The Dissertation Committee for Yiran Su Certifies that this is the approved version of the following dissertation:

Numerical Study of the Steady/Unsteady Multibody Interaction in Ship Propulsion Systems

Committee:

Spyros A. Kinnas, Supervisor

Paola Passalacqua

Howard M. Liljestrand

David G. Bogard

Laxminarayan L. Raja

Numerical Study of the Steady/Unsteady Multibody Interaction in Ship Propulsion Systems

by

Yiran Su

Dissertation

Presented to the Faculty of the Graduate School of

The University of Texas at Austin

in Partial Fulfillment

of the Requirements

for the Degree of

Doctor of Philosophy

The University of Texas at Austin
May 2018

Dedicated to my family.

Acknowledgments

Andritz Hydro GmbH, Wärtsilä Netherlands B.V., Wärtsilä Norway AS, Wärtsilä CME Zhenjiang Propeller Co. Ltd., and Steerprop Ltd.

Numerical Study of the Steady/Unsteady Multibody Interaction in Ship Propulsion Systems

Yiran Su, Ph. D.

The University of Texas at Austin, 2018

Supervisor: Spyros A. Kinnas

The goal of this research is to reduce the computational cost of a fully unsteady RANS simulation for the multibody interaction problems in the ship propulsion system. To achieve this, the boundary element method (BEM) can be coupled with a RANS solver. The rapid-changing propeller-induced flow is first decoupled from the slow-changing or steady total flow. While RANS can be used to calculate the total flow, BEM is applied to the propeller-induced flow. By representing the propeller blades by a body force field and a mass source field, it becomes possible for RANS to use a larger time step size (or even run as a steady problem) and a smaller number of cells. The use of BEM to handle the propeller-induced flow improves the numerical efficiency and also provides a framework for sheet cavitation predictions.

Depending on the level of simplifications, the coupled BEM/RANS scheme can be implemented by three different approaches: the unsteady approach, the time-averaged non-axisymmetric approach, and the time-averaged axisymmetric approach. All of the three approaches are described in this dissertation, as well as some numerical studies on different body force distribution models, mass source models, effective wake calculation models, etc. Then, the scheme is validated by several simple cases in which the propeller's

interaction with upstream bodies is not considered. Finally, the scheme is applied to a hull-propeller-rudder interaction problem and a contra-rotating propeller problem.

Table of Contents

List of Tables

List of Figures

xxiv

Chapter 1.   Introduction

1.1 BACKGROUND

Modern propeller design relies heavily on hydrodynamic analysis tools to predict the propeller performance, propeller cavitation patterns, propeller-induced noises, etc. The numerical methods behind these tools can be roughly divided into two groups, the potential flow methods, and the viscous flow methods.

A potential-based method assumes an irrotational external flow field and represents the lifting body with multiple simple potential flow components. For example, a lifting-line method represents the blade by multiple horseshoe vortex along the span-wise direction and is often used for wind turbines where the span to chord ratio is large and the flow can be simplified to a 2-dimensional flow at each section. For marine propellers, which always have a much smaller span to chord ratio and are sometimes highly skewed, the 3-dimensional effect is stronger and, therefore, the more advanced lifting-surface method should be used instead. In the lifting-surface method, a blade is still represented by horseshoe vortex. The horseshoe vortex is distributed not only along the span-wise direction but also along the chord-wise direction on the mean camber surface of a blade. Finally, the boundary element method (BEM) is another commonly used method in the marine propeller field. The BEM places sources and dipoles on the exact propeller blade surface. It is based on fewer assumptions and considers the blade thickness inherently.

The potential-based methods are widely used for propeller open-water analysis in which the propeller is working inside a uniform and irrotational incoming flow. In the case of a vortical inflow, which is usually caused by the wake of a moving ship hull or other upstream bodies, the propeller-induced potential flow can interact with the inflow and

alters the vortical inflow into the so-called "effective wake". Since the potential theory cannot handle such interactions, the practical way is to use some empirical methods to predict the effective wake field and design the propeller with the predicted effective wake.

The viscous flow methods are mostly based on the Naiver-Stokes equation and are able to handle more general flow fields. In the marine propeller field, the most commonly used methods include the Reynold's Averaged Naiver-Stokes approach (RANS) and the large eddy simulation approach (LES). These methods are often based on a finite volume discretization and solve for the steady flow field in a rotating coordinate system fixed to the propeller shaft.

To accurately evaluate the propeller performance, it is also essential to consider the mutual influence between the ship hull and the propeller, between the propeller and the rudder, between different propellers if multiple propellers are used, and between different rows of the propeller if a multi-row propeller is adopted.

Figure 1.1: Side view of a ship stern (left) and counter-rotating propeller (right) (Source: www.jmuc.co.jp 05/02/2016).

The use of the potential-based methods to handle such multibody interaction problems requires empirical functions to determine the effective wake. Such empirical functions may introduce numerical errors and are hard to get especially for less experienced

2

designs. According to Sánchez-Caja et al. (2015), a 2%-5% error in the effective wake velocity can lead to a 5%-14% numerical error in the predicted propeller forces.

On the other hand, the viscous flow methods are capable of handling such multibody interaction problems. In these applications, the mesh is often divided into multiple zones. The propeller zone is rotating relative to the global zone. It is connected to other zones by sliding interfaces (Sanchez-Caja et al. 2009, Zhuang et al. 2004) or overset mesh (Carrica et al. 2010). Depending on whether an unsteady simulation is needed, the interface can be either a time-accurate interface or a time-averaged interface where all the flow properties are circumferentially averaged on both sides of the interface.

Although the viscous methods excel in the capability of handling various situations, its computational cost can be significant especially for unsteady multibody interaction problems. In a typical hull-propeller interaction problem, the waterline length of the ship hull can be 25-50 times larger than the propeller radius, as shown in Figure 1.2. While the length of the ship hull determines the duration of the simulation (physical time) for flow around the ship hull to get stabilized, the small size and the high angular speed of the propeller controls the upper limit of the time step size. As a result, the cost of multibody interaction problems is usually much higher than a single propeller analysis.

Figure 1.2: The P2772 propeller and the underwater part of the M3458 ship hull

To reduce the computational cost, the propeller blades can be represented either by an actuator disk or by a body force field (Schetz and Favin 1979). These force fields can be calculated by a potential solver. Because the propeller blades are represented by a body

force field, it is possible to use larger cells in the propeller zone and a larger time step size in RANS. Both lead to a better computational efficiency. Due to the same reason, it is also possible to average the flow in time and reduce an unsteady simulation problem to a steady problem. Similarly, the flow can also be averaged in the circumferential direction in order to reduce a 3-dimensional problem to an axisymmetric problem.

1.2 MOTIVATION

In recent years, the requirements have been increased on improving on-board comfort and controlling underwater noise pollutions. As a result, the propeller designers are required to look at the propeller performance in more challenging situations, including ship maneuvering, ship motion under wave and wind conditions, etc. All of these topics are closely related to the multibody interaction problem.

Although the computer hardware and multi-processing technology have been improved significantly, it is still too costly to perform the unsteady multibody interaction analysis with RANS during the design stage. On the other hand, the hybrid potential/RANS approach improves the computational efficiency of the viscous flow solvers. However, most of the current research and applications within this scope treat the problem in a time-averaged way. Therefore, it is useful to develop an efficient time-accurate potential/RANS approach to study the unsteady multibody interaction behaviors.

1.3 OBJECTIVES

The objective of this research is to develop a BEM/RANS scheme which can be utilized by a time-averaged axisymmetric approach, a time-averaged non-axisymmetric approach, and a time-accurate approach. These approaches are based on different levels of

4

simplifications and can provide different levels of flow details. A designer can choose among these approaches based on their design requirements and hardware limitations.

In this study, the BEM is used instead of other potential-based methods because BEM is more general than the lifting surface method and the lifting line method. It does not rely on the small blade thickness assumption and the small angle of attack assumption. It considers the thickness in an inherent way and provides a better framework for pressure calculations and cavitation predictions.

The work in this dissertation includes:

- Extend the capability of PROPCAV, a low order BEM solver for propellers, to handle non-periodical inflows.
- Develop the time-averaged axisymmetric BEM/RANS scheme, time-averaged non-axisymmetric BEM/RANS scheme, and the time-accurate BEM/RANS scheme.
- Study the important factors that may influence the numerical accuracy.
- Validate the BEM/RANS scheme via test cases and justify the assumptions.
- Provide sample applications of the multibody interaction problem and study the numerical error in these applications.

1.4 OVERVIEW

This dissertation contains six major chapters:

Chapter 1 contains the background, motivation, and objectives of this research.

Chapter 2 contains literature reviews of the studies related to the marine propulsor multibody interaction problems.

Chapter 3 introduces the BEM/RANS approach and its implementations in both a time-averaged way and a time-accurate way.

Chapter 4 provides parametric studies, convergence studies, and validation studies of both the time-averaged and the time-accurate BEM/RANS scheme.

Chapter 5 shows several multibody interaction applications of the scheme.

Chapter 6 summarizes the work in this dissertation, lists its major contributions, and provides recommendations for the future research.

1.5 RELATED PUBLICATIONS

The time-averaged BEM/RANS scheme is presented in (Su and Kinnas 2017a). Its applications to propeller P5168, to propeller P2772 (time-averaged hull/propeller/rudder interaction), and to contra-rotating propeller are presented in (Su and Kinnas 2017a), (Su and Kinnas 2017c, Su et al. 2017b), and (Su and Kinnas 2017a) respectively. The time-accurate BEM/RANS scheme and its applications are presented in (Su and Kinnas 2018).

Chapter 2.   Literature Review

The interactions between marine propellers and other bodies are common. Typical situations include propeller-hull interaction, propeller-rudder interaction, and interactions between propellers in a multi-propeller application. This chapter provides literature reviews on the numerical studies that are related to the multibody interaction problems in ship propulsion systems.

The numerical methods for these multibody interaction problems can be divided into three major groups: the potential-based methods, the viscous flow methods, and the hybrid potential/RANS methods.

2.1 POTENTIAL-BASED METHODS

Among all the potential-based propeller hydrodynamics analysis tools, the vortex lattice method and the boundary element method have been mostly used.

The vortex lattice method (VLM) was initially developed for aerodynamic analysis and then introduced to propeller hydrodynamics (Kerwin and Lee 1978). The method is later extended and improved to predict the propeller sheet cavitation (Lee 1979, Kinnas and Fine 1989, Kinnas and Pyo 1999). Generally speaking, the vortex lattice method represents the propeller blade by multiple horseshoe vortex located on the blade mean camber surface and solves for the vortex strength by applying kinematic boundary condition on the wetted surface. Although the method is based on several linear assumptions which require a small thickness to chord ratio, it provides enough accuracy for the industry after applying several corrections (Kinnas 1992, Black 1997).

Comparing to VLM, the boundary element method (BEM), or panel method, is believed to be a more accurate numerical model for marine propellers because it is capable to handle blade thickness, the hub geometry, and the duct geometry in a more direct and realistic way. Since the pioneering work from Hess (Hess and Smith 1967), various forms of the panel method have been applied to propellers (Gibson and Lewis 1973, Hess and Valarezo 1985, Lee 1987, Hoshino 1989, Vaz 2005, Gaggero and Brizzolara 2008). Under the framework of the panel method, various models have been studied and implemented, including the sheet cavitation (Fine 1992, Vaz 2005), tip cavitation (Lee 2002), viscous boundary layer correction (Hufford 1992, Sun 2008), propeller-induced pressure calculation (Su and Kinnas 2017), etc.

PROPCAV is a low-order panel code which was initially developed to solve the steady wetted performance of marine propellers (Lee 1987). It was then improved to handle the unsteady periodical propeller performance under non-uniform inflow (Hsin 1990) and to predict propeller face cavitation (Fine 1992). After that, an unsteady tip vortex model was added to the solver which enables the calculation of tip cavitation (Lee 2002). Sun (2008) coupled PROPCAV with a boundary layer integral equation solver (Drela 1989) to consider the boundary layer effect on the blade surface.

Due to the limitations of the potential flow theory, the above methods are mostly designed to work under irrotational inflow conditions. However, in real applications, either it is a hull-propeller-rudder interaction or a propeller-to-propeller interaction, the incoming flows to the aft bodies are usually viscous due to the boundary layer of the upstream bodies. In such situations, the background flow field in which the propeller is operating is no longer the incoming flow (nominal wake) because the propeller-induced velocity can interact with the viscous inflow. The real background flow (called effective wake) can be calculated empirically or numerically (Carlton 2012).

8

The potential methods can also be used to handle the multibody interaction problems. Liu (2009) used BEM to predict the interaction between the forward propeller and the aft propeller in a contra-rotating propeller (CRP) application. In this application, both propellers are handled by a separate BEM model and the interaction between the two propellers is included by adding the perturbation flow field in every BEM model into the background flow of the other BEM model. Similar methods are also applied to other CRP geometries (Ghassemi and Taherinasab 2013) and water-jet propulsors (Kinnas et al. 2007a, Chang 2010). In these applications, the induced flow velocity from one propeller is time-averaged before it is included in the background flow of the other propeller. This time-averaging process is important because it desingularized the perturbation flow field at the trailing wake surfaces. However, this also causes numerical errors because it turns the discrete the vortex sheet into a volumetric vorticity field and makes the inflow to the downstream propellers to be vortical.

Different from the time-averaged approach, He (2010) studied the propeller-rudder interaction problem in a fully unsteady way. The propeller is solved by the VLM and the rudder is handled by the BEM. The time-accurate interaction between the propeller trailing wake and the rudder can be simulated in this application. To desingularize the flow when the rudder is very close to the wake surface, a numerical fence is applied around the rudder and a simplified vortex core diffusion model is applied to the propeller trailing wake.

2.2 VISCOUS FLOW METHODS

The viscous flow solvers are also widely used in predicting marine propeller performances. Compared to the potential solvers, the viscous flow solvers are able to handle more complex physics in a more general way. Due to the complexity of the propeller

geometry, most of the Navier-Stokes-based applications use the Reynolds averaged (RANS) approach (Sanchez-Caja et al. 2000, Li 2006), the detached-eddy (DES) approach (Mascio et al. 2014, Chase et al. 2013), or the large eddy simulation (LES) approach (Bensow and Bard 2010, Balaras et al. 2015). Brizzolara et al. (2008) performed a systematic comparison between the RANS method and the panel method for propeller applications. Since full-scale marine propellers usually have high Reynolds numbers, a complete turbulence simulation is usually considered enough for such applications. The laminar to turbulent transition is more likely to be a problem of model-scale propellers (Baltazar et al. 2017).

To simulate the multibody interactions with the above methods, the fluid domain is usually divided into one global zone which is fixed to the ship hull and one (or multiple) propeller zone(s) which rotates with the propeller. The zones can be connected by a sliding interface (Sanchez-Caja et al. 2009, Zhuang et al. 2004), or the overset mesh technique (Carrica et al. 2010). If the unsteady propeller performance is not needed, the flow properties can be averaged along the θ (circumferential) direction on the interface. This reduces the multibody interaction problem from unsteady to steady and, therefore, reduces the computational cost. It also enables the use of periodical condition for the propeller zone, where only the key blade needs to be modeled and the other blades are just periodical repeats of the key blade.

2.3 POTENTIAL/RANS METHODS

Both the potential-based methods and the viscous flow methods have some limitations in the multibody interaction simulations. First, the potential-based methods require an empirical or semi-empirical way to determine the effective wake. This may

10

introduce numerical errors especially for less experience propeller designs and off-design loading conditions. The viscous flow solvers can handle such interaction behaviors, but usually takes much longer mesh preparation times and computing times.

To reduce the matrix size of the RANS solver, the propeller can be represented by either an actuator disk or a body force field. The actuator disk model eliminates the cyclic, unsteady, and three-dimensional components. As a result, it can cause near field numerical errors. Therefore, the body force model is believed to be better (Schetz and Favin 1979).

Following the body force approach, Stern et al. (1986) coupled VLM with RANS to predict the unsteady effective wake. The vortex lattice solver is used to calculate the propeller performance and to determine the body force field while the RANS solver is used to predict the interaction between the vortical inflow and the propeller-induced flow. The main purpose of the VLM/RANS approach is to reduce the computational cost of the viscous flow solvers while still maintain the capability of handling viscous flow interactions.

Kerwin et al. (1994) developed an iterative scheme in which the axisymmetric flow component is handled by RANS while the non-axisymmetric part is obtained from VLM. The propeller is represented by axial, radial, and circumferential body force field. Based on this scheme, Black (1997) studied the influence of the thickness blockage effect and viscous boundary layer effect.

Similar to Stern's approach (Stern et al. 1986), Choi (2001) coupled VLM with a Euler solver. In this application, the representation of body force is studied and improved. The scheme can be adapted to solve unsteady problems, steady non-axisymmetric problems, and steady axisymmetric problems. The lack of thickness blockage effect is claimed to be the cause of the numerical error in the dissertation. Later, Mishra (2005)

11

replaced the Euler solver with a RANS solver. The scheme is then applied to a ducted propeller and a contra-rotating propeller (Kinnas et al. 2002, Tian et al. 2014).

Due to the limited computing power in early years, most of these applications determines the effective wake field by solving the interactions between the vortical nominal-wake and the propeller. The nominal wake is determined prior to the simulation. In recent years, with the improvements in computer hardware and parallel computing, the use of BEM and large-scale RANS solver becomes much easier. As a result, it is possible to include the upstream bodies directly in the BEM/RANS solver.

Greve et al. (2012) developed a time-averaged BEM/RANS approach and applied it to a propeller-hull interaction problem (Berger et al. 2013). Starke and Bosschers (2012) developed a similar approach for the propeller-hull interaction problem and studied the scale effect in the ship powering performance. Both applications neglected the thickness blockage effect in the RANS solver. However, in order to be consistent, the second application also neglected the source-induced velocity field term (Rijpkema et al. 2013). Later Hally (2015, 2017) applied the time-averaged BEM/RANS scheme to a submarine-propeller interaction problem. In this application, the thickness blockage effect in included in RANS, but the associated Lagally force (Su 2017a) is not compensated. To improve the numerical results, a correction term is computed from the uniform inflow case and added to the hull-propeller interaction cases.

There are also several applications of the time-accurate BEM/RANS scheme. In these applications, the body force field is confined to one or several layers of cells and moves with the propeller blades. This scheme provides the propeller performance inside an unsteady nominal wake which can be useful for unsteady force calculations, propeller-induced noise calculations, and unsteady cavitation predictions. Nathan et al. (2012) coupled a delayed detached-eddy simulation (DDES) solver with an unsteady vortex lattice

solver and applied the scheme to a self-propulsion simulation of the DARPA sub-off. The results show good agreements under open-water conditions and straight-ahead conditions but begin to diverge at large wake distortions and low advance ratios.

Salvatore et al. (2015) and Calcagni et al. (2017) developed a fully-unsteady BEM/DES scheme for the propeller-rudder interaction problem. In this application, the mesh density in the propeller zone is much higher than the rest of the domain. The body force is firstly combined to the mean camber surface and then applied to several layers of volume cells by a Gaussian distribution function along the normal direction. The thickness blockage effect is not considered in this work.

Gaggero et al. (2017) developed a fully unsteady BEM/RANS approach for the self-propulsion simulation of a surface ship. This scheme also uses higher mesh density in the propeller region, so that there can be 3 to 4 layers of cells inside the propeller blade thickness. The body force is applied directly to the blade surface and distributed to nearby cells by a smooth distribution function.

2.4 ORIGINALITY OF THE CURRENT WORK

The work in this dissertation is based on a time-averaged VLM/Euler scheme (Choi 2001, Choi and Kinnas 2001), a time-averaged VLM/RANS scheme (Mishra 2005, Tian et al. 2014) and a periodical version of the boundary element code PROPCAV v3.3 (Su et al. 2016). The work includes:

- Improve the VLM/RANS interface to support the time-averaged BEM/RANS coupling; Study the influence of different body force distribution models, thickness models, and effective wake calculation models

- Improve the PROPCAV code to handle non-periodical inflow conditions

- Develop the unsteady BEM/RANS scheme; Perform parametric studies and validation tests on the unsteady BEM/RANS scheme. Unlike most of the existing time-accurate BEM/RANS implementations, this scheme does not rely on a highly-refined body force zone mesh and does not rely on the upstream disk to evaluated the effective wake. As a result, the BEM/RANS scheme can be more efficient and more accurate in calculating the effective wake field.

- Apply the unsteady BEM/RANS scheme to ship maneuvering cases

Compared to other unsteady BEM/RANS (or BEM/DES) implementations, the major difference in this dissertation is the use of only one single layer (per blade) of RANS panels to applied the body force. The benefit is a higher computational efficiency due to the reduced number of cells and the increased time step size limit. Other differences are described in the coming chapters.

Chapter 3.   Methodology

This chapter describes the boundary element method, the BEM/RANS coupling scheme, and the implementation of the BEM/RANS scheme. Different ways of body force calculation, mass source calculation, and effective wake evaluation are also described in this chapter and compared in the following chapter. Since the time-averaged problem can be seen as a simplified version of the time-accurate problem, the time-accurate version of the scheme is always described first, followed by the time-average version and the axisymmetric version. To distinguish between these three different approaches, the following terms can be defined:

- Unsteady problem/scheme/approach

    This is the most general situation. There are no restrictions on the periodicity of the propeller performance. The effective wake (observed from the ship-fixed coordinate system) may change with time.

- Non-axisymmetric problem/scheme/approach

    This is the time-averaged version of the unsteady problem. The effective wake cannot change with time (observed from the ship-fixed coordinate system) but can vary in space. The propeller performance is a function of the blade angle and has to be periodical in time. In this case, the time-averaged assumption has two underlying meanings: (a) The incoming flow and the ship motion does not change with time; (b) Like a quasi-steady state, the rotation of the propeller does not introduce any time-dependency (approximately) to the ship/global system.

- Axisymmetric problem/scheme/approach:

This is the circumferentially-averaged version of the non-axisymmetric problem. The effective wake cannot change in time or in the circumferential direction. The propeller performance is a constant and does not change with the blade angle. This problem requires the incoming flow and the upstream bodies to be axisymmetric.

3.1 BOUNDARY ELEMENT METHOD

3.1.1 Flow decomposition

According to the Helmholtz's theorem, a twice differentiable vector field can be decomposed into a curl-free component and a divergence-free component.

$$\vec{F} = \nabla \times \vec{A} + \vec{\nabla}\Phi \tag{3.1}$$

There is an infinite number of decompositions that satisfy the theorem because the curl-free component can always be decomposed into two curl-free components and either one can be added to the divergence-free component without violating the theorem. In this propeller application, we choose the propeller-induced potential flow as the curl-free component, as shown in Equation (3.2).

$$q_t\left(\vec{x},t\right) = q_e\left(\vec{x},t\right) + q\left(\vec{x},t\right) \tag{3.2}$$

In Equation (3.2), the total flow q_t is decomposed to the effective wake flow q_e and the propeller-induced flow q.

The above equation can also be defined in a rotating coordinate system fixed to the propeller shaft, as shown in Equation (3.3).

16

$$q_t\left(\vec{x},t\right)=q_e\left(\vec{x},t\right)+\vec{\Omega}\times\vec{x}+q\left(\vec{x},t\right)$$ (3.3)

Since the propeller-induced flow is a potential flow, it can be written as the gradient of the perturbation potential ϕ which is governed by the Laplace equation.

$$q\left(\vec{x},t\right)=\vec{\nabla}\phi\left(\vec{x},t\right)$$ (3.4)

$$\nabla^2\phi\left(\vec{x},t\right)=0$$ (3.5)

3.1.2 Boundary condition

Although PROPCAV code is capable of solving a cavitating propeller, the propeller cavitation is not the focus of this research. Therefore, only the boundary conditions and equations under the wetted situation are given in this chapter. The detailed description of the cavitation solver is given in (Fine 1992) and (Young 2002).

As shown in Figure 3.1, a kinematic boundary condition is applied to the propeller blade and hub surfaces S_B. After applying Equation (3.3) - (3.5), the boundary condition to the perturbation potential field can be derived:

$$\frac{\partial\phi}{\partial n}=-\left(\vec{q_e}+\vec{\Omega}\times\vec{x}\right)\cdot\vec{n}$$ (3.6)

At the far field, the perturbation potential should vanish:

$$\phi\left(\vec{x},t\right)=0$$ (3.7)

Since the propeller blade is a lifting body, there should be a vortex sheet following the trailing edge of the blade. On the two sides of the vortex sheet, the perturbation potential is different. A force-free condition should be applied on the wake surface and, therefore, on the blade trailing edge as well. In Figure 3.1, the trailing wake surface is only plotted on one blade.

$$\Delta p\left(\vec{x},t\right)\Big|_{\vec{x}\,\in\,S_W(t)} = 0 \tag{3.8}$$
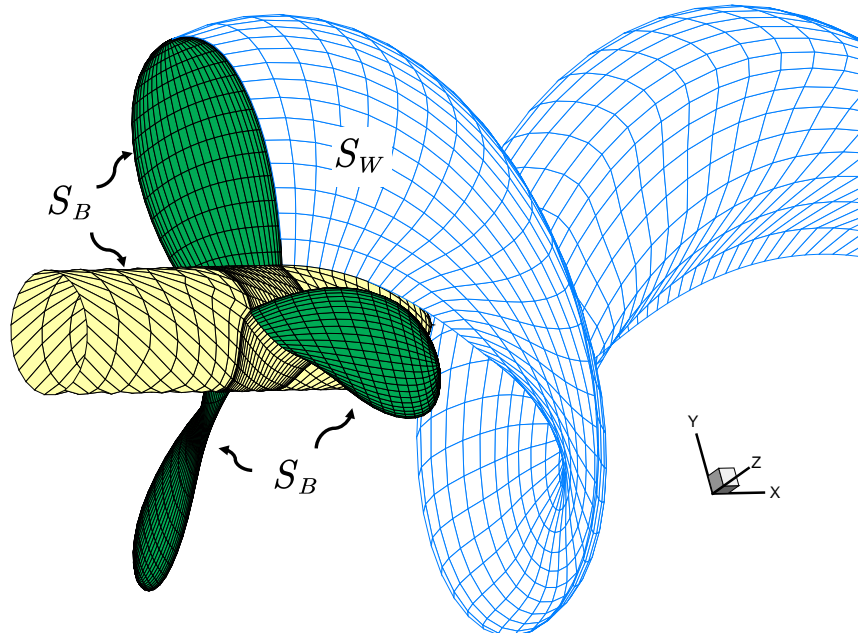
Figure 3.1: An example BEM panel model for a 3-blade open propeller under non-cavitating conditions. The hub surface, blade surfaces, and one (out of 3) trailing wake surface is shown.

3.1.3 Boundary element method

The boundary element method is used to solve the boundary value problem described above. Equation (3.5) is first inserted into the Green's second identity, as shown

18

in Equation (3.9). In this equation, $G(p;q)$ is the Green's function for the Laplace operator, as shown in Equation (3.10), ϕ_p is the perturbation potential at any point (p) of the domain, ϕ_q is the perturbation potential at the integration point (q), $\Delta\phi_q$ is the potential difference between both sides of the wake surface. The integration is performed at the propeller blade and hub surfaces S_B and at the trailing wake surfaces S_W. The normal vector on the integrated surface is noted as n_q.

$$I_p\phi_p = \iint_{q \in S_B} \left(\phi_q \frac{\partial G(p;q)}{\partial n_q} - G(p;q)\frac{\partial \phi_q}{\partial n_q} \right) dS + \iint_{q \in S_W} \Delta\phi_q \frac{\partial G(p;q)}{\partial n_q} dS \qquad (3.9)$$

$$G(p;q) = \frac{1}{4\pi}\frac{1}{r(p;q)} \qquad (3.10)$$

Depending on whether point p is located inside the fluid domain, outside the fluid domain, or on the propeller surface, the I_p factor should be given a different value, as shown in Equation (3.11).

$$I_p = \begin{cases} 1.0; & \forall p \text{ inside fluid domain} \\ 0.5; & \forall p \text{ on } S_B \\ 0.0; & \forall p \text{ outside fluid domain} \end{cases} \qquad (3.11)$$

If we take the gradient of Equation (3.9), the propeller-induced velocity inside the fluid domain can be calculated by:

$$\vec{q}_p = \iint_{q \in S_B} \left(\phi_q \frac{\partial \vec{G}_\nabla(p;q)}{\partial n_q} - \vec{G}_\nabla(p;q)\frac{\partial \phi_q}{\partial n_q} \right) dS + \iint_{q \in S_W} \Delta\phi_q \frac{\partial \vec{G}_\nabla(p;q)}{\partial n_q} dS \quad (3.12)$$

where $\vec{G}_\nabla(p;q) = \nabla_p[G(p;q)]$.

19

3.1.4 Effective wake

In Equation (3.3), the flow is decomposed to the effective wake and the propeller-induced flow. Then the boundary condition of the perturbation potential is given in Equation (3.6) assuming the effective wake is known. In reality, we might not know the effective wake field before solving BEM.

Typically, the flow information we can get before a propeller analysis is the nominal wake. A nominal wake is defined by the flow observed in the absence of the propeller. It can be obtained by empirical equations (Carlton 2012), by model tests, or by CFD simulations of the flow around the ship hull.

To calculate the effective wake from the nominal wake, there are two different situations:

- If the nominal wake is irrotational, it is also governed by the Laplace equation. Therefore, we can simply add the propeller-induced flow to the nominal wake to form the total flow. In other words, the effective wake is equal to the nominal wake.

- If the nominal wake is vortical, it is governed by the nonlinear Navier-Stokes equation and can no longer be linearly added to the propeller-induced flow. Therefore, including the propeller's effect on the flow also modifies the nominal wake. We call this modified nominal wake to be the effective wake. According to (Carlton 2012), the effective wake can be expressed in two ways:

    - effective velocity = nominal velocity + interaction velocity
    - effective velocity = total velocity – propeller-induced velocity

3.1.5 Calculation of pressure and forces

To calculate the pressure distribution on the propeller surface, the head-loss/gain caused by the viscous/turbulence diffusion is neglected and the Euler equation in the

rotating coordinate system is used to derive the Bernoulli equation (3.13), where ω is the rotation vector of the coordinate system and x is the coordinate vector. Then, the time derivative term can be decomposed and some vector identities can be applied (Kinnas 2006), resulting in the Equation (3.14). The total head H is defined by Equation (3.15).

$$\frac{\partial \vec{q_t}}{\partial t} - \vec{q_t} \times \left(\vec{\nabla} \times \vec{q_t} + 2\vec{\omega} \right) = -\vec{\nabla} \left[\frac{p}{\rho} + \frac{q_t^2}{2} - \vec{g} \cdot \vec{x} - \frac{\left(\vec{\omega} \times \vec{x} \right)^2}{2} \right] \qquad (3.13)$$

$$\vec{\nabla} H = -\frac{\partial \vec{q_e}}{\partial t} + \vec{q_t} \times \left(\vec{\nabla} \times \vec{q_e} \right) \qquad (3.14)$$

$$H = \frac{\partial \phi}{\partial t} + \frac{p}{\rho} + \frac{q_t^2}{2} - \vec{g} \cdot \vec{x} - \frac{\left(\vec{\omega} \times \vec{x} \right)^2}{2} \qquad (3.15)$$

If we integrate Equation (3.14) along the streamline s from point p_0 to point p_1, the second term on the right-hand side vanishes and we get:

$$H(p_1) - H(p_0) = -\int_{p_0 \in s}^{p_1 \in s} \frac{\partial \vec{q_e}}{\partial t} \cdot \vec{\gamma} ds \qquad (3.16)$$

This is the general equation for calculating the pressure inside the BEM solver. However, under certain situations, the equation can be simplified. If the effective wake q_e is steady and irrotational, the right-hand side of Equation (3.14) becomes zero and, therefore, the total head H is uniform across the flow field. If we apply the integration of Equation (3.14) along any curves from far upstream to the target point, we can get Equation (3.17). p_s is the far upstream shaft pressure, $q_{t\infty}$ is the far upstream relative velocity magnitude at the same radius as x.

21

$$\frac{p_s}{\rho} + \frac{q_{t\infty}^2}{2} = \frac{\partial \phi}{\partial t} + \frac{p}{\rho} + \frac{q_t^2}{2} - \vec{g} \cdot \vec{x}$$

(3.17)

In the current PROPCAV code, Equation (3.17) is always used to calculate the pressure on the propeller surface even if the effective wake is unsteady or vortical. In practice, this does not seem to create much numerical error as long as the change of the effective wake along the streamwise direction is not large.

After the calculation of the pressure, the total force acting on the blade can be calculated by the following equation. In Equation (3.18) - (3.19), n is the normal vector on the propeller surface, γ is the unit vector in the total velocity's direction. The skin friction f can be calculated either empirically or by solving the boundary layer integral equation (Sun 2008).

$$\vec{T} = \iint_{S_B} \left[\left(\vec{n} \cdot \vec{i}_x \right) p + \left(\vec{\gamma} \cdot \vec{i}_x \right) f \right] dS$$

(3.18)

$$\vec{Q} = \iint_{S_B} \left[\left(\vec{n} \cdot \vec{i}_\theta \right) p + \left(\vec{\gamma} \cdot \vec{i}_\theta \right) f \right] r dS$$

(3.19)

3.1.6 Single-blade problem

To solve Equation (3.9), the surface of the propeller S_B and the trailing wake surface S_W can be discretized to BEM panels, as shown in Figure 3.1. Given a single-blade propeller, Equation (3.9) can be discretized to the following equation:

$$A_{ij}\phi_j + B_{ij}\frac{\partial \phi_j}{\partial n_j} + W_{ik}\Delta\phi_k = 0$$

(3.20)

In Equation (3.20), i and j are blade/hub panel indexes; k is the wake panel index. A_{ij}, B_{ij}, and W_{ij} are dipole influence coefficient from a blade/hub panel, source influence coefficient from a blade/hub panel, and dipole influence coefficient from a wake panel respectively. They can be calculated by Equation (3.21) - (3.23). Here, P_i is the control point (usually the centroid) of the i-th panel; q is a point on the panel surface S_j or S_k; n is the normal vector on point q.

$$A_{ij} = \iint_{q \in S_j} \frac{\partial G(P_i; q)}{\partial n_j} dS \tag{3.21}$$

$$B_{ij} = \iint_{q \in S_j} G(P_i; q) dS \tag{3.22}$$

$$W_{ik} = \iint_{q \in S_k} \frac{\partial G(P_i; q)}{\partial n_k} dS \tag{3.23}$$

To solve Equation (3.20), $B_{ij} \dfrac{\partial \phi_j}{\partial n_j}$ term is known and moved to the right-hand side while $A_{ij}\phi_j$ term is to be solved and put to the left-hand side. $\Delta\phi_k$ is generally known except for the first row of panels. Therefore, the $W_{ij}\Delta\phi_k$ term is partially in the left-hand side and mainly in the right-hand side. In the case of an axisymmetric problem, $\Delta\phi_k$ does not change along the streamwise direction and, therefore, the $W_{ik}\Delta\phi_k$ term is put purely in the left-hand side.

3.1.7 Trailing wake

In order to solve Equation (3.20), we also need two types of information about the trailing wake: the wake surface geometry and the dipole strength $\Delta\phi$ on the first row of wake panels.

According to the Helmholtz theorem, for any ideal and barotropic fluid subject only to conservative forces, the vortex line moves with the flow and does not change in strength (circulation). Therefore, the move of the wake surface can be described by:

$$\frac{\partial \vec{x}_w}{\partial t} = \vec{q}_t\left(\vec{x}_w, t\right) \tag{3.24}$$

In other words, the dipole panels on the wake surface move and deform with the flow. However, the dipole strength on the panel remains unchanged. This explains why the dipole strength is known on the wake surface except for the first row of panels.

In the case of an axisymmetric problem or a problem in which the unsteady wake behavior is ignored, the flow is steady in the rotating coordinate system. Therefore, the path-line defined by Equation (3.24) coincides with the streamline and the wake surface no longer change with time.

To calculate the dipole strength $\Delta\phi$ on the first row of wake panel, the zero pressure jump condition should be applied at the trailing edge. For a 2D foil, the zero pressure jump condition leads to the Morino condition:

$$\Delta\phi_k = \phi_W^+ - \phi_W^- = \phi_k^+ - \phi_k^-$$

Here, the ϕ_k^+ and ϕ_k^- represent the perturbation potential at the suction side of the trailing edge and at the pressure side of the trailing edge respectively; k is the panel index number in the span-wise direction. Special treatment is needed if the perturbation potential is not stored at the trailing edge (Lee 1987).

For a 3-dimensional propeller flow, the different velocity direction on two sides of the trailing edge and the different total head caused by the inflow vorticity makes the Morino condition no longer valid. As a result, an iterative pressure Kutta condition, defined

by Equation (3.25), should be used (Lee 1987, Kinnas and Hsin 1992). In the iterative scheme, the Morino condition is first used as the initial guess. Then, the wake dipole strength is adjusted in an iterative way. Here, k and n are panel indexes in the span-wise direction; i is the iteration number. Matrix R_{nk} is determined by the Newton-Raphson method.

$$\Delta \phi_k^{(i)} = \phi_k^{+(i)} - \phi_k^{-(i)} + R_{nk} \Delta p_n^{(i-1)} \tag{3.25}$$

3.1.8 Multi-blade problem

- Unsteady problem

For the multi-blade unsteady problem, in order to reduce the matrix size, only one blade (called the key blade) is solved at the time, as shown in Equation (3.26). Z is the number of blades; $\mathbb{A}$, $\mathbb{B}$, and $\mathbb{W}$ are the influence coefficients matrix from the source, the dipole, and the wake; subscript $(\ )_{j,1}$ means the influence coefficients matrix is from j-th blade to the key blade; $\Phi_j(t)$ is the perturbation potential (BEM solution) on the j-th blade at time t; superscript $(\ )^{(1)}$ and $(\ )^{(2+)}$ represent the first row of wake panels and the other rows of wake panels respectively.

$$
\begin{aligned}
\mathbb{A}_{1,1}\Phi_1(t) \ &+ \mathbb{W}_{1,1}^{(1)}\Delta\Phi_1^{(1)}(t) \\
= \ &- \sum_{j=2}^{Z} \mathbb{A}_{j,1}\Phi_j(t) \\
&- \sum_{j=1}^{Z} \mathbb{B}_{j,1}\frac{\partial\Phi_j(t)}{\partial n} \\
&- \mathbb{W}_{1,1}^{(2+)}\Delta\Phi_1^{(2+)}(t) \\
&- \sum_{k=2}^{Z} \mathbb{W}_{k,1}\Delta\Phi_k(t)
\end{aligned}
\tag{3.26}
$$

25

The interactions between blades are considered in an iterative manner, as shown in Figure 3.2. Within every time step, each blade is solved in a sequential manner and the process is repeated until fully converged. Every blade can have a unique solution and the solution is a function of time.
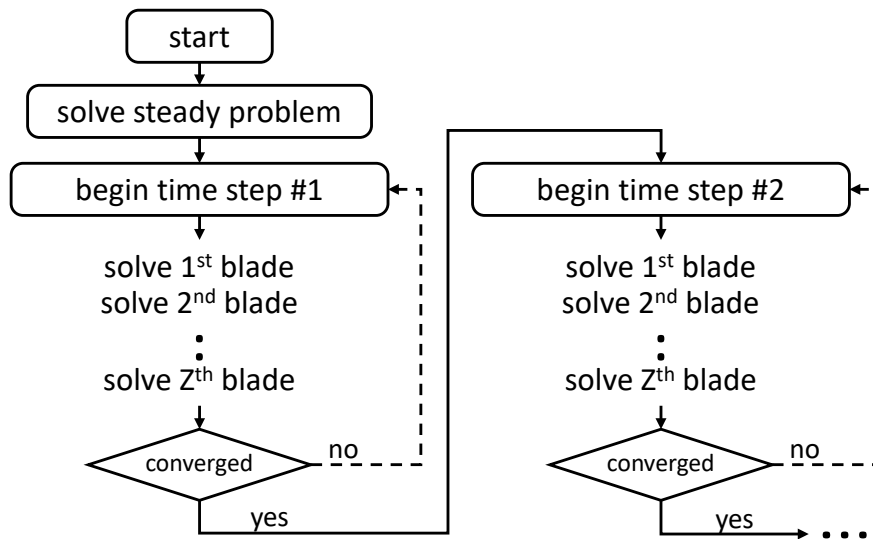
Figure 3.2: Flow chart of the unsteady boundary element method.

- Non-axisymmetric problem

For the multi-blade non-axisymmetric problem, the above equation can be modified to reduce the computational cost. In the non-axisymmetric problem, the solution is periodical and is only a function of the blade angle. Therefore, we only need to solve the problem at different blade angles. All the blades should have the same solution except for a phase difference. The equation for the non-axisymmetric problem is given below:

$$\mathbb{A}_{1,1}\Phi_1\left(\theta_l^1\right) + \mathbb{W}_{1,1}^{(1)}\Delta\Phi_1^{(1)}\left(\theta_l^1\right)$$

$$= \quad - \sum_{j=2}^{Z} \mathbb{A}_{j,1}\Phi_j\left(\theta_l^j\right)$$

$$- \sum_{j=1}^{Z} \mathbb{B}_{j,1}\frac{\partial\Phi_j\left(\theta_l^j\right)}{\partial n} \tag{3.27}$$

$$- \mathbb{W}_{1,1}^{(2+)}\Delta\Phi_1^{(2+)}\left(\theta_l^1\right)$$

$$- \sum_{k=2}^{Z} \mathbb{W}_{k,1}\Delta\Phi_k\left(\theta_l^j\right)$$

Here, θ_l^j is the blade angle of the j-th blade when the key blade is located at θ_l^1, as shown in Equation (3.28).

$$\theta_l^j = \theta_l^1 + (j-1) \times \frac{2\pi}{Z} \tag{3.28}$$

Equation (3.27) is solved sequentially at different blade angles, $\theta_1 \ldots \theta_n$, as shown in Figure 3.3. It usually takes 3 – 6 revolutions for the solution to converge.
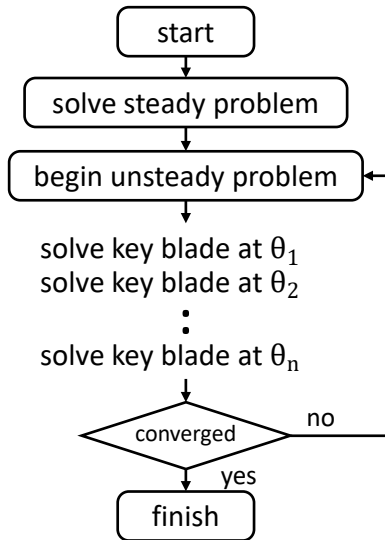
Figure 3.3: Flow chart of the steady boundary element method.

27

- Axisymmetric problem

In the axisymmetric problem, the solution is the same for every blade and at every blade angle. Therefore, we only need to solve Equation (3.29) once to get the solution.

$$\sum_{j=1}^{Z} \mathbb{A}_{j,1}\Phi_1 + \sum_{k=1}^{Z} \mathbb{W}_{k,1}\Delta\Phi_1 = -\sum_{j=1}^{Z} \mathbb{B}_{j,1}\frac{\partial\Phi_1}{\partial \mathrm{n}} \qquad (3.29)$$

3.1.9 Boundary layer correction

Although BEM is only a potential solver and is not able to calculate the flow inside the boundary layer, corrections can be made to consider the boundary layer's effect to the outside flow (Drela 1989, Sun 2008, Kinnas et al. 2012). The scheme simplifies the boundary layer into blowing sources and places those sources onto the blade surface panels. The source strength $\hat{\sigma}$ can be calculated by Equation (3.30) where U_e is the edge velocity, δ^* is the displacement thickness, and s is the panel direction. The edge velocity and displacement thickness can be solved by coupling PROPCAV with a boundary layer solver XFOIL.

$$\hat{\sigma} = \frac{d\left(U_e\delta^*\right)}{ds} \qquad (3.30)$$

3.2 BEM/RANS COUPLING

An unsteady RANS simulation of the multibody interaction problem can be costly. Take the hull-propeller interaction as an example. Usually, the dimension of the ship hull is much larger compared to the dimension of the propeller, as shown in Figure 3.4. If we solve both the hull and the propeller in the same RANS model, it may take a long simulation

time for the flow around the ship hull to stabilize while it also requires a small time-step-size due to the small dimensions and the fast rotation of the propeller. As a result, the computational cost can be very high.

In fact, there is no need to solve both the ship hull and the propeller in the same model. The flow around the ship hull can be seen as in a quasi-steady state. In other words, since the dimensions of the propeller are so small and the propeller is moving much faster than the ship hull, the propeller-induced unsteady flow can be decoupled from the ship hull flow system. Given that the flow can be decomposed to a steady (or slow-changing) ship hull flow and a rapid-changing propeller flow, we can then use a much larger time-step-size for the ship hull flow and saves time.
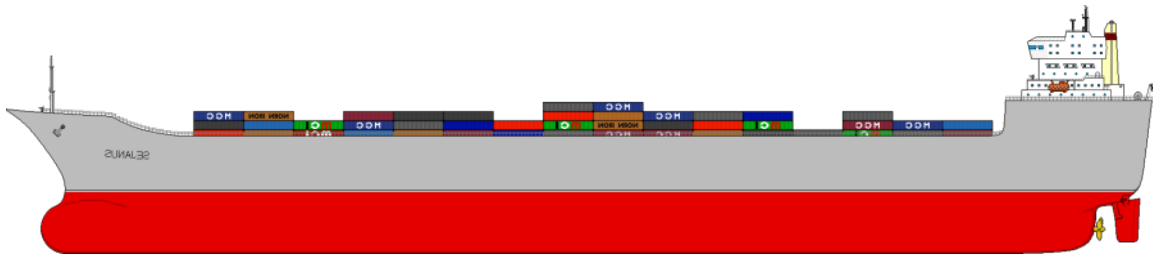
Figure 3.4: Side view of a container ship. The ship stern and the propeller are at the right side of the plot.

The BEM/RANS coupling scheme is based on such kind of flow decomposition. The steady or slow-changing ship hull flow is solved by a steady RANS or an unsteady RANS with a larger time-step-size[1]. The rapid-changing propeller-induced flow can be solved by BEM. In order to include the propeller's effect in RANS, the propeller blades can be represented by body force fields and mass source fields.

---

[1] The RANS solver in this dissertation refers to ANSYS Fluent v18.2
(https://www.ansys.com/products/fluids/ansys-fluent).

3.2.1 Assumptions

In the BEM/RANS scheme, due to the large time-step-size, the propeller blades cannot be represented by non-slip wall boundaries. In order to consider the influence of the propeller to the ship hull flow, a propeller blade can be represented by the following terms:

- Normal pressure and skin friction

This term includes all the forces a propeller blade imposes to the surrounding flow. It can be represented by a body force term in the momentum equation. The normal pressure on the propeller blade can be evaluated by the Bernoulli Equation, as shown in Equation (3.16). The skin friction can be calculated by the boundary layer solver or simply by an empirical skin friction coefficient.

- Thickness blockage effect

The thickness blockage effect means the displacement of mass due to the blade thickness. Therefore, this term can be represented by a mass source field which can be applied to the continuity equation.

- Boundary layer blockage effect

The boundary layers on both sides of the blade have a similar effect to the blade thickness effect. Due to the velocity deficit near the wall, the external flow is "pushed" outward by the displacement thickness. Thus, the boundary layer term can also be represented by the mass source term and applied to the continuity equation.

- Compensating force

If a non-zero source term is added to the continuity equation, another term is automatically included in the non-conservative form of the momentum equation. This term reduces the local velocity when mass is added and increases the local velocity when mass is subtracted. This term needs to be compensated by an extra body force term.

Based on the assumptions above, the unsteady RANS equation can be written as:

$$\frac{\partial \overline{U}_j}{\partial x_j} = \mathcal{Q}(x,r,\theta,t) \tag{3.31}$$

$$\frac{\partial \overline{U}_i}{\partial t} + \overline{U}_j \frac{\partial \overline{U}_i}{\partial x_j} = -\frac{1}{\rho} \frac{\partial \overline{P}}{\partial x_i} + \nu \frac{\partial^2 \overline{U}_i}{\partial x_j \partial x_j} - \frac{\partial}{\partial x_j} \langle u_i u_j \rangle + \mathcal{F}_i(x,r,\theta,t) \tag{3.32}$$

In Equation (3.31) and (3.32), $\overline{U}$ is the unsteady Reynolds averaged velocity and $\overline{P}$ is the unsteady Reynolds averaged pressure. Depending on the reference frames used in each zone, certain inertial force terms should be added to the momentum equation.

Instead of using non-slip wall boundaries, the propeller blades can be represented by the mass source term $\mathcal{Q}$ and the body force term $\mathcal{F}$. These terms are non-zero only inside the propeller zone. The use of these terms enables the representation of a time-averaged propeller effect. In the unsteady problem, more specifically, both the mass source term and the body force term are time-averaged within the RANS time-step-size.

The unsteady problem can be simplified to the steady non-axisymmetric problem at certain conditions or certain assumptions. If the ship flow does not change with time, the propeller performance should be periodic and can be expressed as a function of the blade angle. If we integrate Equation (3.31) and (3.32) over the propeller revolution period, we get:

$$\frac{\partial \overline{U}_j}{\partial x_j} = \mathcal{Q}(x,r,\theta) \tag{3.33}$$

$$\overline{U}_j \frac{\partial \overline{U}_i}{\partial x_j} = -\frac{1}{\rho} \frac{\partial \overline{P}}{\partial x_i} + \nu \frac{\partial^2 \overline{U}_i}{\partial x_j \partial x_j} - \frac{\partial}{\partial x_j} \langle u_i u_j \rangle + \mathcal{F}_i(x,r,\theta) \tag{3.34}$$

31

In Equation (3.33) and (3.34), $\overline{U}$ is the steady Reynolds averaged velocity and $\overline{P}$ is the steady Reynolds averaged pressure. The unsteady components are dropped due to the periodical flow condition. The cross terms originated from the convection term are also neglected because of the assumption that the propeller-induced unsteady velocity is much smaller than the time-averaged velocity components. This scheme can be seen as the unsteady scheme with the time-step-size set to the propeller revolution period.

The steady non-axisymmetric problem can be further simplified to the steady axisymmetric problem. If the inflow and the geometry of the upstream body are both axisymmetric, the propeller performance should be a constant and does not change with the blade angle. If we integrate Equation (3.33) and (3.34) in the θ-direction, we get the axisymmetric RANS equation:

$$\frac{\partial \overline{U_j}}{\partial x_j} = \mathcal{Q}(x,r) \tag{3.35}$$

$$\overline{U_j}\frac{\partial \overline{U_i}}{\partial x_j} = -\frac{1}{\rho}\frac{\partial \overline{P}}{\partial x_i} + \nu \frac{\partial^2 \overline{U_i}}{\partial x_j \partial x_j} - \frac{\partial}{\partial x_j}\langle u_i u_j \rangle + \mathcal{F}_i(x,r) \tag{3.36}$$

In Equation (3.35) and (3.36), $\overline{U}$ is the axisymmetric Reynolds averaged velocity and $\overline{P}$ is the axisymmetric Reynolds averaged pressure. The non-axisymmetric components are dropped. The cross terms originated from the convection term are also neglected because of the assumption that the propeller-induced non-axisymmetric velocity is much smaller than the axisymmetric velocity components.

32

3.2.2 Coupling scheme

In Chapter 3.2.1, assumptions are made to represent the propeller blades by body force field and mass source field. In order to determine these field functions, the BEM solver can be used. On the other hand, the BEM solver requires the effective wake field to determine the boundary condition for the perturbation potential field, as shown in Equation (3.6). This effective wake field can be calculated by subtracting the propeller-induced flow from the total flow. As a result, the data flow inside the BEM/RANS scheme can be shown as in Figure 3.5. It can be seen that both solvers depend on the results from the other solver and, therefore, an iterative scheme is required for the scheme to converge.
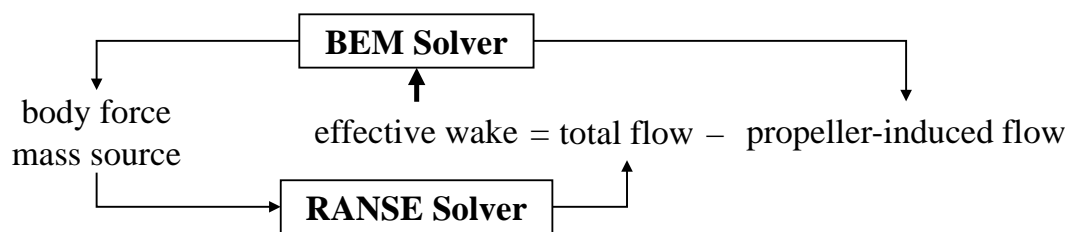
Figure 3.5: Data flow inside the BEM/RANS approach.

The scheme can be implemented in three different ways: unsteady, steady non-axisymmetric, and steady axisymmetric. The difference between the three is given in Table 3.1. The unsteady scheme couples the unsteady RANS solver with an unsteady non-periodical BEM solver. It does not impose any requirement on the upstream bodies and incoming flows. The non-axisymmetric scheme couples the steady 3-dimensional RANS solver with unsteady periodical BEM solver. It requires the nominal wake of the propeller to be steady so that the propeller performance is periodic. This requirement can be further defined as a zero-ship-hull-acceleration condition and a steady-incident-flow condition. The axisymmetric scheme couples the steady axisymmetric RANS solver with a steady

BEM solver. It requires the nominal wake of the propeller to be steady and axisymmetric so that the propeller performance is a constant. This requirement can be further defined as an axisymmetric-upstream-body condition, a zero-acceleration condition, and a steady-axisymmetric-incident-flow condition.

Comparisons of the body force field, mass source field, and effective wake field will be given in greater details in Chapter 3.3 – 3.5.

Scheme	Unsteady	Non-axisymmetric	Axisymmetric
RANS solver type	unsteady 3D	steady 3D	axisymmetric 2D
BEM solution	non-periodical	unsteady periodical	steady
Body force field[2]	function of x, r, θ, t	function of x, r, θ	function of x, r
Upstream body	no requirement	zero-acceleration	zero-acceleration axisymmetric shape
Inflow requirement	no requirement	steady inflow	steady axisymmetric

Table 3.1 Comparison of the unsteady scheme, the non-axisymmetric scheme, and the axisymmetric scheme.

3.2.3 Unsteady BEM/RANS scheme

Figure 3.6 shows the algorithm for the unsteady BEM/RANS scheme:

---

[2] The same applies to mass source field and effective wake field as well.
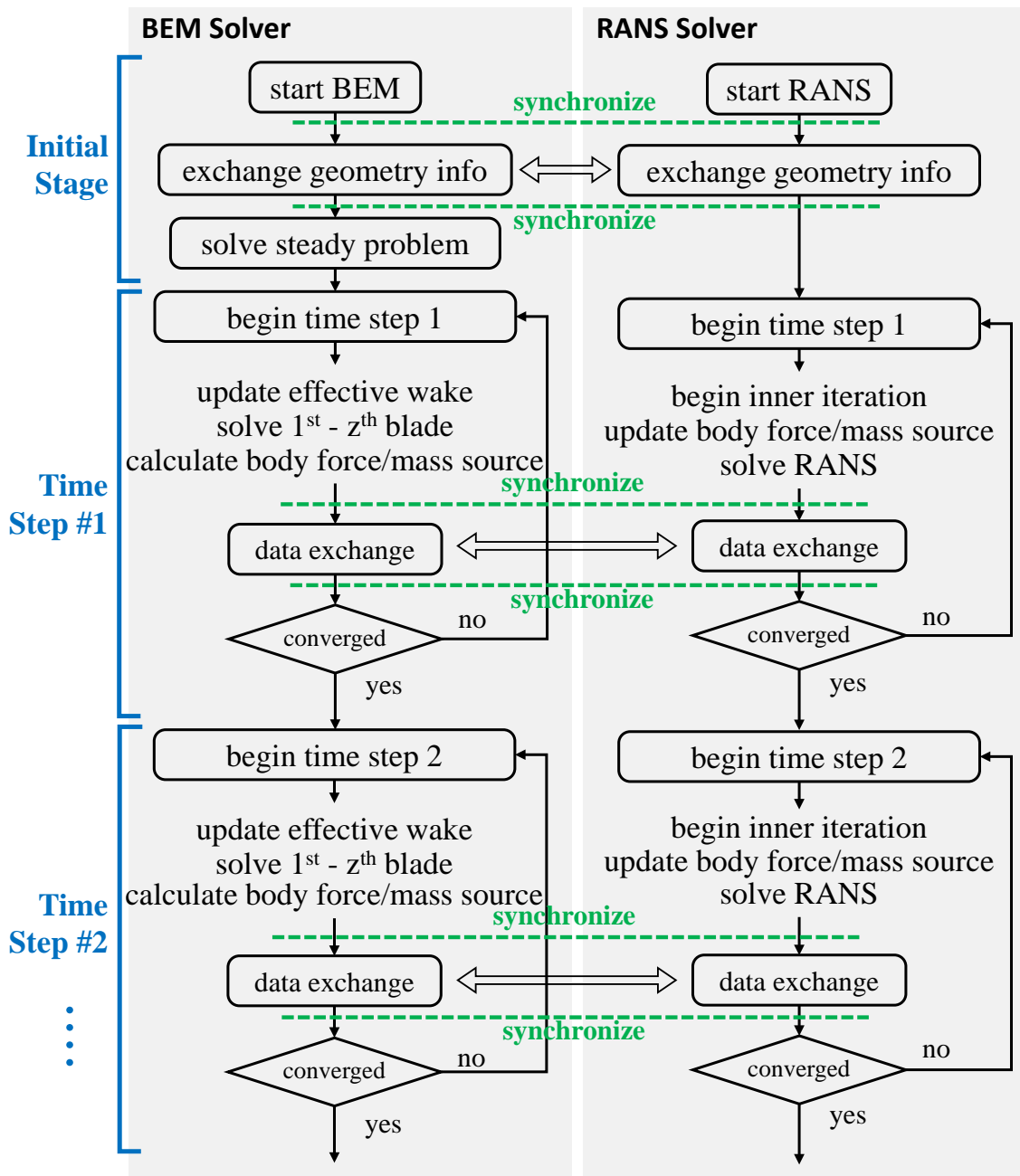
Figure 3.6: Flow chart for the unsteady BEM/RANS scheme.

As shown in the figure, the BEM solver and the RANS solver start by exchanging geometry information and calculating interpolation parameters between the RANS mesh

and the BEM panels. Then, the steady BEM solution is calculated based on a uniform incoming flow condition. The solution provides the initial body force strength and mass source strength for unsteady RANS.

Currently, the BEM solver and the RANS solver must have the same time step size. This restriction can be removed so that the RANS solver can have a larger time step size than BEM. This topic is a part of the future work.

Within each time step, both the BEM solver and the RANS solver use inner iterations to achieve the converged solution. The body force field, mass source field, and effective wake field data are exchanged between the two solvers multiple times within a time step. In other words, an implicit time-stepping is used for updating these three terms. More specifically, the body force term and the mass source term are calculated via the Crank-Nicolson scheme. The use of unsteady time-stepping schemes is important for maintaining numerical stability at large time step sizes. In some test versions of the unsteady BEM/RANS scheme where the explicit time-stepping schemes are used, the numerical convergence is always a big issue.

The number of inner iterations between data exchanges should be determined to minimize the overall computational cost to achieve numerical convergence. Three factors need to be considered: the data exchange cost, the load balancing between the two solvers, and the convergence rate.

The BEM/RANS scheme will terminate the current time step and proceed to the next time step when certain convergence criteria are met. Aside from the convergence criteria imposed by the RANS solver, a new condition is added with respect to the overall propeller thrust force:

$$\left| \frac{T_N - T_O}{T_{ini}} \right| < 10^{-5} \qquad\qquad (3.37)$$

where T_N and T_O are the thrust force at the current and the previous time step; T_{ini} is the thrust force predicted in the steady BEM step.

In the unsteady BEM/RANS approach, the BEM solver and the RANS solver run simultaneously and exchange data multiple times during the process. This requires some special techniques to ensure the data integrity and the data exchange efficiency. Semaphores and shared memory are used in this application. Detailed information about synchronization and inter-process communication are given in Appendix A.

The mesh zone that contains the body force in the unsteady BEM/RANS scheme is also designed in a special way so that the body force field is confined to one layer of cells. This reduces the body force/mass source interpolation error and increases the accuracy of the effective wake field. More details about the body force zone mesh can be found in Appendix B.

3.2.4 Steady non-axisymmetric and steady axisymmetric BEM/RANS scheme

The non-axisymmetric scheme and the axisymmetric scheme can be implemented in the same way, as shown in Figure 3.7. The only differences between the two schemes are the type of BEM solvers used, the type of RANS solvers used, and whether the body force field, mass source field, and effective wake field are circumferentially averaged.

The steady RANS problem can be seen as a single-step unsteady RANS simulation with an infinite time step size. It only takes 5-9 iterations for the BEM/RANS scheme to achieve the converged state. Because of this, there is no need to run BEM and RANS

simultaneously. We can simply call the RANS solver the BEM solver in a sequential and repetitive manner until the solution converges.
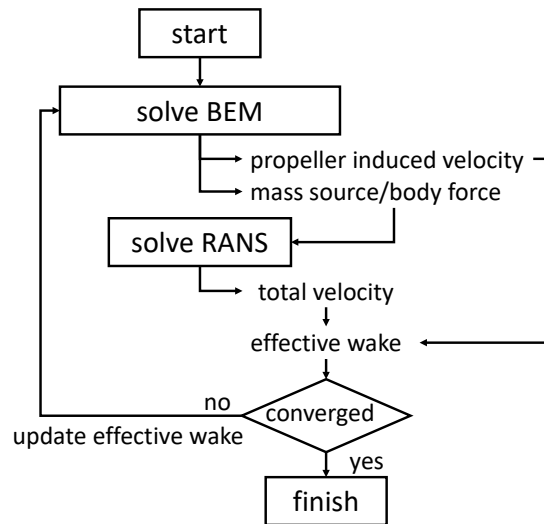
Figure 3.7: Flow chart for the non-axisymmetric BEM/RANS scheme and the axisymmetric BEM/RANS scheme.

3.2.5 Difference between the unsteady BEM/RANS scheme and the immersed boundary method

The major similarity between the unsteady BEM/RANS scheme and the immersed boundary scheme is the use of the body force field to represent the internal wall boundaries. Although the BEM/RANS method can be called a special type of immersed boundary method, there are actually several major differences between the unsteady BEM/RANS approach and the basic form of the immersed boundary method.

- First, the way to determine the body force field is different. The immersed boundary method uses either the feedback forcing approach or a direct forcing approach to

38

determine the body force field (Mittal and Iaccarino 2005, Lai and Peskin 2000, Balaras 2004). In the unsteady BEM/RANS approach, the body force field is determined by an external BEM solver.

- The immersed boundary method relies on the string function (feedback forcing approach) or a pressure reconstruction step (direct forcing approach) to determine the pressure distribution on the boundary. In the BEM/RANS approach, the propeller forces are determined by the BEM solver using the Bernoulli equation.

- To handle high Reynolds number flows immersed boundary method usually refines the mesh near the wall boundary in order to resolve the boundary layer velocity profile. In the unsteady BEM/RANS scheme, the boundary layer is not represented in the RANS solver. Instead, a boundary layer correction can be made to the BEM solver. This reduces the number of cells in the propeller zone and enables larger time step sizes.

- The immersed boundary method does not use source terms in the continuity equation.

3.3 BODY FORCE CALCULATION

The body force term contains three components: normal pressure, skin friction, and the compensating force. The way to calculate the first two components is described in this part and the compensating force will be discussed together with the thickness blockage effect in Chapter 3.4.

3.3.1 Existing studies

To represent the propeller blades by body force field, there are mainly two different approaches: the surface-distribution approach and the mean-camber-distribution approach.

The surface-distribution approach uses either a direct interpolation scheme, as shown in Figure 3.8 (left), or a smooth distribution function, as shown in Figure 3.8 (right), to distribute the surface pressures on the BEM panels to the surrounding finite volume cells. The direct interpolation scheme distributes the pressure on a BEM panel using its intersection areas/volumes with the finite volume cells (Choi 2001). The distribution function method, however, uses a smooth function to distribute the body force to the surrounding cells within a certain range (Gaggero 2017).
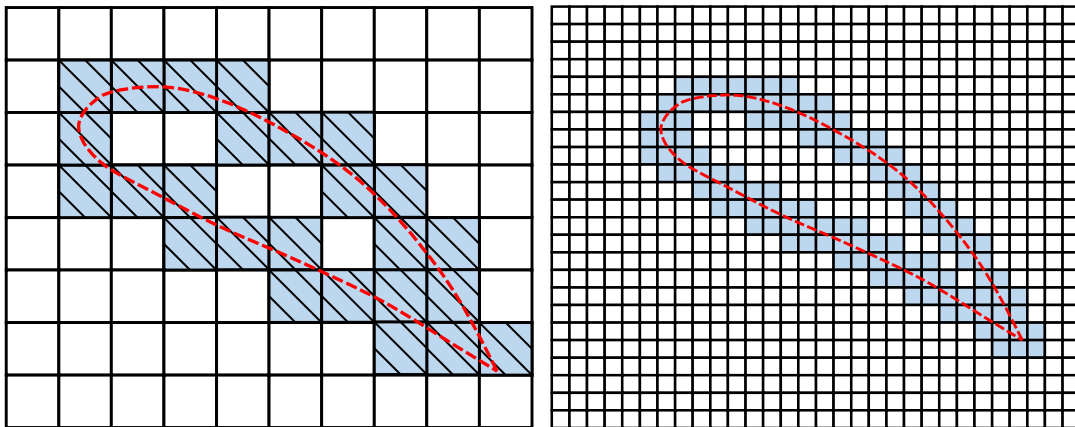
Figure 3.8: A 2D example of the surface-distribution body force model with direct interpolation method (left) or distribution function method (right). The red dashed curve is a 2-dimensional hydrofoil. The body force is applied to all the shadowed cells.

The camber-distribution approach adds an additional step before the force is distributed. The normal pressure and skin friction on both sides of the blade (called pressure side and suction side) is first combined in a conservative way, as shown in Equation (3.38) and Figure 3.9. Then, the combined force field is distributed from the mean camber panels

to the finite volume cells with either the direct interpolation method (Choi 2001) or the distribution function method (Salvatore 2015, Calcagni 2017), as shown in Figure 3.10.

$$\vec{F}_{\text{camber}} = \vec{F}_{\text{pressure}} + \vec{F}_{\text{suction}} \tag{3.38}$$
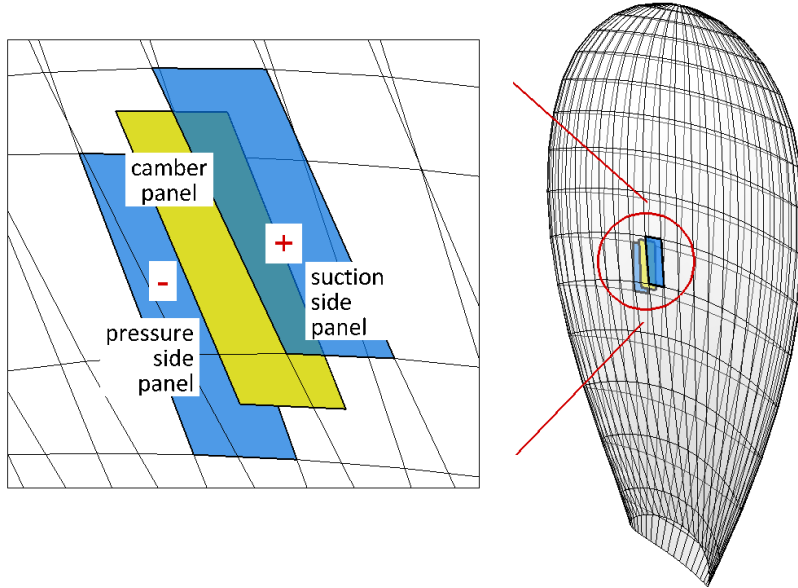
Figure 3.9: Calculation of the combined force field on the blade mean camber surface.

Choi (2001) studied the difference between the surface-distribution approach and the camber-distribution approach on a 2-dimensional hydrofoil solved by an Euler solver. The direct interpolation method is used to distribute the forces to finite volume cells. Results are compared with BEM solutions. The study shows that both the surface-distribution model and the camber-distribution model can accurately represent the hydrofoil. The error of the total flow velocity away from the foil is always less than 1%. However, due to the lack of mesh granularity, the velocity near the foil surface (or camber surface) is not accurate.

41
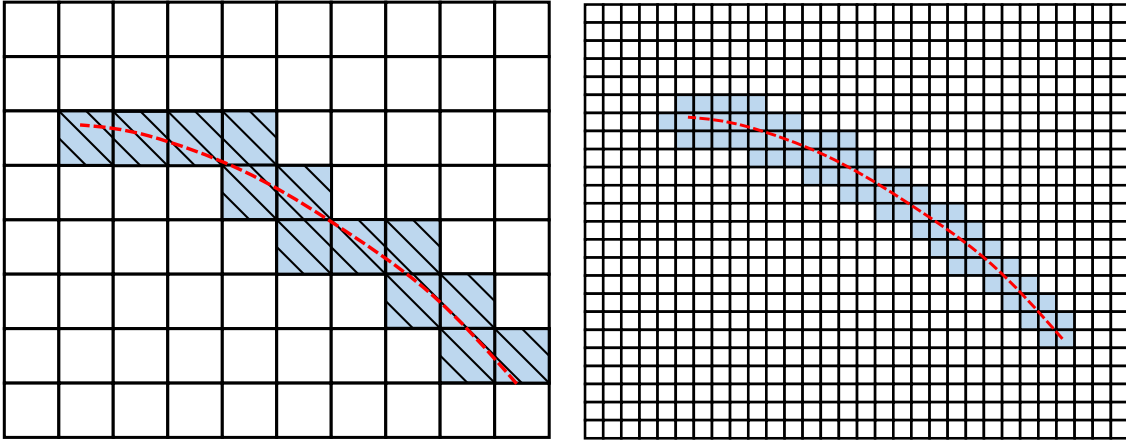
Figure 3.10: A 2D example of the camber-distribution body force model with direct interpolation method (left) or distribution function method (right). The red dashed curve is the camber line of a 2-dimensional hydrofoil. The body force is applied to all the shadowed cells.

3.3.2 Body force calculation in the unsteady BEM/RANS scheme

The surface-distribution approach requires a higher mesh density than the camber-distribution approach because it requires at least two layers of cells inside the blade thickness. Therefore, in order to reduce the number of cells in the propeller zone, the camber-distribution approach is adopted in the unsteady BEM/RANS scheme. The direct interpolation scheme is also used to support the calculation of effective wake close to the propeller blade.

The body force in the unsteady BEM/RANS scheme can be calculated by the following steps:

First, the normal pressure and skin friction on both sides of the blade is summed, as shown in Equation (3.39). In the BEM model, a structured surface mesh is used to represent the propeller blade, as shown in Figure 3.1. p is the static pressure; f is the skin friction; $\vec{q}/|q|$ is the unit vector in the flow direction; $\vec{n}$ is the normal vector; + and –

represent the suction side panel and pressure side panel respectively, as shown in Figure 3.9; S is the area of the panel. As shown in Figure 3.9, the forces on the suction side panel and the forces on the pressure side panel can be summed to obtain the equivalent force $\vec{F}_C$ on the mean camber panel.

$$\vec{F}_C(t) = \left(p\vec{n}S - f\frac{\vec{q}}{|q|}S \right)^+ + \left(p\vec{n}S - f\frac{\vec{q}}{|q|}S \right)^- \tag{3.39}$$

The force is then distributed to one or multiple finite volume cells based on the intersection volume, as shown in Equation (3.40). V_i and $\vec{\mathcal{F}}_i$ are the volume and the body force strength of the i-th finite volume cell; $\vec{F}_C^{\,j}$ is the total force at the j-th camber panel; V_j is the volume defined by sweeping the j-th mean camber panel by the angle of propeller rotation during a time step and can be calculated by Equation (3.41); V_j^i is the intersecting volume between the i-th finite volume cell and the swept volume V_j. In Equation (3.41), S_C is the area of the camber panel; Δt is the time step size; $\vec{n}_j$ is the normal vector of the camber panel; $\vec{n}_j^{\,\theta}$ is the unit vector in the circumferential direction; R_j is the centroid radius of the i-th cell; M is the number of mean camber panels on all blades; N is the number of finite volume cells.

$$\vec{\mathcal{F}}_i(t) = \frac{1}{V_i} \sum_j^M \frac{V_j^i}{V_j} \vec{F}_C^{\,j}(t) \tag{3.40}$$

$$V_j = \sum_i^N V_j^i = S_j \frac{2\pi V_S}{J_S D} \Delta t \left(\vec{n}_j \bullet \vec{n}_j^{\,\theta} \right) R_j \tag{3.41}$$

3.3.3 Body force calculation in the non-axisymmetric BEM/RANS scheme

In the non-axisymmetric version of the BEM/RANS scheme, the time-average of Equation (3.40) should be used to calculate the body force field, as shown in Equation (3.42). Here, the force on the camber $\vec{F}_C^{\,j}$ is a function of the blade angle, instead of time; V_j^T is the volume defined by sweeping the j-th mean camber panel by 2π and can be calculated via Equation (3.43); V_j^i is the intersection volume between the i-th finite volume cell and the swept volume V_j^T.

$$\vec{\mathcal{F}}_i = \frac{\Delta t}{t_{rev}} \frac{1}{V_i} \sum_j^M \frac{V_j^i}{V_j} \vec{F}_C^{\,j}(\theta_i) = \frac{1}{V_i} \sum_j^M \frac{V_j^i}{V_j^T} \vec{F}_C^{\,j}(\theta_i) \tag{3.42}$$

$$V_j^T = 2\pi R_j S_j \left(\vec{n}_j \bullet \vec{n}_j^{\,\theta} \right) \tag{3.43}$$

3.3.4 Body force calculation in the axisymmetric BEM/RANS scheme

In the axisymmetric version of the BEM/RANS scheme, the circumferential average of Equation (3.42) should be used to calculate the body force field, as shown in Equation (3.44). Here, the force on the camber $\vec{F}_C^{\,j}$ is no longer a function of blade angle; A_i is the area of the i-th finite volume cell; A_j is the area of the X-R projection of the j-th mean camber panel and can be calculated by Equation (3.45); A_j^i is the intersection area between the i-th finite volume cell and the projection of j-th mean camber panel.

$$\vec{\mathcal{F}}_i = \frac{1}{A_i} \sum_j^M \frac{A_j^i}{A_j} \vec{F}_C^{\,j} \tag{3.44}$$

$$A_j = S_j \left(\vec{n}_j \bullet \vec{n}_j^{\,\theta} \right) \tag{3.45}$$

3.4 THICKNESS BLOCKAGE EFFECT

3.4.1 Calculation of mass source term

The calculation of the mass source term is very similar to the calculation of the body force term. The BEM sources on both sides of the blade are first combined, as shown in Equation (3.46). In this equation, + and – represent the suction side panel and pressure side panel respectively, as shown in Figure 3.9. Then, this source term can be distributed to finite volume cells based on the direct interpolation scheme.

$$\vec{Q}_C(t) = \left(\frac{\partial \phi}{\partial n}\right)^+ + \left(\frac{\partial \phi}{\partial n}\right)^- \tag{3.46}$$

In the unsteady BEM/RANS scheme, the mass source field can be calculated by Equation (3.47) while V_j is calculated by Equation (3.41).

$$\vec{\mathcal{Q}}_i(t) = \frac{1}{V_i} \sum_j^M \frac{V_j^i}{V_j} \vec{Q}_C^j(t) \tag{3.47}$$

In the non-axisymmetric BEM/RANS scheme, the mass source field can be calculated by Equation (3.48) and V_j is calculated by Equation (3.43).

$$\vec{\mathcal{Q}}_i = \frac{1}{V_i} \sum_j^M \frac{V_j^i}{V_j^T} \vec{Q}_C^j(\theta_i) \tag{3.48}$$

In the axisymmetric BEM/RANS scheme, the mass source field can be calculated by Equation (3.49) and A_j is calculated by Equation (3.45).

$$\vec{\mathcal{Q}}_i = \frac{1}{A_i} \sum_j^M \frac{A_j^i}{A_j} \vec{Q}_C^j \tag{3.49}$$

45

3.4.2 Calculation of compensating force term

When the mass source term is included in the continuity equation, the conservative form of the convection term in the incompressible momentum equation can be written to the non-conservative form by the following way:

$$\rho \partial_j (U_i U_j) = \rho U_i \partial_j U_j + \rho U_j \partial_j U_i = \rho U_i \mathcal{Q} + \rho U_j \partial_j U_i \qquad (3.50)$$

Here, $\rho U_j \partial_j U_i$ is the non-conservative form of the convection term; $\rho U_i \mathcal{Q}$ is a force term induced by the added/subtracted mass sources and is called the "Lagally force". Depending on the implementation of the RANS solver, this term may reduce the local velocity when mass is added and increase the local velocity when mass is subtracted. To eliminate this effect, an extra body force field should be included wherever the mass source term is none-zero. The compensating force field can be calculated by Equation (3.51).

$$\vec{\mathcal{F}}_p = \rho \vec{q} \mathcal{Q} \qquad (3.51)$$

3.5 EFFECTIVE WAKE CALCULATION

As shown in Figure 3.5, the effective wake is calculated by subtracting the propeller-induced velocity from the total velocity. The calculation of the total velocity is straight-forward because it just requires an interpolation of the RANS solution. The calculation of the propeller-induced velocity is based on Equation (3.12) and can actually be implemented in several different ways. Another important aspect is the location where the effective wake is calculated.

In this part, different schemes for calculating the effective wake field are described. The comparison between different effective wake schemes will be given in Chapter 4.

3.5.1 Effective wake calculation in the unsteady BEM/RANS approach

Theoretically, the best location to evaluate the effective wake field is exactly on the blade surface. However, according to Chapter 3.3.1, the RANS solution is not accurate close to the propeller blade due to the lack of mesh density.

In the existing unsteady BEM/RANS applications, the effective wake is usually evaluated at an upstream disk (Chase et al. 2013, Calcagni 2017). This disk can either be a planer disk, as shown in Figure 3.11, or a curved disk that conforms to the shape of the propeller leading edge. This scheme avoided the region where the RANS solution is not accurate but also introduced additional numerical errors because it constrains the change of the effective wake field in the axial direction. As a result, the effective wake can be inaccurate near the trailing edge of the propeller.
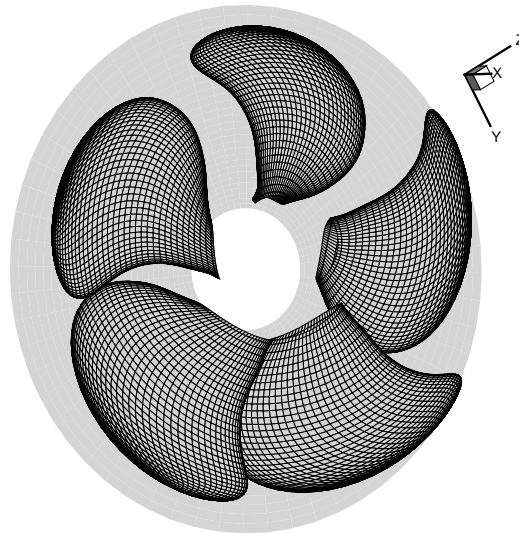
Figure 3.11: An example of evaluating the effective wake at a planar upstream disk in the unsteady BEM/RANS scheme.

In this application, the above issues are solved by evaluating the effective wake at a small constant offset from the propeller blade control points. To implement this idea, two different approaches are tested:

- Calculating effective wake on a constant offset from the blade surface

In this application, the effective wake velocity for the j-th BEM panel is evaluated at the location X_j^E defined by a constant distance offset from the panel centroid X_j^P, as shown in Figure 3.12 and Equation (3.52). In the equation, $\vec{n}_j$ is the normal vector of the j-th BEM panel and d is the offset distance.

$$\vec{X}_j^E = \vec{X}_j^P + \vec{n}_j d \tag{3.52}$$
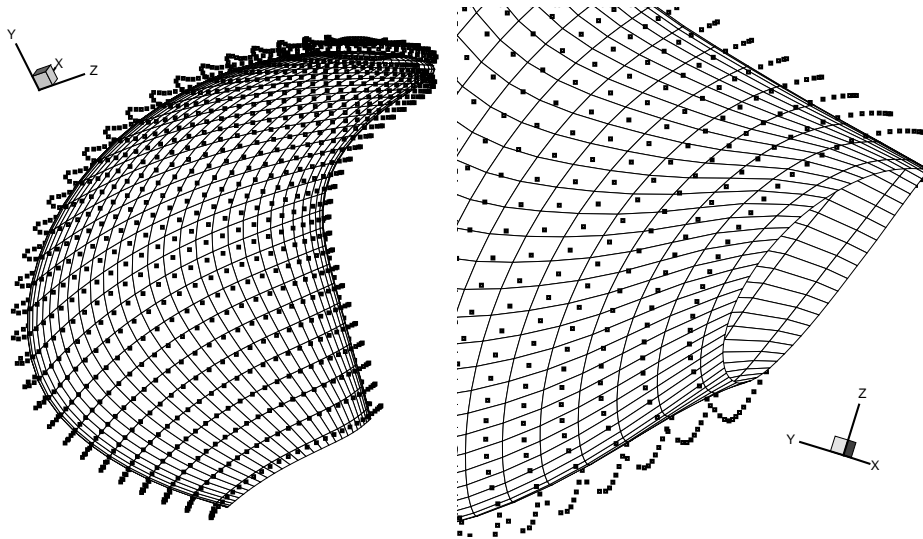
Figure 3.12: Calculation of effective wake velocity at a constant offset from the blade surface. The left figure is a global view of the blade while the right figure is a close-up view of the blade base station. The black points are where the effective wake is evaluated.

48

To evaluate the induced velocity on these points, the Equation (3.12) can be used. In this equation, S_B includes the blade surface and the hub surface.

The offset distance d is an important parameter in this scheme. If d is too small, the total velocity from RANS is not accurate due to the lack of mesh density; the calculated propeller-induced velocity from Equation (3.12) is not accurate as well because of the "saw-tooth effect" (Kinnas and Hsin 1994). If the offset distance is too large, the calculated wake field cannot accurately represent the flow near the propeller blade and, thus, create a numerical error. A parametric study on choosing the offset distance is given in Chapter 4.

- Calculation of effective wake based on the mean camber geometry

In this application, the effective wake velocity for the j-th BEM panel is evaluated at the location X_j^E defined by a constant distance offset from the corresponding mean camber panel centroid X_j^C, as shown in Figure 3.13 and Equation (3.53). In the equation, $\vec{n}_j^C$ is the normal vector of the mean camber panel and d is the offset distance. The $\pm$ symbol is the equation is determined by which side (pressure side or suction side) is the j-th BEM panel located.

$$\vec{X}_j^E = \vec{X}_j^C \pm \vec{n}_j d \qquad (3.53)$$

In this approach, the blade-induced velocity can still be calculated by Equation (3.12). However, the boundary S_B in this equation needs to be changed in order to be consistent with the locations where the effective wake is calculated. Therefore, instead of integrating over the blade surfaces, the mean camber surfaces are used to calculate the blade-induced velocity. In other words, S_B includes the mean camber surfaces and the hub surface. The source and dipole strength on a mean camber panel can be determined by the

summation of the sources and dipoles from the blade surface panels on both sides of the camber panel, as shown in Equation (3.54). In this equation, A^+, A^-, and A^C are the areas of the suction side surface panel, pressure side surface panel, and mean camber panel. $\mathcal{S}^+$, $\mathcal{S}^-$, and $\mathcal{S}^C$ are can be the source strength or dipole strength of the suction side surface panel, pressure side surface panel, and the mean camber panel

$$\mathcal{S}^C = \frac{A^+}{A^C}\mathcal{S}^+ + \frac{A^-}{A^C}\mathcal{S}^- \qquad (3.54)$$
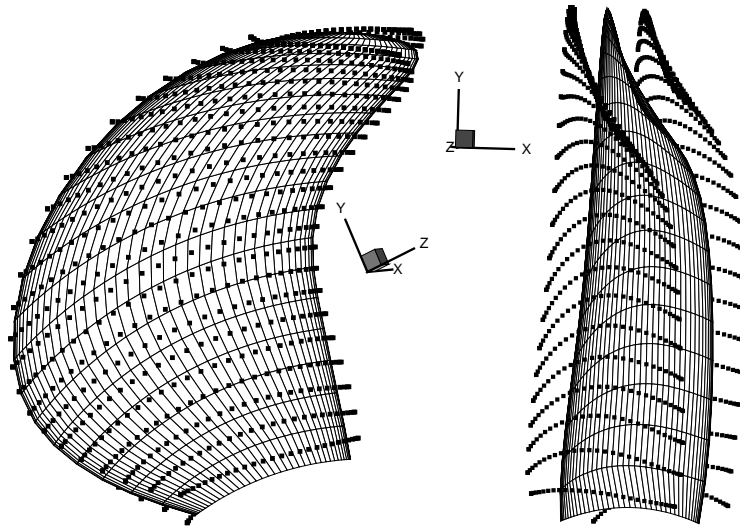
Figure 3.13: Calculation of effective wake velocity at a constant offset from the blade mean camber surface. The left figure is a global view of the blade camber surface while the right figure is a side view of the camber surface. The black points are where the effective wake is evaluated.

3.5.2 Effective wake calculation in the non-axisymmetric BEM/RANS approach

In the non-axisymmetric BEM/RANS scheme, the effective wake can be evaluated either at an upstream disk, as shown in Figure 3.11, or at the centroids of the blade surface panels, as shown in Figure 3.14. The upstream disk model constrains the change of the effective wake field along the axial direction and this can cause numerical errors. According to Tian (Tian et al. 2014), evaluating the effective wake on the propeller blade surface can improve the numerical accuracy for various types of propellers.

It is worth noting that although the effective wake is always evaluated on the blade surface, the effective wake can still change with the blade angle.
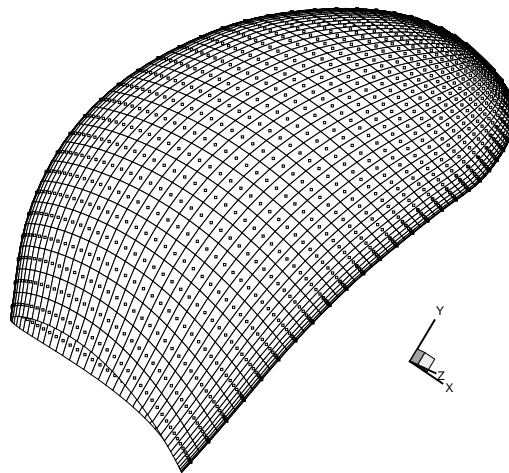
Figure 3.14: An example of evaluating the effective wake at the centroids of blade surface panels in the non-axisymmetric BEM/RANS scheme.

Unlike the unsteady BEM/RANS scheme, in the non-axisymmetric BEM/RANS scheme, we can either neglect or avoid the numerical errors in calculating the total flow velocity and propeller-induced velocity close to the propeller blade. This is why it is possible to evaluate the effective wake exactly on the blade surface. The following paragraphs explain why those errors can be neglected.

Since RANS solves for the time-averaged problem, the body force field and mass source field are distributed to the whole propeller region instead of a few layers of cells. This time-average reduces the numerical error in the unsteady approach due to the lack of local mesh granularity.

According to the previous description, the error in calculating the near-field blade-induced velocity is due to the "saw-tooth" effect. To avoid this numerical error, the propeller-induced velocity on the blade surface can be evaluated via another way, as shown in Equation (3.55) - (3.57). Here, ξ and η are the chord-wise and the span-wise panel directions; n is the panel normal direction.

$$\vec{q}_\xi = \frac{\partial \phi}{\partial \xi} \tag{3.55}$$

$$\vec{q}_\eta = \frac{\partial \phi}{\partial \eta} \tag{3.56}$$

$$\vec{q}_n = -\vec{q}_e \cdot \vec{n} \tag{3.57}$$

In the non-axisymmetric BEM/RANS scheme, RANS solves for the time-averaged total flow while BEM solves for the unsteady propeller-induced flow under the time-averaged effective wake field. To calculate the time-averaged effective wake, the unsteady propeller-induced flow should be time-averaged first and subtracted from the total flow.

There are two possible ways to calculate the time-averaged propeller-induced flow velocity $\vec{q}$:

- **Average the propeller-induced velocity within a blade passing period, including the period when the target point is inside the blade thickness.** As shown in Equation (3.58), $\vec{q}^{(R)}$ and $\vec{q}^{(S)}$ are the time-accurate propeller-induced

52

velocity defined in the rotational coordinate system and in the ship coordinate system; Z is the number of blades, T is the propeller revolution period, and ω is the angular velocity; ψ_0 is an arbitrary angle that can be chosen based on the propeller panel geometry to simplify the integration process. This equation converts the time integral into a spacial integral so that it is more straight-forward to implement in the PROPCAV solver. It is worth noting that according to the BEM theory, the propeller-induced velocity $\vec{q}^{(R)}$ is zero inside the propeller blade thickness.

$$
\begin{aligned}
\vec{q}(x,r,\theta) &= \frac{Z}{T}\int_0^{\frac{T}{Z}}\vec{q}^{(S)}(x,r,\theta,t)\,dt \\
&= \frac{Z}{T}\int_0^{\frac{T}{Z}}\vec{q}^{(R)}(x,r,\theta+\omega t,t)\,dt \\
&= \frac{Z}{2\pi}\int_{\psi_0}^{\psi_0+\frac{2\pi}{Z}}\vec{q}^{(R)}(x,r,\psi,t_0)\,d\psi
\end{aligned}
\tag{3.58}
$$

$$
t_0 = \frac{\psi-\theta}{\omega}
\tag{3.59}
$$

- **Average the propeller-induced velocity within a blade passing period, NOT including the period when the target point is inside the blade thickness.** As shown in Equation (3.60), the only change is the range in which the averaging is performed. Here, ψ_0 and ψ_1 are the angular range of the fluid domain between to nearby propeller blades, as shown in Figure 3.15.

$$
\vec{q}(x,r,\theta) = \frac{1}{\psi_1-\psi_0}\int_{\psi_0}^{\psi_1}\vec{q}^{(R)}(x,r,\psi,t_0)\,d\psi
\tag{3.60}
$$
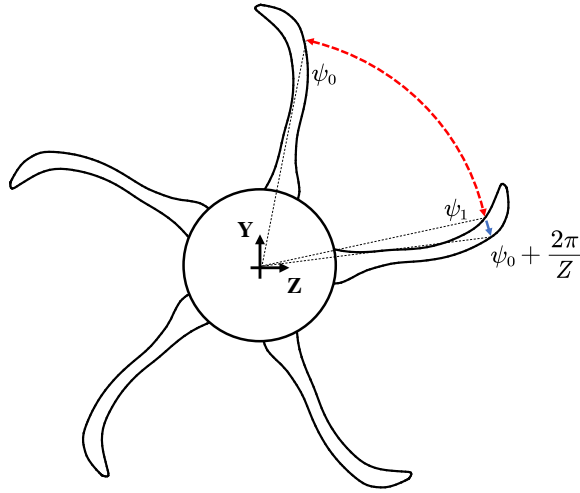
Figure 3.15: Two possible range of integration in calculating the time-averaged propeller-induced velocity for the non-axisymmetric and axisymmetric BEM/RANS scheme.

Numerical study about the two different averaging schemes is given in Chapter 4.

3.5.3 Effective wake calculation in the axisymmetric BEM/RANS approach

In the axisymmetric BEM/RANS scheme, the effective wake can be evaluated either at an upstream curve or at the centroids of the blade surface panels, as shown in Figure 3.16. The effective wake is both time-averaged and circumferentially-averaged.

In the axisymmetric BEM/RANS scheme, the RANS solver determines the steady axisymmetric total flow while BEM solves for the steady propeller-induced flow under an axisymmetric effective wake field. To calculate the axisymmetric effective wake, the propeller-induced flow should be circumferentially-averaged before it is subtracted from the total flow, as shown in Equation (3.61) or (3.62), where $\psi = \theta + \omega t$.
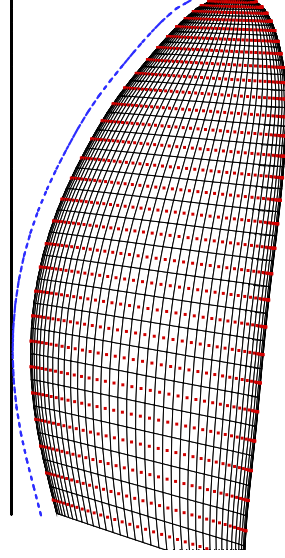
Figure 3.16: Three different methods to evaluate the effective wake in the axisymmetric BEM/RANS scheme: at an upstream straight line (solid line), at an offset from the blade leading edge (dashed line), and at the centroids of blade surface panels (points).

$$
\begin{aligned}
\vec{\bar{q}}\left(x,r\right) &= \frac{1}{2\pi}\frac{Z}{T}\int_0^{2\pi}\int_0^{\frac{T}{Z}}\vec{q}^{(S)}\left(x,r,\theta,t\right)dt\,d\theta \\
&= \frac{1}{2\pi}\frac{Z}{T}\int_0^{2\pi}\int_0^{\frac{T}{Z}}\vec{q}^{(R)}\left(x,r,\theta+\omega t,t\right)dt\,d\theta \\
&= \frac{1}{2\pi}\frac{Z}{2\pi}\int_0^{2\pi}\int_{\psi_0}^{\psi_0+\frac{2\pi}{Z}}\vec{q}^{(R)}\left(x,r,\psi,t_0\right)d\psi\,d\theta \\
&= \frac{Z}{2\pi}\int_{\psi_0}^{\psi_0+\frac{2\pi}{Z}}\vec{q}^{(R)}\left(x,r,\psi,t_0\right)d\psi \quad \forall t_0\in[0,T]
\end{aligned}
\tag{3.61}
$$

$$
\vec{\bar{q}}\left(x,r\right) = \frac{1}{\psi_1-\psi_0}\int_{\psi_0}^{\psi_1}\vec{q}^{(R)}\left(x,r,\psi,t_0\right)d\psi \quad \forall t_0\in[0,T]
\tag{3.62}
$$

Chapter 4.   Numerical Study and Validation

In this chapter, several simple test cases are solved to validate the BEM/RANS approach. Numerical and parametrical studies are also made on whether to include the thickness blockage effect and on which is the better way to evaluate the effective wake. In order to make the problem simpler for the numerical and parametrical studies, the multibody interaction is not included in any of these cases. More realistic applications on the multibody interaction problems are given in Chapter 5.

To make it easier to distinguish between different numerical scheme, the following terms are defined:

- BEM: the propeller performance is solved by the boundary element solver under the nominal wake. The interaction between the potential flow and the incoming vortical flow is not considered.

- BEM/RANS: the propeller performance is solved by the coupled BEM/RANS approach. The propeller blades are represented by body force field and mass source field in the RANS model. The scheme can be used to determine the effective wake and to handle the multibody interaction problem. The scheme can be unsteady, non-axisymmetric, or axisymmetric.

- RANS: (or called "full-blown RANS") the propeller performance is solved by RANS solver with the propeller represented by non-slip wall boundaries. The scheme can be used to handle multibody interaction problem and can be used as a reference to validate the BEM/RANS scheme.

---

[*] The data in chapter 4.2 and 4.3 are published in (Su and Kinnas 2017a). The data in chapter 4.4 and 4.5 are published in (Su and Kinnas 2018). The dissertator is the primary author of both papers.

4.1 DEFINITION OF NON-DIMENSIONAL NUMBERS

The non-dimensional numbers that are used in this chapter and in the next chapter include:

- Thrust coefficient K_T is the non-dimensional thrust force generated by the whole propeller unit. In contrast, the thrust coefficient generated by a single blade is written as $K_T^{(1)}$. In a contra-rotating propeller (CRP) case, the thrust coefficient of the forward propeller and the aft propeller are K_{TF} and K_{TA} respectively. All these thrust coefficients are calculated by Equation (4.1). In this equation, ρ is the flow density, D the propeller diameter, n is the propeller r.p.s. (revolution per second), and T is the thrust force. In the definition of the aft propeller K_{TA} in the CRP case, the forward propeller diameter is used.

$$K_T = \frac{T}{\rho n^2 D^4} \tag{4.1}$$

- Torque coefficient K_Q is the non-dimensional torque generated by the propeller unit. In contrast, the torque coefficient generated by a single blade can be written as $K_Q^{(1)}$. In a CRP case, the torque coefficient of the forward propeller and the aft propeller are K_{QF} and K_{QA} respectively. All these torque coefficients are defined by Equation (4.2). In the definition of the aft propeller K_{QA} in the CRP case, the forward propeller diameter is used.

$$K_Q = \frac{Q}{\rho n^2 D^5} \tag{4.2}$$

57

- Pressure coefficient C_p is the non-dimensional pressure and can be defined by Equation (4.3). In this equation, P is the pressure that is non-dimensionalized and P_0 is the far upstream pressure.

$$C_p = \frac{P - P_0}{\frac{1}{2}\rho n^2 D^2} \tag{4.3}$$

- Advance ratio J_S quantifies the angular velocity of the propeller compared to the ship speed V_S.

$$J_S = \frac{V_S}{nD} \tag{4.4}$$

- Non-dimensionalized circulation G_S represents the loading at a certain station of the propeller blade. It is defined by Equation (4.5) where R is the propeller max radius and Γ is the blade velocity circulation at a certain station.

$$G_S = \frac{100\Gamma}{2\pi R V_S} \tag{4.5}$$

4.2 PROPELLER P5168 IN UNIFORM INFLOW SOLVED BY AXISYMMETRIC BEM/RANS

4.2.1 Description of the problem

In this application, the five-blade skewed propeller P5168, as shown in Figure 4.1 is used with a uniform incoming flow (nominal wake). The P5168 propeller is a representation of the current propeller designs. The inflow velocity is in the direction of the shaft axis. Different advance ratios are used ranging from 0.8 to 1.0.

58

According to Chapter 3.1.4, if the nominal wake is irrotational, the predicted effective wake should be the same as the nominal wake. This condition can be used to validate the BEM/RANS scheme. In other words, although there is no need to use the BEM/RANS approach in a uniform inflow case, the solution of BEM/RANS scheme reveals how much error is introduced by the assumptions in Chapter 3.2.1.
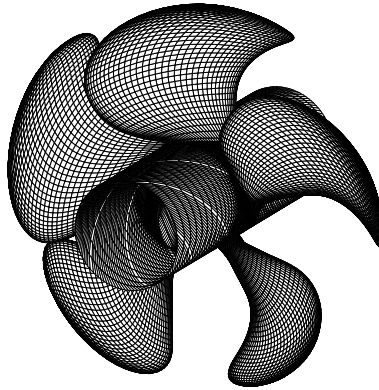
Figure 4.1: BEM panel model of the P5168 propeller.

4.2.2 Description of the numerical model

The axisymmetric BEM/RANS scheme is used to solve this problem. The steady BEM solver is coupled with the steady axisymmetric RANS solver.

In the BEM model, as shown in Figure 4.1, 80×36 panels are placed on the key blade surface while 70×20 panels are used for the hub surface between two blades. A PSF-2 type wake alignment scheme is used (Greeley and Kerwin 1982).

The axisymmetric RANS model includes 46,000 quadrilateral cells which cover a computational domain from -1.5D to 2.0D in the axial direction and 2.0D in the radial direction, as shown in Figure 4.2. The inflow velocity is set at the upstream boundary; a

slip-wall condition is set on the hub surface; a zero-gradient condition is used for all the flow variables at the downstream boundary. The mesh is refined at the propeller zone where body force and mass source are applied, as shown in Figure 4.3. Other settings for the axisymmetric RANS model are listed in Appendix C.

By default, when calculating the time-averaged propeller-induced velocity, the period when the target point is inside the blade thickness is NOT included. This is the second method in Chapter 3.5.2 and 3.5.3.
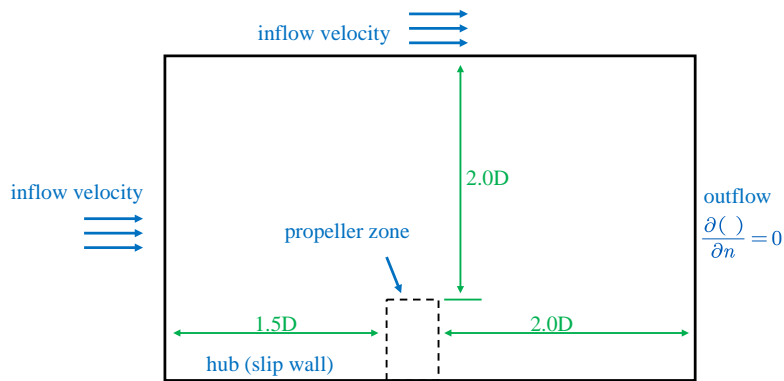
Figure 4.2: Boundary conditions and the range of computational domain of the axisymmetric RANS model.
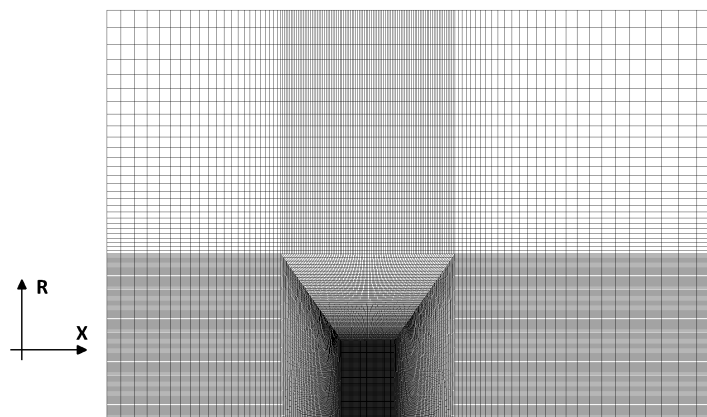
Figure 4.3: The RANS mesh used in the axisymmetric BEM/RANS scheme.

4.2.3 Validation of the axisymmetric BEM/RANS scheme

In this test, the advance ratio is set to Js=0.8. The axisymmetric BEM/RANS scheme is used to determine the effective wake field. Since we expect the effective wake to be the same as the nominal wake, only one BEM/RANS iteration is performed.

First, a mesh convergence study is made on the number of BEM panels and on the number of RANS cells. As shown in Table 4.1, a higher-mesh-density case and a lower-mesh-density case are tested. The circulations after the first iteration are compared, as shown in Figure 4.4. Very little difference can be observed. This validates the mesh independence.

The higher-mesh-density settings are used for further studies. The predicted effective wake on the blade is plotted in the X-R domain, as shown in Figure 4.5. For the most part of the blade, the error of the predicted effective wake is within 3%. The major difference occurs at the root of the blade and at the tip of the blade. The error near the root can be explained by the "saw-tooth" effect in calculating the hub-induced velocity. This causes a numerical error in the propeller-induced velocity near the hub panels. The error near the tip of the blade may be explained by the inaccurate tip vortex geometry. It is still challenging for potential solvers to handle propeller tip flows. But the good news is the error at the root and tip does not influence the overall propeller performance much.

	BEM blade panels	RANS cells
Higher mesh density	80×36	46,000
Lower mesh density	60×20	28,000

Table 4.1: Number of cells/panels used in the mesh convergence study.
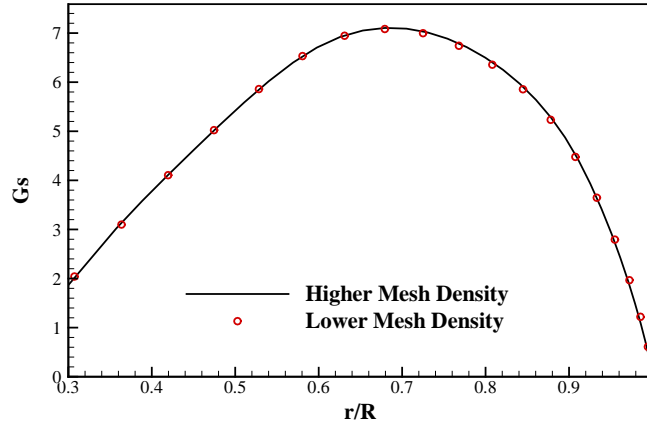
Figure 4.4: Comparison of the blade circulation distribution predicted from the higher-mesh-density case and from the lower-mesh -density case.
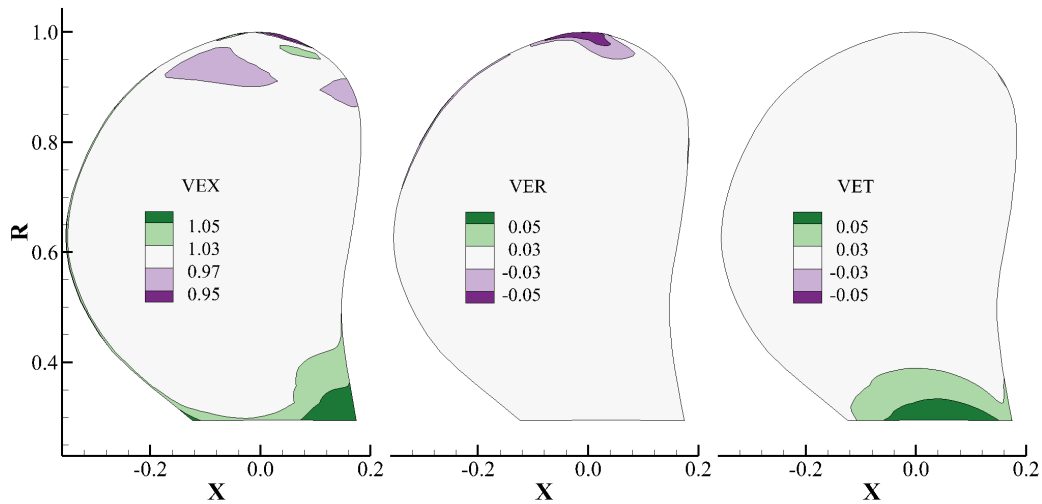
Figure 4.5: (Scheme A) Effective wake velocity components in the axial (left), radial (middle), and swirl (right) direction. The velocity is non-dimensionalized by q_e/V_S. White color means a less than 3% numerical error.

4.2.4 Study of the Thickness Blockage Effect

To study the thickness blockage effect, 4 slightly different BEM/RANS schemes are used to solve the P5168 propeller with uniform inflow. As shown in Table 4.2, the

differences between the 4 schemes include whether the mass source term is added to the continuity equation, whether the compensating force is added to the momentum equation, and how the time- and circumferentially-averaged propeller-induced velocity is calculated.

First, advance ratio Js=0.8 is used. The effective wake field predicted by the 4 different schemes are shown in Figure 4.5 - Figure 4.8 respectively.

	Mass source	Compensating force	Averaging range
Scheme A	Included	Included	Include the part inside a blade
Scheme B	Included	NOT included	Include the part inside a blade
Scheme C	NOT included	NOT included	Include the part inside a blade
Scheme D	Included	Included	NOT include the part inside blade

Table 4.2: Differences between the four cases in the thickness blockage effect study.
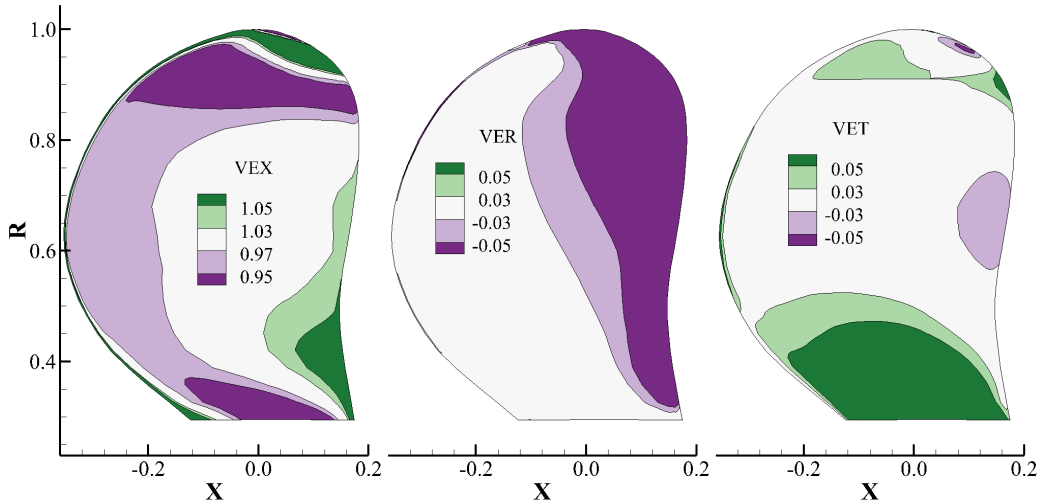
Figure 4.6: (Scheme B) Effective wake velocity components in the axial (left), radial (middle), and swirl (right) direction. The velocity is non-dimensionalized by q_e/V_S. White color means a less than 3% numerical error.
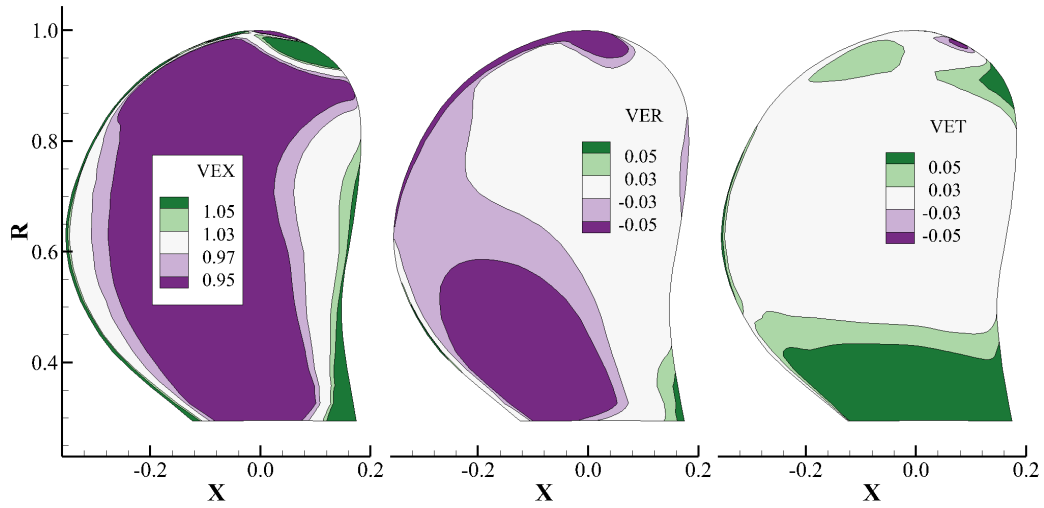
Figure 4.7: (Scheme C) Effective wake velocity components in the axial (left), radial (middle), and swirl (right) direction. The velocity is non-dimensionalized by q_e/V_S. White color means a less than 3% numerical error.
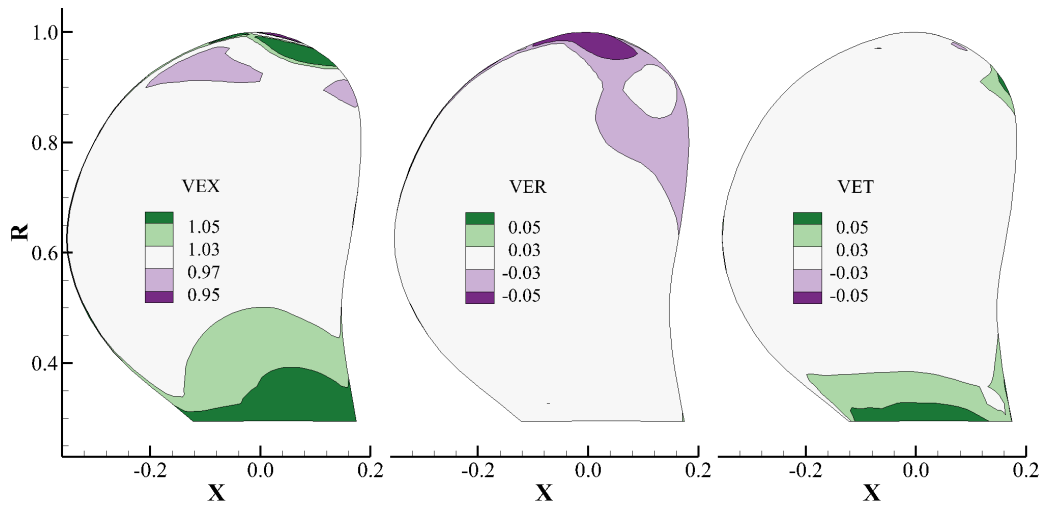
Figure 4.8: (Scheme D) Effective wake velocity components in the axial (left), radial (middle), and swirl (right) direction. The velocity is non-dimensionalized by q_e/V_S. White color means a less than 3% numerical error.

Among all the 4 schemes, the most accurate effective wake field is predicted by scheme A in which both the mass source and the compensating force are included and the propeller-induced velocity is time-averaged in between two blades.

In scheme B, the compensating force term is removed from RANS but the mass source term is still included. The predicted effective wake is shown in Figure 4.6. Due to the thickness distribution, the Lagally force tends to decelerate the axial flow at the forward part of a blade and accelerate the axial flow at the aft part. Therefore, an underpredicted axial flow is expected in the axial component effective wake velocity (left plot of Figure 4.6).

In scheme C, both the mass source and the compensating force are removed from RANS. The predicted effective wake is shown in Figure 4.7. Without the thickness blockage effect, the axial component of the total flow is expected to be smaller. This leads to an underpredicted axial effective wake velocity, as depicted in the left plot of Figure 4.7.

Based on the above observations, it can be concluded that both the mass source term and the compensating force term are essential and should be included in the RANS model. Next, the different methods for calculating the time-averaged propeller-induced velocity are looked at.

Both scheme A and scheme D included the mass source term and compensating force term. The only difference between the two schemes is the way how the propeller-induced velocity is time-averaged. Scheme A averages the velocity only in between the blades while scheme D also includes the part inside the blade thickness where the propeller-induced velocity is zero. Details about the two methods can be found in Chapter 3.5.2 and 3.5.3.

As shown in Figure 4.8, the effective wake predicted by scheme D has a larger numerical error than that from scheme A, especially at the root of the blade. This is because

the blade thickness is largest at the root. Therefore, including the zero-velocity region inside the blade reduces the propeller-induced velocity in the axial direction and, thus, increase the axial component of the effective wake near the root of the blade.

To explain why the blade thickness region should not be included in calculating the time-averaged propeller-induced flow, the effect of the BEM source term should be first examined. In a vortex lattice representation of a propeller blade, the streamline follows the mean camber surface. When source terms are also added to the model to represent the blade thickness, the streamline is pushed outwards due to the blockage effect. As a result, the velocity in between the blades increases. Back to the BEM representation of the blade, the source on the blade surface panels (thickness blockage effect) causes the flow in between blades to increase and the flow velocity inside the blade thickness to be zero. Therefore, if only the region between two blades is considered, the thickness blockage effect is included in the propeller-induced velocity field. On the other hand, if the blade thickness region is also included, the thickness blockage effect is weakened. Finally, since the thickness blockage effect is included in RANS, it should also be included in the propeller-induced velocity so that the two flow fields are consistent. The consistency between the total flow field and propeller-induced flow field reduces the numerical error of the effective wake, which is calculated by subtracting the propeller-induced flow from the total flow.

In conclusion, in the axisymmetric BEM/RANS scheme, the mass source and compensating force need to be included in RANS. The calculation of the time-averaged propeller-induced flow should only consider the region between the blade and not consider the zero-velocity blade thickness region. The same reasoning should also be true for the time-averaged non-axisymmetric scheme.

The converged blade circulation predicted by scheme A, B and C is also compared. Different advance ratios are tested, including 0.6 (Figure 4.9), 0.8 (Figure 4.10), 1.0 (Figure

4.11). A special case is also solved with a 0.8 advance ratio and a 150% of the design thickness (Figure 4.12).
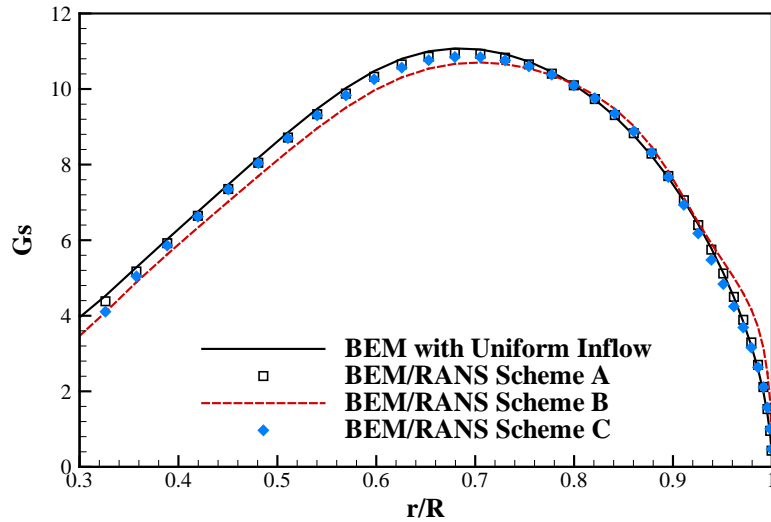
Figure 4.9: Influence of the mass source and compensating force towards the blade circulation at Js=0.6.
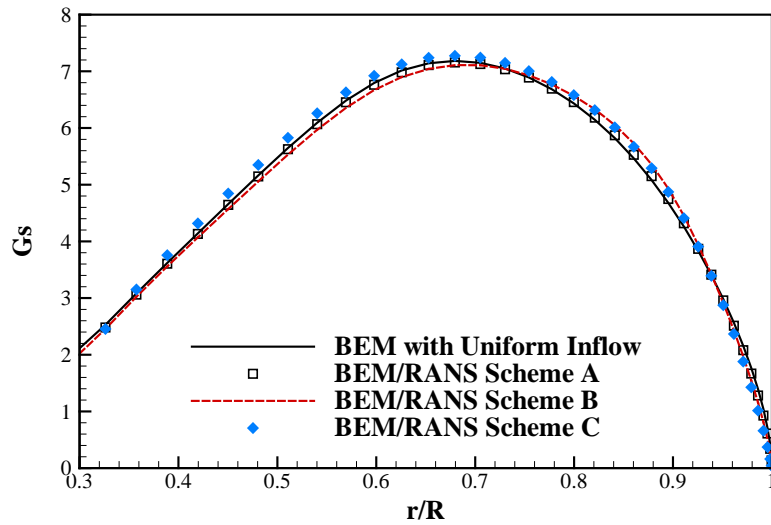
Figure 4.10: Influence of the mass source and compensating force towards the blade circulation at Js=0.8.
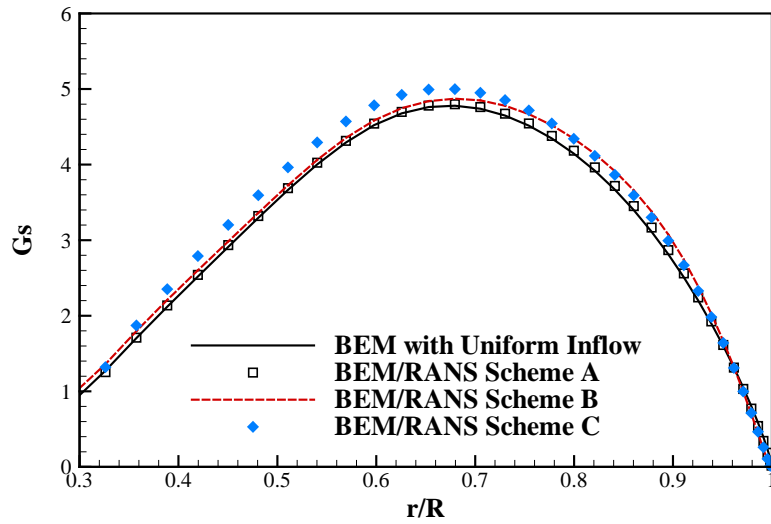
Figure 4.11: Influence of the mass source and compensating force towards the blade
circulation at Js=1.0.
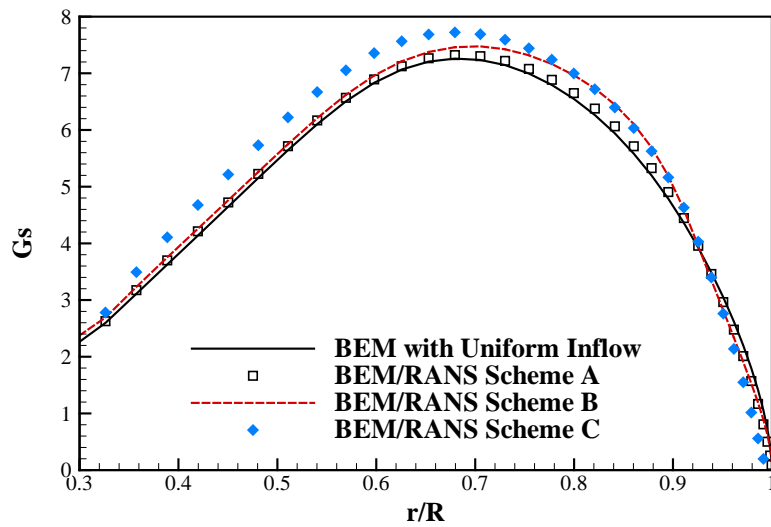
Figure 4.12: Influence of the mass source and compensating force towards the blade
circulation at Js=0.8 with 150% blade thickness.

In every one of the four figures, four circulation distribution curves are compared.

The first curve represents the circulation predicted by PROPCAV under the uniform inflow

(nominal wake) condition. The next three curves are the circulation calculated by PROPCAV under the effective wake predicted by scheme A, B, or C.

According to these figures, the second curve always has the smallest numerical error compared to the first curve. Removing the mass source term can lead to an overestimated blade loading because the absence of the thickness blockage effect causes a weaker effective wake field. This phenomenon is more evident under higher advance ratios or higher blade thickness. The higher advance ratio means a weaker body force field. A thicker blade means a higher mass source field. Both lead to a spurious stronger blockage effect. Removing the compensating force alters the propeller loading distribution along the blade chord-wise direction. However, the overall change of the blade circulation at a certain radius depends on the blade thickness distribution along the chord as well as many other factors. Therefore, there is no clear trend on how the circulation distribution changes if the compensating force is removed.

4.3 PROPELLER P5168 IN AXISYMMETRIC INFLOW SOLVED BY AXISYMMETRIC BEM/RANS

4.3.1 Description of the problem

In order to test how the axisymmetric BEM/RANS scheme behaves with non-uniform inflows, the following test case is designed. The same propeller P5168 is used in this study. The incoming flow (nominal wake) is a nonuniform axisymmetric flow field, defined by Equation (4.6) and (4.7). This nominal wake contains a lower axial velocity region at the smaller radius and a constant velocity outside the propeller region, as shown in Figure 4.13. Such type of wake field can often be found in the downstream of an underwater axisymmetric slender body, including submarines and some other underwater vehicles.

$$\frac{V_X}{V_S} = \begin{cases} 1 - 0.6 \dfrac{1 + \cos\left(\dfrac{\pi r}{R}\right)}{2} & ; \quad \dfrac{r}{R} \leqslant 1 \\[3em] 1.0 & ; \quad \dfrac{r}{R} > 1 \end{cases}$$

(4.6)

$$\frac{V_Y}{V_S} = \frac{V_Z}{V_S} = 0.0$$

(4.7)
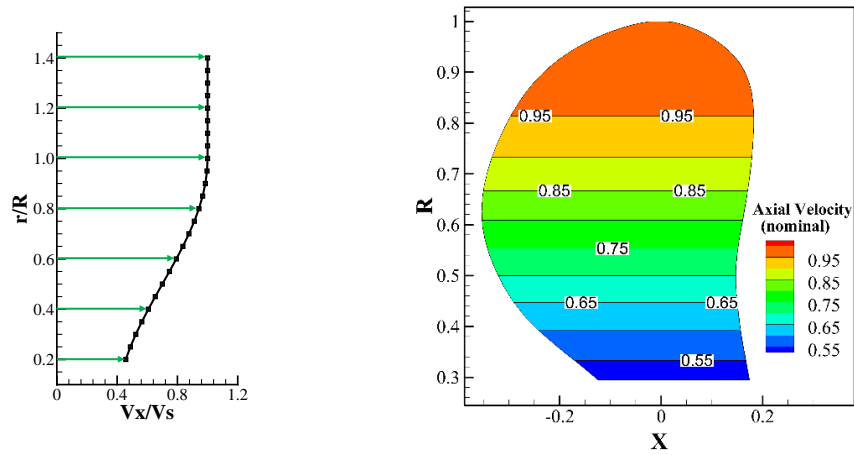
Figure 4.13: Axial velocity profile of the nonuniform axisymmetric inflow (left) and the corresponding nominal wake field plotted on the propeller surface (right).

4.3.2 Description of the numerical models

First, the axisymmetric BEM/RANS scheme is used. The BEM model and RANS model are the same as those described in Chapter 4.2.2. The only difference is that the inflow boundary is set to the above velocity profile. Both the mass source term and the compensating force term are included. The propeller-induced velocity is only averaged in the region between two blades.

To validate the BEM/RANS result, a full-blown RANS simulation is performed for the same case. As shown in Figure 4.14, only 1/5 of the propeller is modeled with around 3 million cells and periodical boundaries. The velocity profile is applied to the inflow boundary. The propeller blade is modeled by non-slip walls while the hub is modeled by a slip-wall. Other settings can be found in Appendix C.
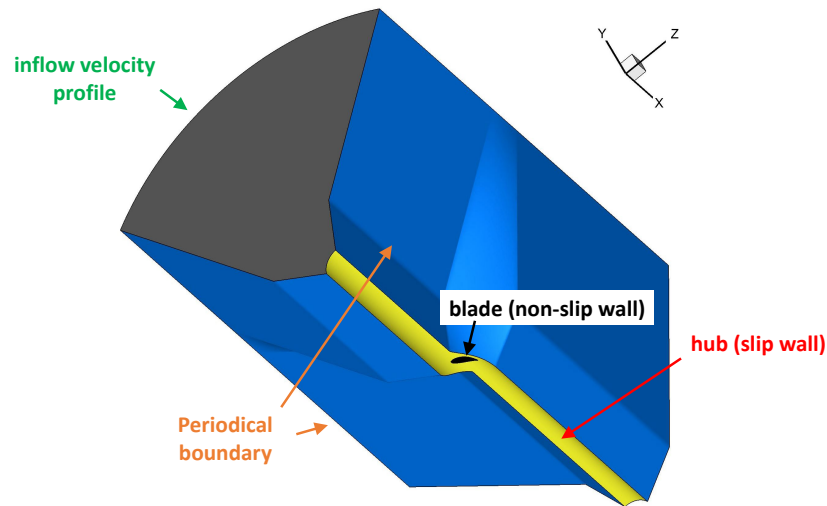
Figure 4.14: Boundaries of the full-blown RANS simulation for propeller P5168 under nonuniform axisymmetric inflow.

4.3.3 Results

In this case, since the inflow is no longer irrotational, the propeller-induced flow may interact with the nominal wake. Therefore, the propeller performance should change with the iterations. As shown in Figure 4.15, the convergence of the BEM/RANS scheme is established at around the fourth iteration. Figure 4.16 shows the body force field and mass source field. Figure 4.17 shows the axial and swirl components of the predicted effective wake. This effective wake field can be compared with the nominal wake, as

shown in Figure 4.13, to illustrate the interaction between the vortical inflow and the propeller-induced flow. In the effective wake, the axial velocity increases at lower radii. The swirl velocity component is also developed. Overall, the propeller makes the flow more evenly distributed.
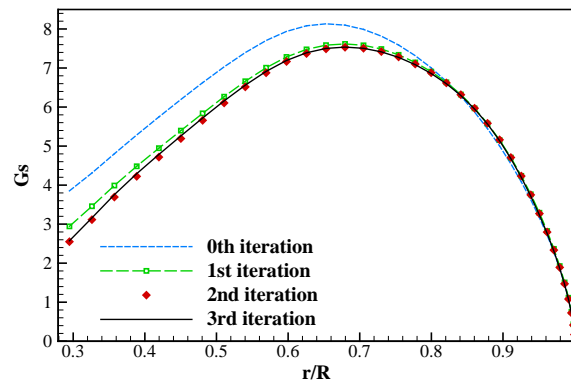
Figure 4.15: Blade circulation distribution at different iterations.
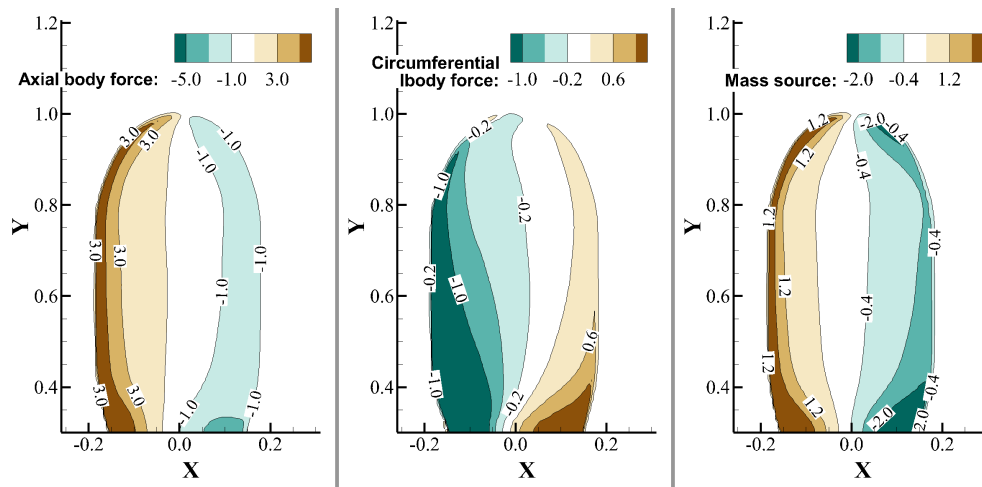
Figure 4.16: Axial body force field (left), circumferential body force field (middle), and mass source field (right) plotted on the X-R projection of the propeller. The blade leading edge is on the left side. The unit of the body force field is $\rho V_S^2/R$ and the unit of the mass source field is $\rho V_S/R$.
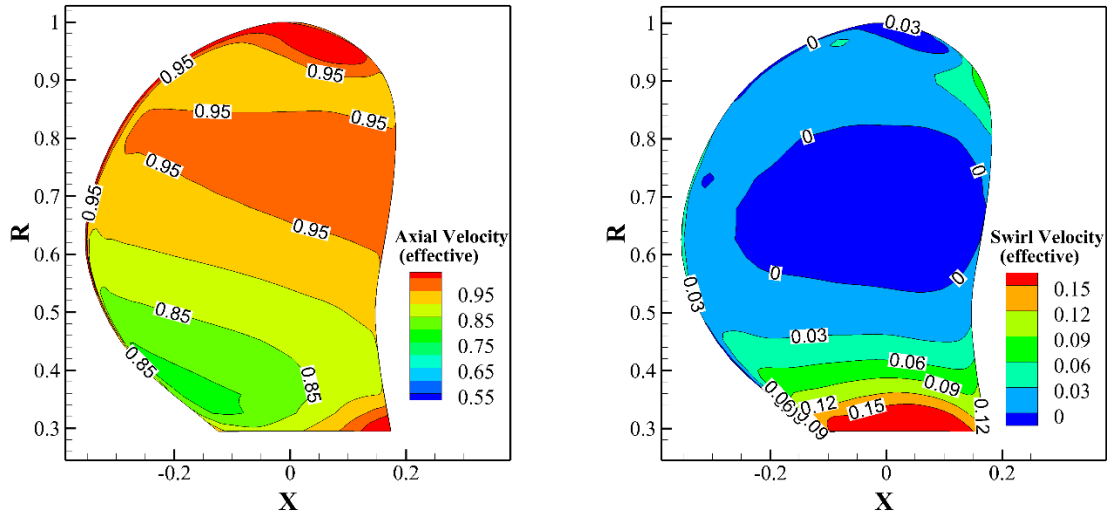
Figure 4.17: Effective wake field $\vec{q}_e/V_s$ predicted by the axisymmetric BEM/RANS
scheme (non-uniform axisymmetric inflow case). The axial (left) and swirl
(right) velocity components are plotted on the X-R projection of the
propeller. The blade leading edge is on the left side.

	Computational Cost (on same machine)	Thrust Coef.	Torque Coef.
BEM (nominal wake)	40 seconds	0.140	0.0198
BEM/RANS	30 minutes	0.158 (13% error)	0.0220 (11% error)
Full-blown RANS	8 hours	0.141 (1.0% error)	0.0197 (0.8% error)

Table 4.3: Comparison of predicted propeller forces and computational cost between
BEM, BEM/RANS, and full-blown RANS.

With the full-blown RANS results as a reference, the BEM/RANS scheme can be

validated. The thrust coefficients and torque coefficients are first compared, as shown in

Table 4.3. When BEM is solved directly with the nominal wake, the predicted propeller

73

forces may have as much as a 13% error compared to the full-blown RANS results. However, after considering the vortical inflow-propeller interaction via the BEM/RANS scheme, the error goes down to less than 1%. The computational cost of all three schemes is also listed in Table 4.3.

4.4 PROPELLER P2772 IN UNIFORM INFLOW SOLVED BY UNSTEADY BEM/RANS

4.4.1 Description of the problem

In this application, a four-blade skewed propeller P2772 at P/D = 0.87, as shown in Figure 4.18, is used with a uniform incoming flow (nominal wake). The inflow velocity is in the direction of the shaft axis. The advance ratio is set to 0.6.
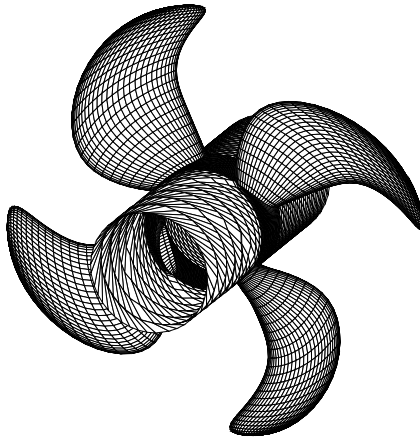
Figure 4.18: BEM panel model of the P2772 propeller.

The original P2772 propeller geometry has a round trailing edge. This makes the Kutta condition hard to implement and also makes the trailing wake surface hard to determine. In order to handle round trailing edge propellers, the propeller geometry needs to be modified. Pan (2011) and Du (2017) developed a trailing edge extension scheme for

the blunt trailing edge duct and blunt trailing edge 2-dimensional foils. The same idea can also be applied to extend the blunt/round propeller trailing edges.
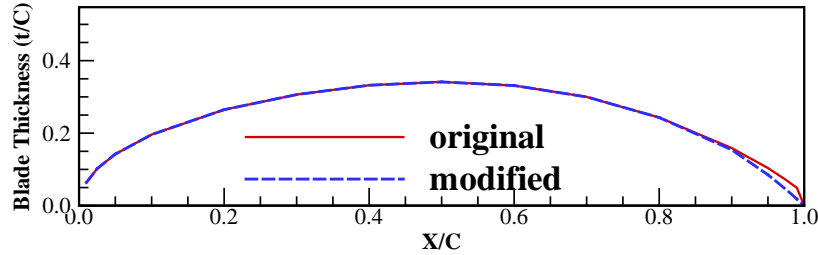
Figure 4.19: Original (solid) and modified (dashed) root section thickness distribution of propeller P2772.

In this dissertation, a simpler method is used which modifies the blade thickness near the trailing edge, as shown in Figure 4.19. For every blade section, assume the original blade thickness distribution is defined by Equation (4.8) where ζ/C is the blade thickness as a ratio to the camber and x/C is the chord-wise coordinate which ranges from 0 to 1.

$$\frac{\zeta}{C} = f\left(\frac{x}{C}\right) \tag{4.8}$$

Equation (4.9) defines the modified thickness distribution while the parameter A and B can be calculated by Equation (4.10). In Equation (4.9), the thickness within the $x/C \in [0.8, 1]$ region is replaced by a second-order polynomial which is determined by two end points and the slope at $x/C = 0.8$.

$$\frac{\zeta}{C} = \begin{cases} f\left(\dfrac{x}{C}\right) & ; \ \dfrac{x}{C} \leqslant 0.8 \\ A\left(\dfrac{x}{C} - 1\right)^2 + B\left(\dfrac{x}{C} - 1\right) & ; \ \dfrac{x}{C} > 0.8 \end{cases} \tag{4.9}$$

75

$$A = -5f'(0.8) - 25f(0.8)$$
$$B = -f'(0.8) - 10f(0.8)$$

(4.10)

Similar to Chapter 4.2.1, the predicted effective wake is expected to be the same as the nominal wake. This serves as a validation for the unsteady BEM/RANS scheme.

4.4.2 Description of the numerical model

The unsteady BEM/RANS scheme is used to solve this problem. The unsteady BEM solver is coupled with the unsteady RANS solver.

In the BEM model, as shown in Figure 4.18, 60×25 panels are placed on the key blade surface while 66×10 panels are used for the hub surface between two blades. A PSF-2 type wake alignment scheme is used.

The unsteady RANS model uses 2,000,000 hexahedron cells that cover a computational domain from -1.5D to 1.5D in the axial direction and up to 2.0D in the radial direction, as shown in Figure 4.20 and Figure 4.21. The inflow velocity is set at the upstream boundary; a slip-wall condition is set on the hub surface; a zero-gradient condition is used for all the flow variables at the downstream boundary. The model consists of two zones. The inner zone is where body force term and mass source term are applied. The cells in the inner zone follow that shape of the mean camber surface. More details about the inner zone can be found in Appendix B. The inner zone rotates with the propeller and is connected to the outer zone via sliding interfaces. Other settings for the RANS model are listed in Appendix C.

The BEM/RANS model is solved for 6 propeller revolutions. A 3-degree equivalent time steps size is used. Here, the equivalent time-step size is defined as the propeller rotation angle during a time step. At the last propeller revolution, the boundary layer

correction is included in the BEM solver. However, the blowing source term is not applied to the RANS model.
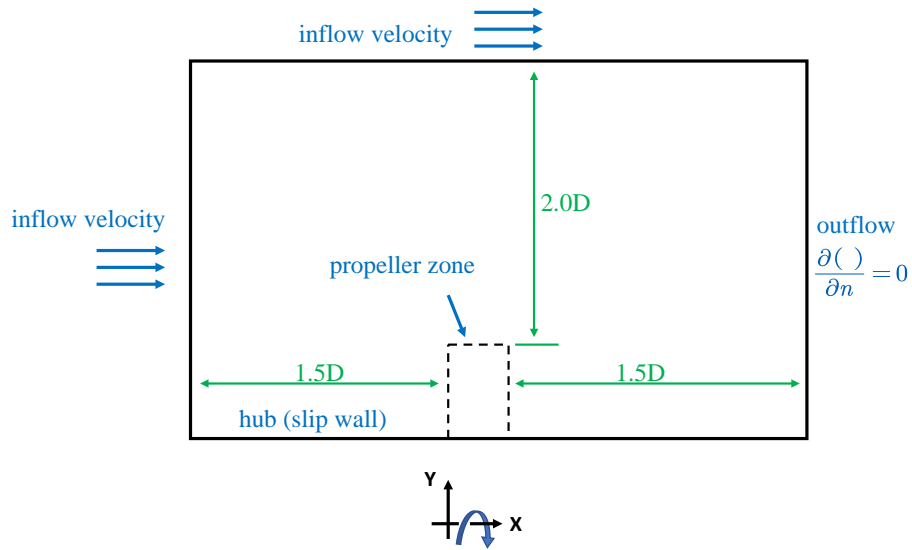
Figure 4.20: Boundary conditions and the range of computational domain of the unsteady RANS model. Only the {z = 0 and y > 0} slice of the 3-dimensional model is shown.
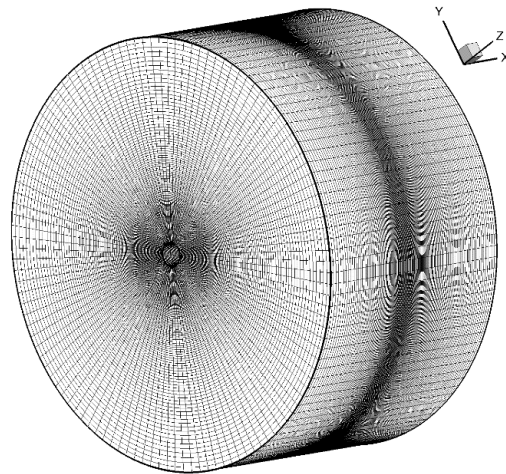
Figure 4.21: The RANS mesh used in the unsteady BEM/RANS scheme.

To validate the unsteady BEM/RANS scheme, an unsteady full-blown RANS simulation is also performed with the same case. In this RANS model, the outer zone remains the same. The inner zone is a full cylindrical zone that contains 1.35 million polyhedral cells and non-slip boundaries to represent the propeller blades. A 1-degree equivalent time step size is used. Other settings in the RANS solver can be found in Appendix C.
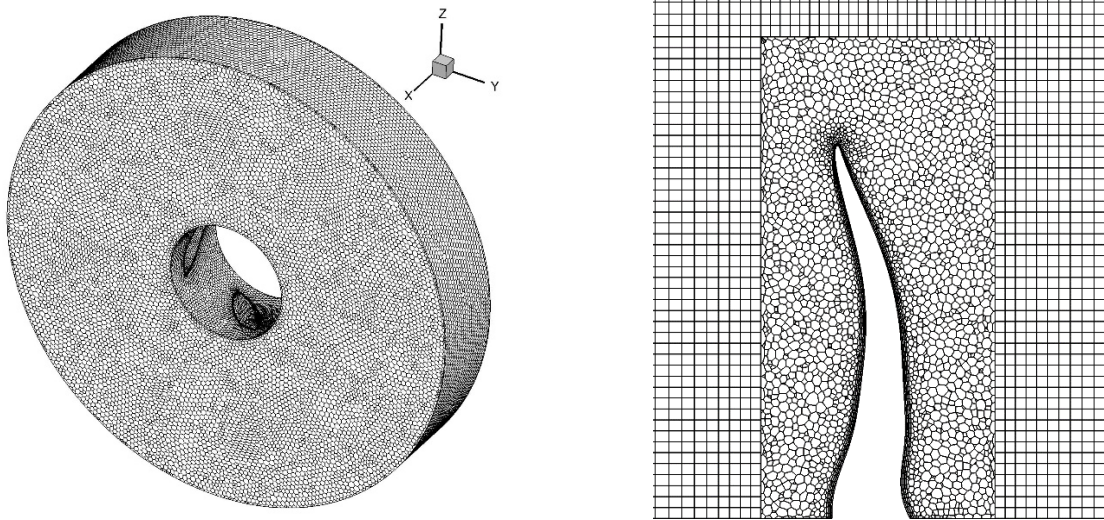
Figure 4.22: The inner mesh zone (left) and its middle slice (y = 0) (right) in the unsteady full-blown RANS simulation.

4.4.3 Numerical study on different effective wake calculation schemes

In Chapter 3.5.1, two different methods are introduced to evaluate the effective wake for the unsteady BEM/RANS scheme. The first method calculates the effective wake based on the propeller blade surface geometry while the second method calculates the effective wake based on the blade mean camber surface.

To determine which method is better, two different cases are tested.

In the first case, the effective wake is evaluated at a constant offset from the blade surface. This means both the total flow velocity and the effective wake velocity are interpolated or calculated at those offset locations. The offset distance is 6% of the propeller diameter. The blade-induced velocity is calculated by an integration over all the blade surface panels. The predicted effective wake field at the mid-chord slice is shown in Figure 4.23.

In the second case, the effective wake is evaluated at a constant offset from the mean camber surface. The offset distance is also 6% of the propeller diameter. The blade-induced velocity is calculated by an integration over all the mean camber panels. The predicted effective wake field at the mid-chord slice is shown in Figure 4.24.

In the unsteady BEM/RANS scheme, the effective wake field is evaluated only at several blade angles where the blades are currently located. In other words, the algorithm does not provide all the data required to generate Figure 4.23 at a certain time step. In fact, the data in Figure 4.23 and Figure 4.24 comes from multiple time steps within the last revolution. That is why a small discontinuity might be observed near the boundary line at around 0-degree blade angle position. This discontinuity is not obvious in this case because the inflow is axisymmetric. It is more noticeable in some later studies when the ship hull acceleration or turning is included.

Based on Figure 4.23 and Figure 4.24, the second method behaves much better than the first method. As shown in Figure 4.24, the effective wake predicted by the second method has very small vertical and horizontal components. On most part of the mid-chord slice, the axial effective wake velocity has a less than 3% error (shown as the white color). At the root of the blade, the error rises to 5%. This might be due to the saw-tooth effect in calculating the hub-induced velocity. On the contrary, in Figure 4.23, the effective wake predicted by the first method has a much larger error in all directions.
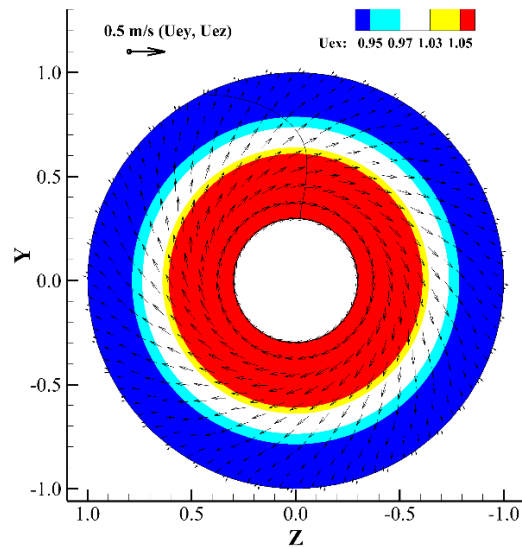
Figure 4.23: The mid-chord effective wake field q_e/V_S predicted by the unsteady BEM/RANS scheme. The effective wake is evaluated based on the blade surface geometry. The axial velocity component is shown by the contour plot while the in-plane velocity components are shown by arrows.
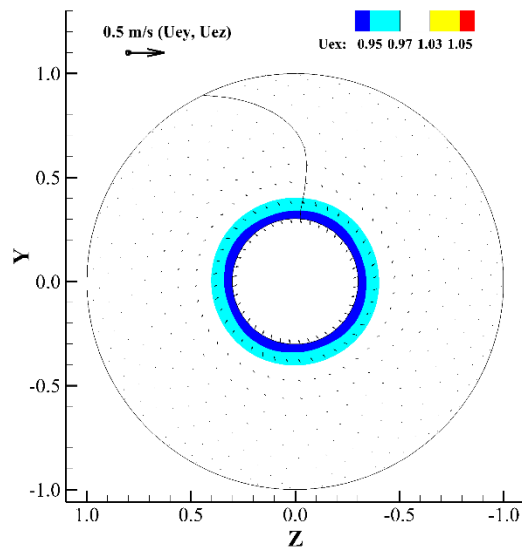
Figure 4.24: The mid-chord effective wake field q_e/V_S predicted by the unsteady BEM/RANS scheme. The effective wake is evaluated based on the blade mean camber surface. The axial velocity component is shown by the contour plot while the in-plane velocity components are shown by arrows.

To explain why the second method behaves better than the first method, the body force model needs to be looked at. In Chapter 3.3.1, two body force models are described: the surface-distribution model and the camber-distribution model. The camber-distribution model is finally chosen because it uses a smaller number of cells in the propeller zone. The camber-distribution model means the propeller's effect on the RANS model (body force and the mass source) is applied at the mean camber location. Since the accurate prediction of the effective wake requires a consistent representation of the propeller blades in both RANS and BEM, the propeller-induced velocity should also be calculated based on the mean camber geometry (second method).

In all future unsteady BEM/RANS calculations, the second way of calculating effective wake field is always used.

Finally, although these two methods predict quite different effective wake field in the unsteady BEM/RANS calculations, the difference might not be significant in time-averaged BEM/RANS calculations (non-axisymmetric scheme and axisymmetric scheme). One possible explanation is that the time-averaging process cancels the numerical error.

4.4.4 Influence of the offset distance in calculating the effective wake field

The offset distance at which the effective wake is calculated is also an important parameter. If the offset distance is too small, both the total flow from RANS and the blade-induced velocity are not accurate[3]. If the offset distance is too large, the calculated wake field might not be able to represent the real effective wake on the propeller surface.

To study how the offset distance affects the numerical result, five cases with different offset distances are tested. The distance ranges from 2% of propeller diameter to

---

[3] Refer to Chapter 3.5.1 for more details.

6% of propeller diameter. The numerical scheme fails to converge in the case with a 2% of diameter offset. The results from the other 4 cases are shown in Figure 4.25. In this figure, the numerical error of the predicted propeller forces is compared. The full-blown RANS result is set as the reference.
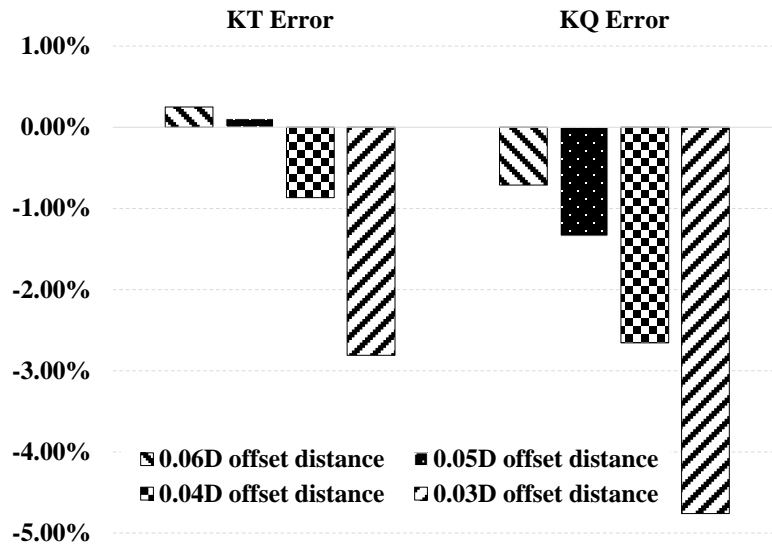
Figure 4.25: Error of the propeller forces predicted by the unsteady BEM/RANS scheme with the effective wake calculated at different offset distances. The full-blown RANS result is set as the reference.

According to the figure, the numerical error decrease as the offset distance increases from 3% to 6% of the propeller diameter. At 6% diameter of offset, the numerical errors of both the thrust coefficient and torque coefficient fall below 1%. Therefore, the 6% of the diameter is chosen as the sweet spot for the offset distance. It is worth noting that this number might change when different BEM panels are used or when a different inner mesh density is used.

In all future unsteady BEM/RANS calculations, the effective wake field is always calculated at an offset of 6% diameter.

4.4.5 Result and comparison

Other results from the unsteady BEM/RANS simulation are shown in this subchapter. Figure 4.26 shows the body force field in all three directions at the $x = 0$ slice of the RANS computational domain.

Figure 4.27 shows the predicted propeller forces as a function of time. There is a huge jump in the propeller loading at the beginning of the scheme. This is due to the starting vortex. As the vortex moves downstream, the propeller performance finally stabilizes after around one blade revolution (120th-time step).

Figure 4.28 compares the blade circulation distribution from the unsteady BEM/RANS scheme and that from the BEM solver with uniform inflow (nominal wake). In the unsteady BEM/RANS, the circulation from the stabilized solution is used. As expected, the difference between the two curves is small.

Figure 4.29 compares the thrust coefficient and torque coefficient predicted by the unsteady BEM/RANS scheme, by the unsteady full-blown RANS, by BEM with the nominal wake, and by experiment.

Figure 4.30 compares the vorticity fields from the unsteady BEM/RANS scheme and from the unsteady full-blown RANS. Six pairs of figures are shown, each representing a different blade angle (time). Within each pair, the top figure shows the vorticity field generated by non-slip wall boundaries (full-blown RANS) while the lower figure shows the vorticity field generated by body force fields and mass source fields (unsteady BEM/RANS).

83
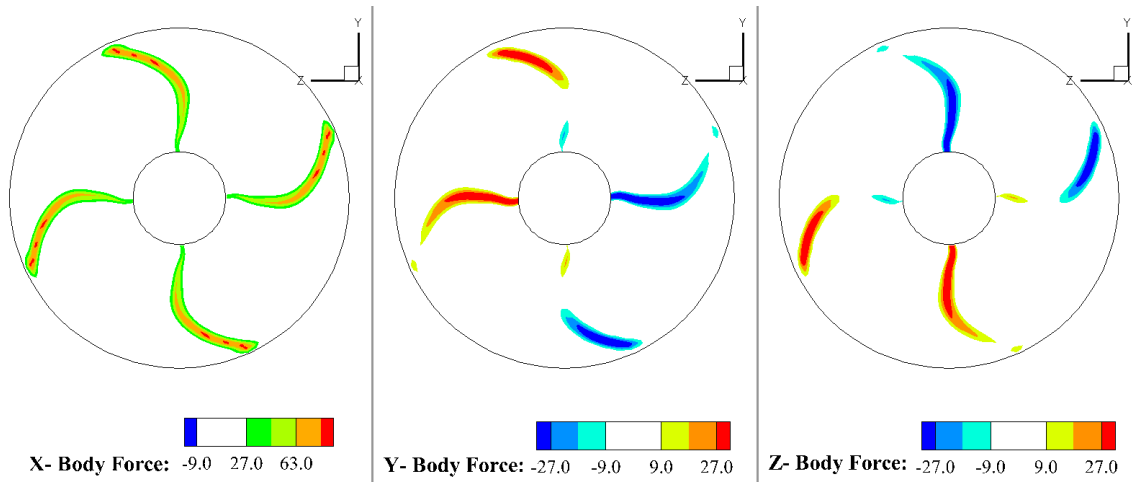
Figure 4.26: Axial body force field (left), vertical body force field (middle), and horizontal body force field (right) plotted at the x = 0 slice of the RANS computational domain. The unit of the body force field is $\rho V_S^2 / R$.
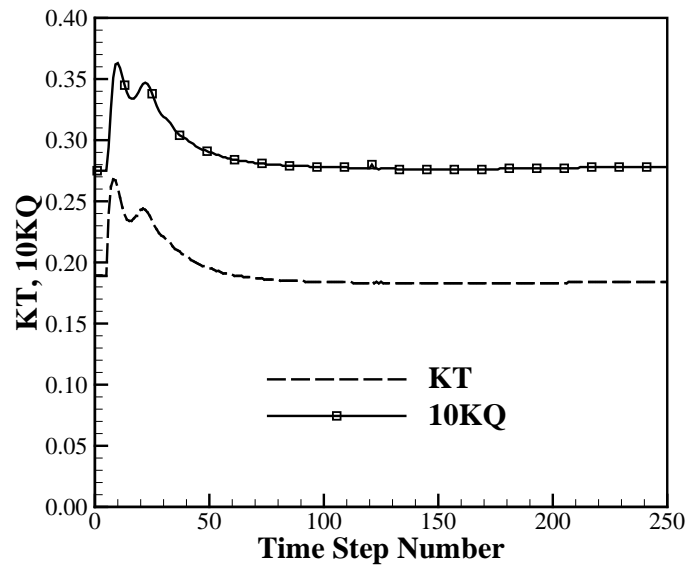
Figure 4.27: The thrust coefficient and torque coefficient predicted by the unsteady BEM/RANS scheme.
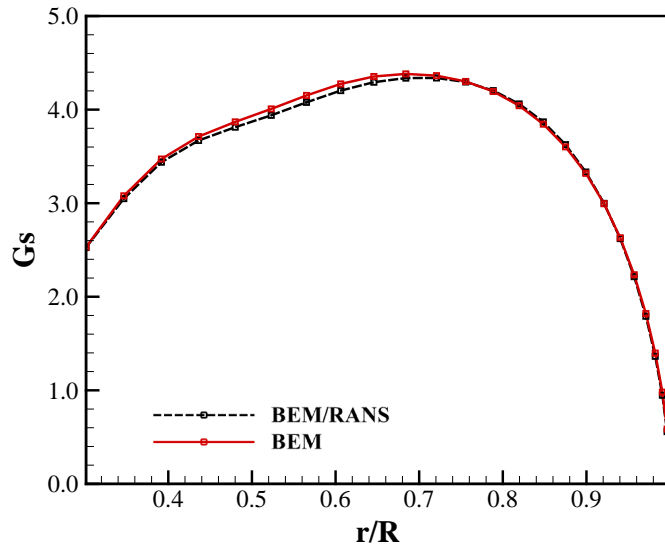
Figure 4.28: Blade circulation distribution predicted by the unsteady BEM/RANS scheme (after fully stabilized) and by the BEM solver under the nominal wake (uniform inflow).
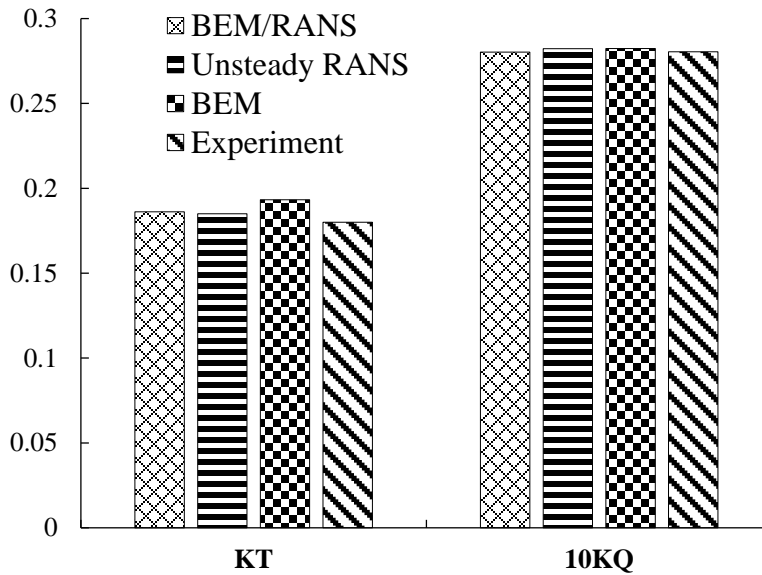
Figure 4.29: Comparison of the thrust coefficient and torque coefficient predicted by unsteady BEM/RANS scheme, by unsteady full-blown RANS, by BEM with the nominal wake, and by experiment.

(blade angle: 0-deg)
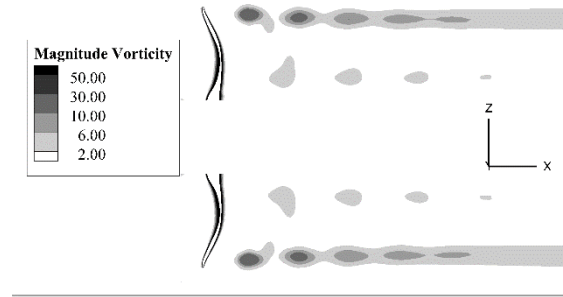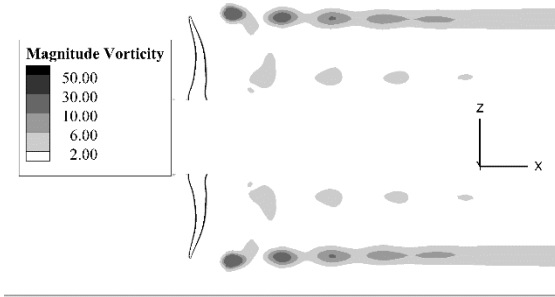
(blade angle: 15-deg)

(blade angle: 30-deg)
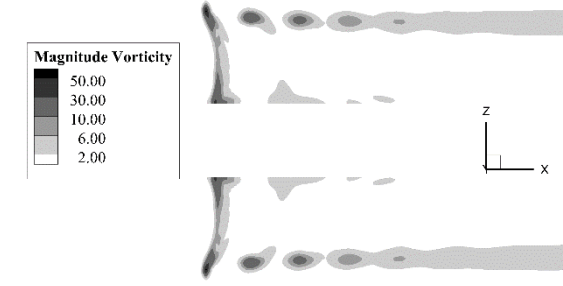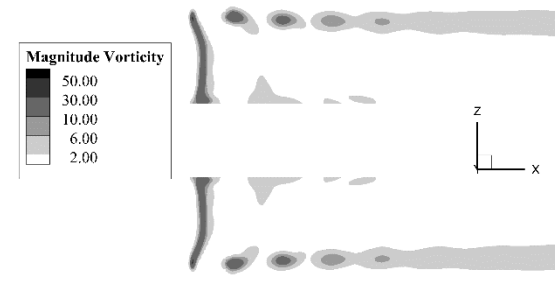
(blade angle: 45-deg)

(blade angle: 60-deg)   (blade angle: 75-deg)
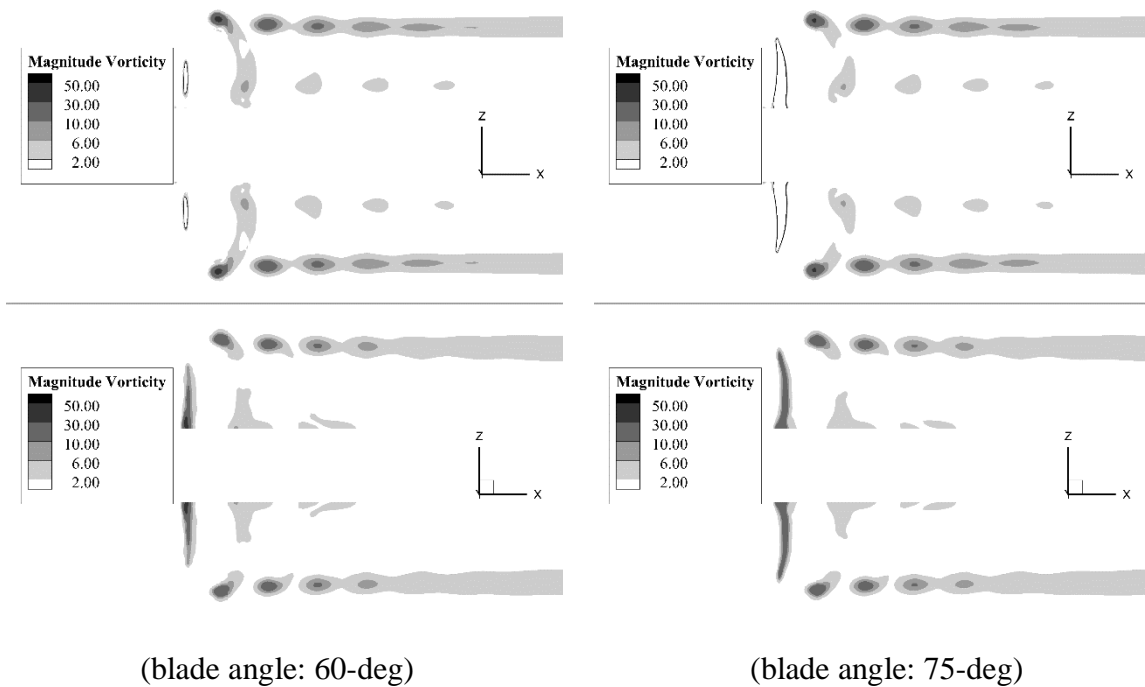
Figure 4.30: Comparison of vorticity fields from unsteady BEM/RANS scheme and from unsteady full-blown RANS. Six pairs of figures are shown, each representing a different blade angle (time). Within each pair, the top figure shows the vorticity field generated by non-slip wall boundaries while the lower figure shows the vorticity field generated by body force fields and mass source fields.

4.5 PROPELLER P2772 IN UNIFORM INCLINED INFLOW SOLVED BY UNSTEADY BEM/RANS

4.5.1 Description of the problem

In the previous study, a uniform incoming flow in the shaft axis direction is used. As a result, the propeller performance does not change with the blade angle. In order to further test the unsteady BEM/RANS scheme, it is helpful to include some non-axisymmetric component.

One possible way is to change the inflow direction so that the inflow is at an angle with the hub axis. Due to the relative direction between the inflow and the propeller blade angle, the incident flow velocity and direction for a blade can change. Therefore, the unsteady component is included in the propeller performance.

In real applications, some propellers are installed at an inclination angle from the ship longitudinal direction. Such cases can be solved as normally-placed propeller with an inclined inflow direction.

In this study, the P2772 propeller is used with a 10-degree inclination angle and the advance ratio $J_S = 0.6$.

4.5.2 Description of the numerical model

The unsteady BEM/RANS scheme is first used to solve this problem. To validate the unsteady BEM/RANS scheme, an unsteady full-blown RANS simulation is also performed. The BEM model, the unsteady RANS model, and the unsteady full-blown RANS model are the same as those described in Chapter 4.4.2. The only difference is that the inflow direction is changed in both RANS models, as shown in Figure 4.31.
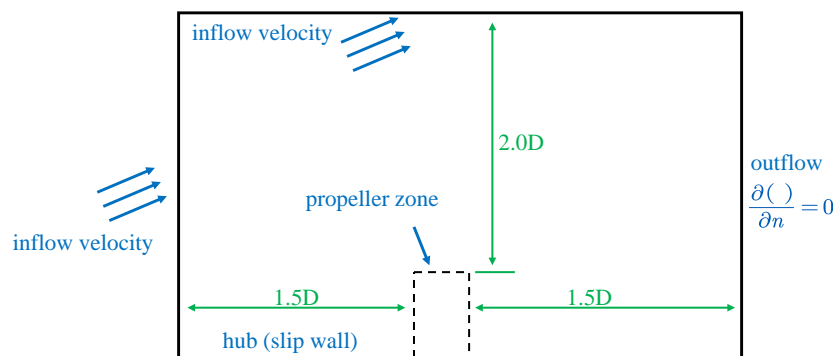
Figure 4.31: Boundary conditions and the range of computational domain of the unsteady RANS model with inclined inflow. Only the {z = 0 and y > 0} slice of the 3-dimensional model is shown.

Both BEM/RANS and full-blown RANS are solved for 6 propeller revolutions. A 3-degree equivalent time step size is used is BEM/RANS while 1-degree equivalent time step size is used in full-blown RANS. At the last revolution of BEM/RANS, the boundary layer correction is included in the BEM solver. However, the blowing source term is not applied to the RANS model.

4.5.3 Convergence study on mesh density and time step size

The first convergence study is on the number of panels used in the BEM model while the RANS model is kept unchanged, shown as case A, B, and C in Table 4.4.

The second convergence study is on the number of RANS cells in the inner zone and the time step size, show as case D, E, B, and F in Table 4.4.

	BEM panels on the key blade	Inner zone cells in RANS	Outer zone cells in RANS	Equivalent time step size (degree)
Case A	80×30	32×44×120	1.99 million	3
Case B	60×25	32×44×120	1.99 million	3
Case C	50×20	32×44×120	1.99 million	3
Case D	60×25	70×64×360	1.99 million	1
Case E	60×25	40×54×180	1.99 million	2
Case F	60×25	20×34×60	1.99 million	6

Table 4.4: Number of BEM panels and RANS inner zone cells used in the convergence study. The number of the BEM panels on the blade is given by the product of chord-wise panel count and span-wise panel count. The number of inner zone RANS cells is given by the product of chord-wise cell count, span-wise cell count, and circumferential cell count. The equivalent time step size is the propeller's rotation angle within a time step.
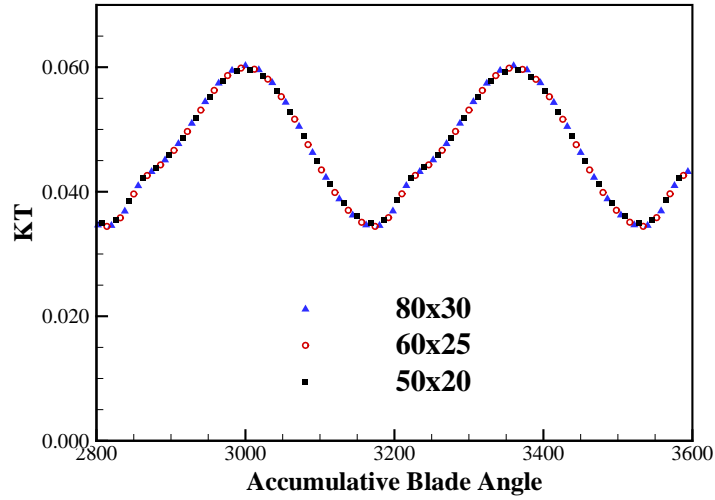
Figure 4.32: Comparison of the predicted thrust coefficients with a different number of panels on the BEM propeller surface: case A (80×30), case B (60×25), and case C (50×20). The accumulative blade angle is the angle the propeller has rotated since the start of the simulation.
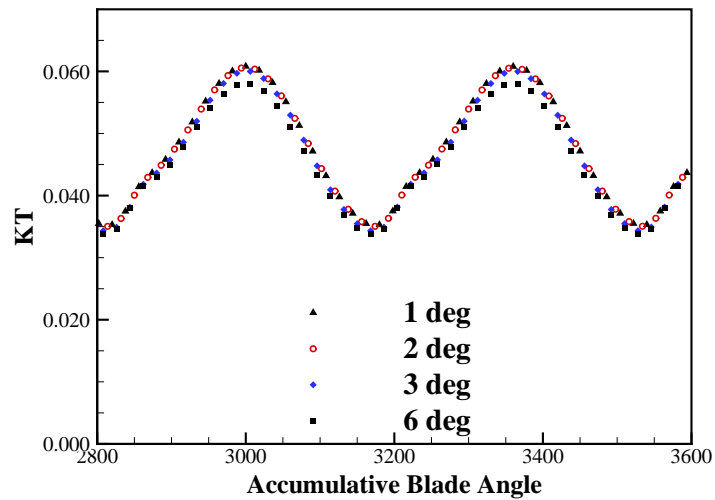
Figure 4.33: Comparison of the predicted thrust coefficients with a different number of inner zone RANS cells and different equivalent time step size: case D (70×64×360, 1deg), case E (40×54×180, 2deg), case B (32×44×120, 3deg), and case F (20×34×60, 6deg). The accumulative blade angle is the angle the propeller has rotated since the start of the simulation.

90

Results of both convergence studies are shown in Figure 4.32 and Figure 4.33. A good convergence is found on the number of BEM panels under current settings. The convergence with respect to the RANS inner zone mesh density and time step size is also good except case F.

In all the following unsteady BEM/RANS scheme, 60×25 panels are used on a propeller blade surface, 32×44×120 cells are used in the body force/mass source zone, and a 3-degree equivalent time step size is used.

4.5.4 Result and comparison

Figure 4.34 shows the predicted propeller forces as a function of time. Since the incident flow direction changes as the propeller rotate inside the inclined inflow, the stabilized propeller forces oscillate in a periodical manner. The mean propeller forces at the last propeller revolution are also compared, as shown in Figure 4.36.

In this application, although non-axisymmetric component is included in the problem, the inflow remains irrotational. Therefore, the effective wake is expected to be the same as the uniform inclined incoming flow. Figure 4.35 shows the predicted effective wake on the mid-chord slice. The error of the axial effective wake velocity is within 3% on most part of the mid-chord slice. The error is larger near the hub due to the saw-tooth effect. The vertical component of the effective wake is shown by arrows.

Figure 4.37 shows the pressure coefficient on the blade surface at 0-blade-angle of the last revolution. The pressure coefficients are plotted along the chord-wise direction at several different blade sections (r/R equals to 0.44, 0.57, and 0.79). Comparisons are made between results from the unsteady BEM/RANS with the boundary layer correction, from the unsteady BEM/RANS without the boundary layer correction, and from the unsteady

full-blown RANS. The boundary layer correction scheme used in this case is developed by Sun and Kinnas (Kinnas et al. 2007b). The scheme uses three-dimensional influence coefficients and considers the interaction among strips and the influence from other blades. If the result from the full-blown RANS is set as a reference, it can be clearly seen that the boundary layer correction significantly improves the results of the unsteady BEM/RANS scheme, especially at a lower radius, at the suction side, and near the trailing edge. This huge difference is due to the low advance ratio (0.6) used in this study. A lower advance ratio means a higher angle of attack for all the blade sections and, therefore, a larger boundary layer thickness at the suction side of the blade. Since the blade thickness at a lower radius is higher, the negative pressure gradients at these sections are more significant near the trailing edge. This makes the boundary layer effect more significant at the suction side, at a lower radius, and near the trailing edge.

Figure 4.38 compares the vorticity fields from the unsteady BEM/RANS scheme and from the unsteady full-blown RANS. Six pairs of figures are shown, each representing a different blade angle (time). Within each pair, the top figure shows the vorticity field generated by non-slip wall boundaries (full-blown RANS) while the lower figure shows the vorticity field generated by body force fields and mass source fields (BEM/RANS).
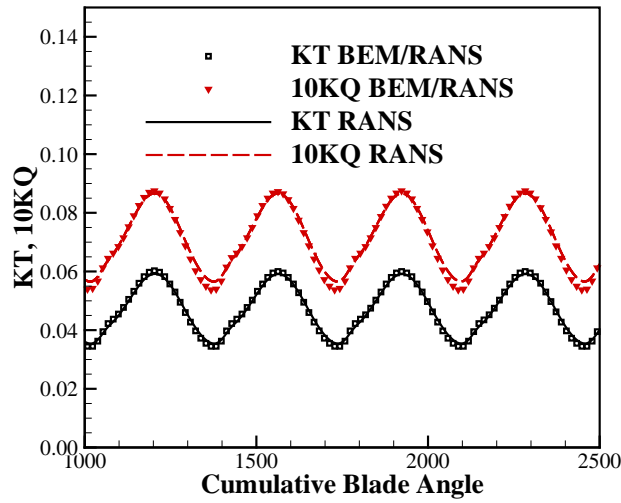
Figure 4.34: The stabilized thrust coefficient and torque coefficient predicted by the unsteady BEM/RANS scheme and by the unsteady full-blown RANS.
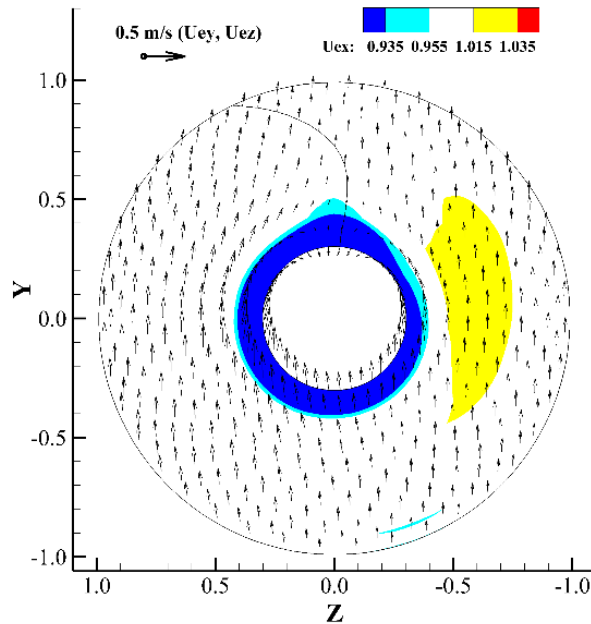
Figure 4.35: The mid-chord effective wake field q_e/V_S predicted by the unsteady BEM/RANS scheme. The axial velocity component is shown by the contour plot while the in-plane velocity components are shown by arrows.

93
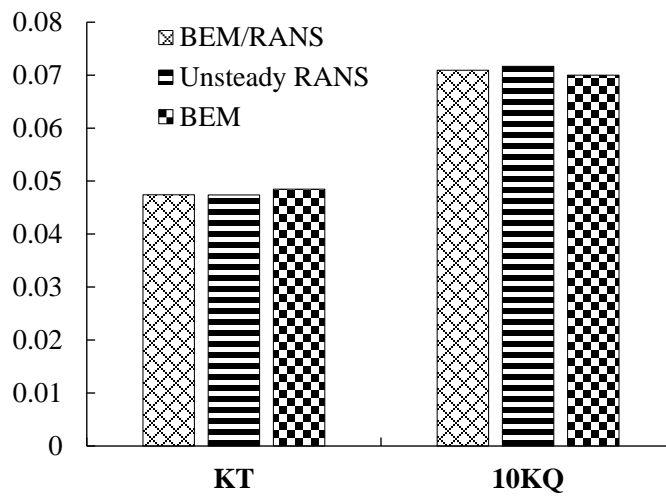
Figure 4.36: Mean thrust coefficient and torque coefficient at the last revolution. Comparison between unsteady BEM/RANS scheme, unsteady full-blown RANS, and BEM with nominal wake are provided.

(r/R = 0.44)

(r/R = 0.57)

(r/R = 0.79)
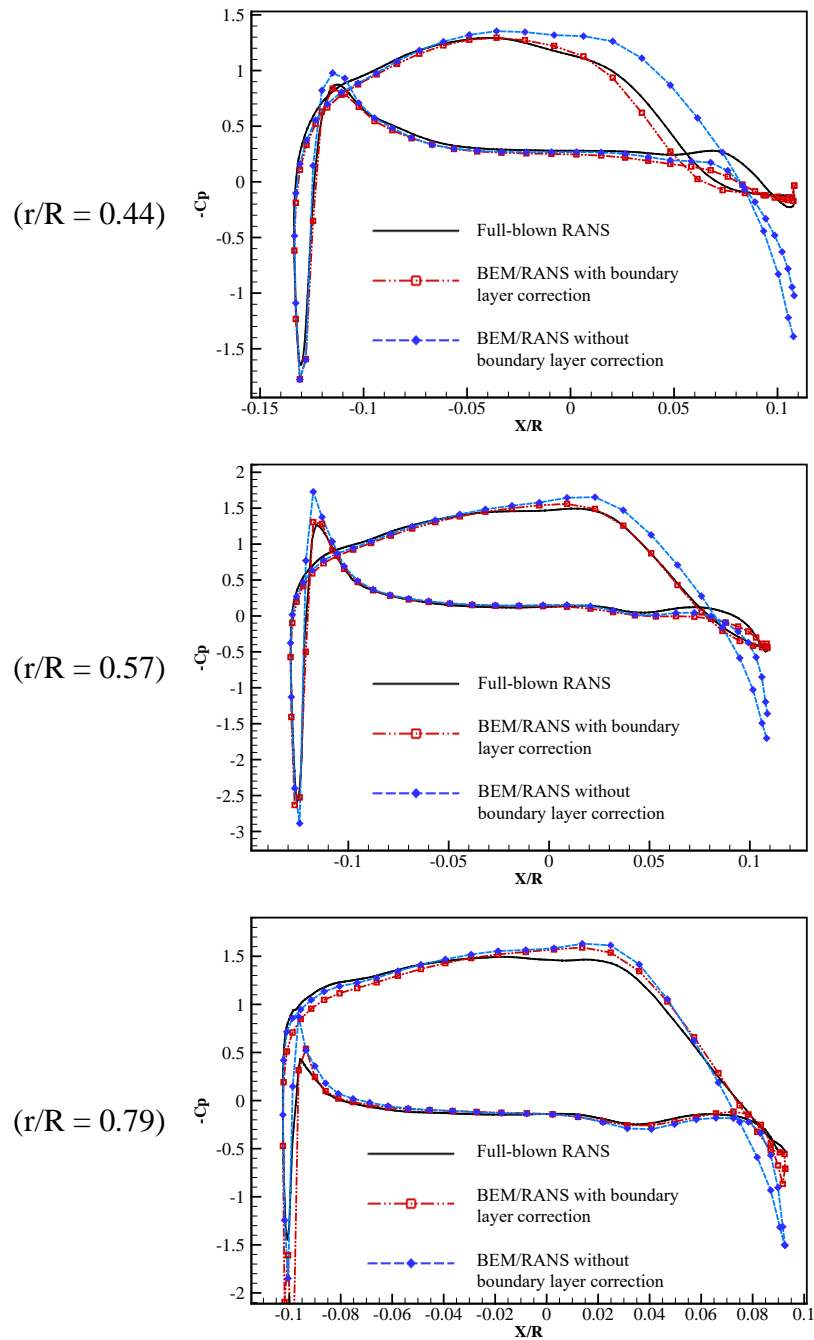
Figure 4.37: Key-blade surface pressure at zero-blade-angle of the last revolution. Comparison between unsteady BEM/RANS with boundary layer correction, unsteady BEM/RANS without boundary layer correction, and unsteady full-blown RANS are provided.

(blade angle: 0-deg)
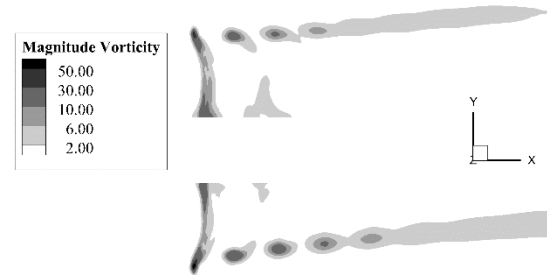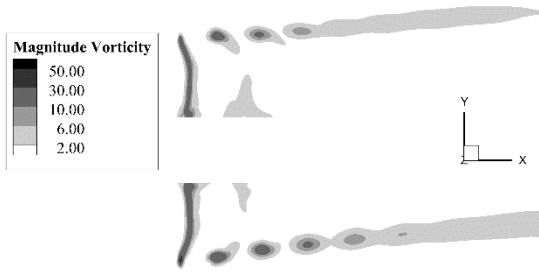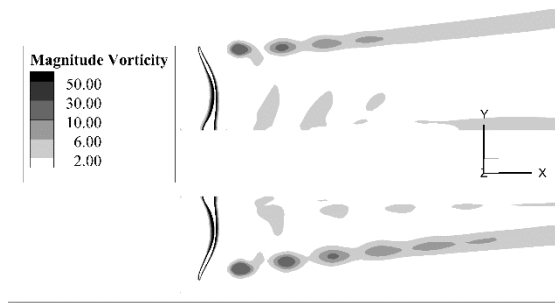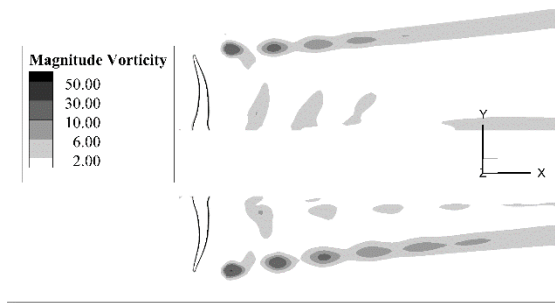
(blade angle: 15-deg)

(blade angle: 30-deg)
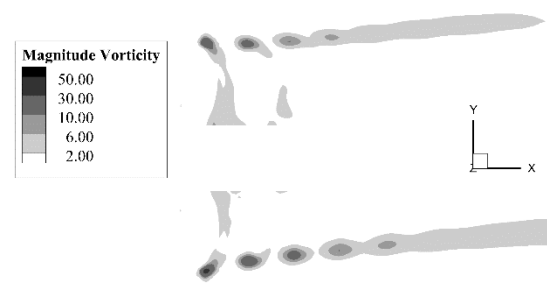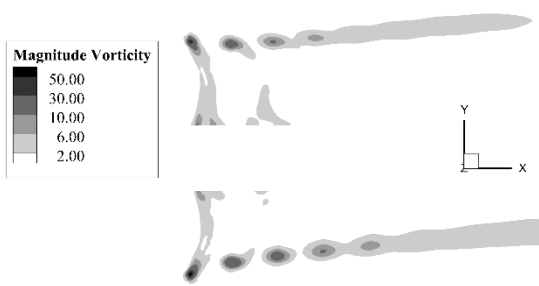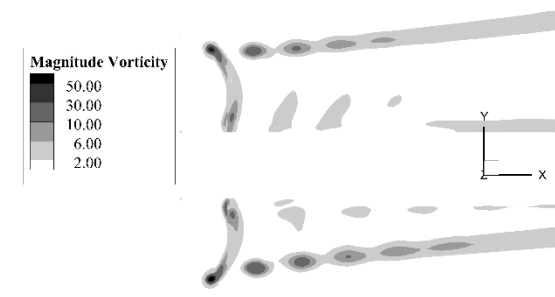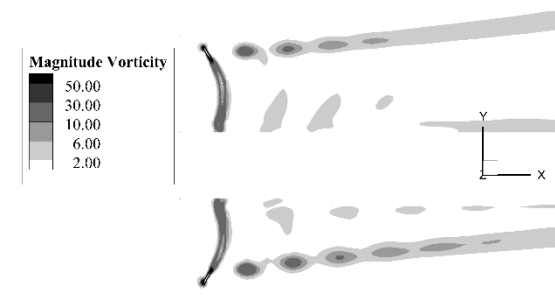
(blade angle: 45-deg)

(blade angle: 60-deg)   (blade angle: 75-deg)
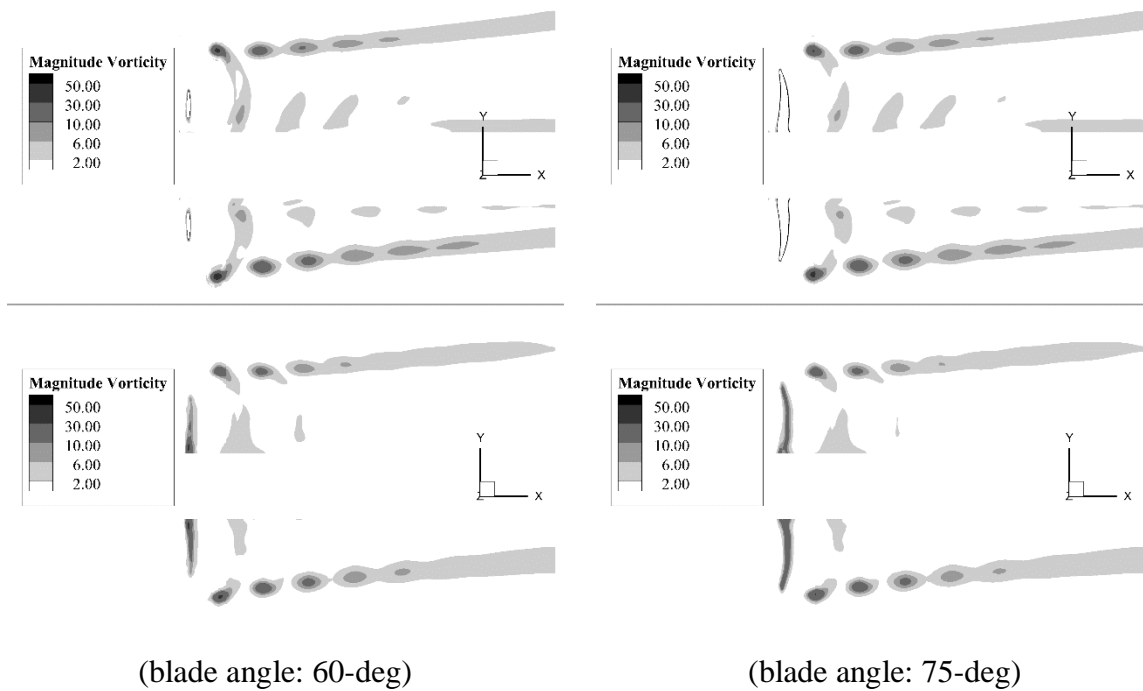
Figure 4.38: Comparison of vorticity fields from unsteady BEM/RANS scheme and from unsteady full-blown RANS (inclined inflow case). Six pairs of figures are shown, each representing a different blade angle (time). Within each pair, the top figure shows the vorticity field generated by non-slip wall boundaries while the lower figure shows the vorticity field generated by body force fields and mass source fields.

Chapter 5.   Multibody Interaction Applications

In the previous chapter, the BEM/RANS schemes are used to predict the propeller performance under a uniform or non-uniform inflow. Several numerical studies are performed to improve the scheme.

In this chapter, the more practical and more challenging problems are looked at. The BEM/RANS scheme is applied to multibody interaction problems. In the first part, the axisymmetric and non-axisymmetric BEM/RANS scheme is used to solve the interaction between the forward propeller and the aft propeller in a contra-rotating propeller (CRP) unit. In the second part, a hull-propeller-rudder interaction problem is handled by the non-axisymmetric BEM/RANS. In the last part, the unsteady BEM/RANS scheme is used to solve the hull-propeller-rudder interaction at ship maneuvering conditions.

5.1 CONTRA-ROTATING PROPELLER SOLVED BY AXISYMMETRIC BEM/RANS AND NON-AXISYMMETRIC BEM/RANS

5.1.1 Description of the problem

A contra-rotating propeller, also referred to as CRP, is a propulsion unit which includes two coaxial single propellers operating in opposite directions. The use of CRPs in marine propulsion improves the fuel efficiency and also helps underwater vehicles to maintain torque balance.

As shown in Figure 5.1, the podded CRP unit includes a 3-blade forward propeller, a 4-blade aft propeller, a shaft, and a strut. The interaction between the forward propeller, the aft propeller, and the strut (only in the non-axisymmetric version) can be handled by

---

the BEM/RANS scheme.

In this study, the CRP performance is predicted under two conditions. Under the first condition, the inflow is uniform and the inflow velocity is in the direction of the shaft axis. This case is solved by both the axisymmetric version and the non-axisymmetric version of the BEM/RANS approach. Under the second condition, the CRP performance under a steering condition is simulated. In other words, the incoming flow is inclined inside the horizontal surface. This situation is handled by the non-axisymmetric approach.

Figure 5.1: Geometry of the contra-rotating propeller unit.

5.1.2 Description of the numerical model

The first numerical model used the axisymmetric BEM/RANS to handle the straight inflow situation. Since this model solves for the axisymmetric problem, the effect from the strut has to be neglected. The steady axisymmetric RANS model is coupled with two separate steady BEM models. The first BEM model solves the forward propeller performance while the second BEM model solves the aft propeller performance. The interaction between the two propellers is achieved through RANS. Figure 5.2 shows the BEM panel models for the forward propeller and the aft propeller. In both BEM models, $80{\times}30$ panels are placed on the key blade surface while $70{\times}20$ panels are used for the shaft

99

surface between two blades. Figure 5.3 shows the mesh of the axisymmetric RANS model. The mesh model includes 19,900 quadrilateral cells which cover a computational domain from -2.0D to 3.5D in the axial direction and up to 2.5D in the radial direction. The inflow velocity is set at the upstream boundary; a slip-wall condition is set on the shaft surface; a zero-gradient condition is used for all the flow variables at the downstream boundary. Other settings for the axisymmetric RANS model are listed in Appendix C.
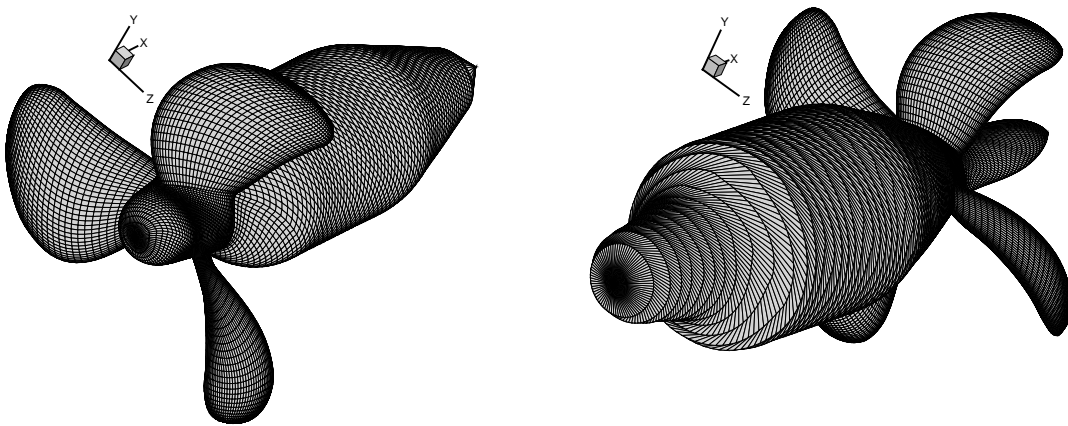
Figure 5.2: BEM panel models for the forward propeller (left) and aft propeller (right).
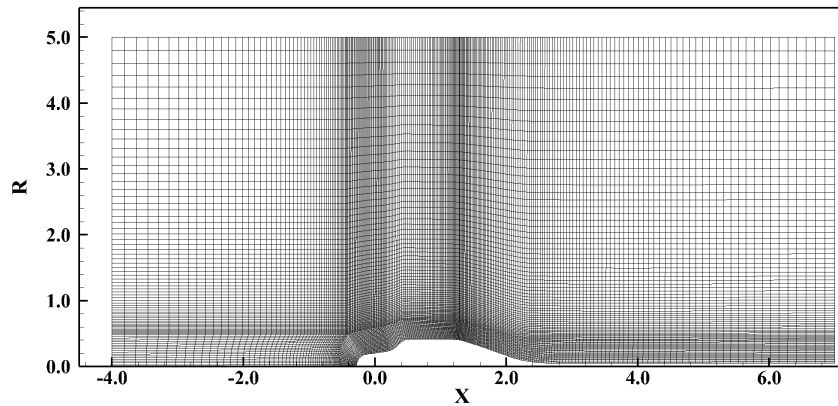
Figure 5.3: The finite volume mesh used in the axisymmetric BEM/RANS scheme (CRP application).

100

The second numerical model used the non-axisymmetric BEM/RANS to handle the straight inflow situation. In this model, the effect from non-axisymmetric bodies, the strut, can be included. The steady 3-dimensional RANS model is coupled with two separate unsteady BEM models. The same BEM panel models are used, as shown in Figure 4.1. However, the BEM solver behaves differently in this case. In the axisymmetric approach, BEM only solves for the mean propeller performance. In the non-axisymmetric approach, BEM solves for the propeller performance as a function of the blade angle. As shown in Figure 5.4, the non-axisymmetric RANS model includes 2.2 million hexahedron and tetrahedron cells which cover a computational domain from -2.5D to 5.0D in the axial direction, from -3.0D to 3.0D in the horizontal direction, and from -3.0D up to the free surface in the vertical direction. The inflow velocity is set at the upstream boundaries. The shaft surface is represented by a slip-surface while the non-slip boundary condition is applied to the strut, as shown in Figure 5.5. A zero-gradient condition is used for all the flow variables at the downstream boundary. Other settings for the axisymmetric RANS model are listed in Appendix C.
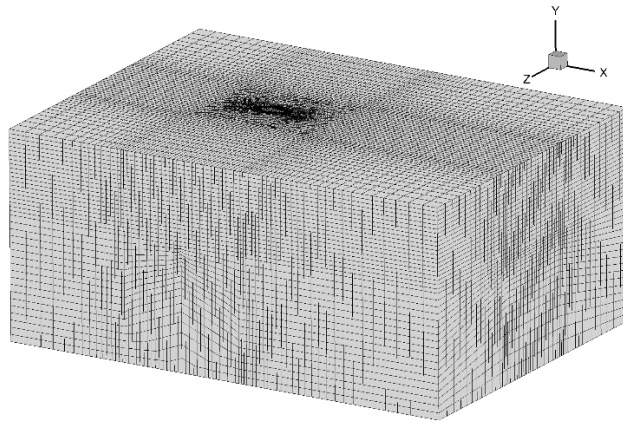
Figure 5.4: The finite volume mesh used in the non-axisymmetric BEM/RANS scheme (CRP application).
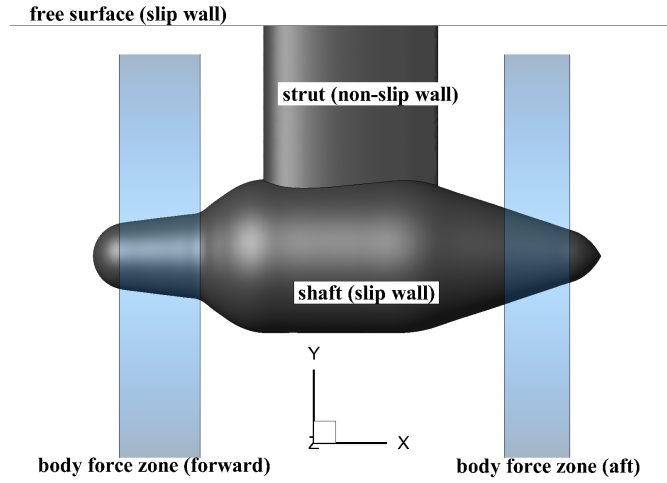
Figure 5.5: Boundaries conditions of the RANS model in the non-axisymmetric
BEM/RANS scheme (CRP application).

The third numerical model used the non-axisymmetric BEM/RANS to handle the
inclined inflow situation. Both the BEM model and the RANS model is mostly the same
as those in the second case. The only difference is that the inflow direction at upstream
boundaries is changed.

Since the BEM solver is nondimensionalized by the propeller's maximum radius
and the RANS solver is nondimensionalized by the forward propeller's maximum radius,
the aft propeller's body force field and mass source field need to be scaled before they are
used in RANS. First, the size ratio m is defined $m = D_F/D_A$ where D_F and D_A are the
propeller diameters for the forward propeller and the aft propeller respectively. According
to the Buckingham-π theorem, the aft propeller's body force field and mass source field
can be scaled by the following equations:

$$\mathcal{F}_{\text{RANS.aft}} = m\mathcal{F}_{\text{BEM.aft}}$$

(5.1)

$$\mathcal{Q}_{\text{RANS.aft}} = m\mathcal{Q}_{\text{BEM.aft}}$$

(5.2)

102

5.1.3 Mesh convergence study

A convergence study is first made to test whether the propeller performance is sensitive to the number of panels in the BEM model and the number of the cells in the RANS model. As shown in Table 5.1, the non-axisymmetric version of the BEM/RANS scheme is tested in two cases. Case B is the normal setting and has a higher number of panels/cells compared to case A. The predicted circulation distributions from case A and from case B are compared, as shown in Figure 5.6. The thrust coefficients predicted by case A and case B are 0.388 and 0.386 respectively, with a 0.37% difference between them.

	BEM panels (fwd)	BEM panels (aft)	RANS cells
Case A	60×20	60×20	1.6 million
Case B	80×30	80×30	2.2 million

Table 5.1: Number of BEM panels and RANS cells used in the convergence study.

(forward propeller)   (aft propeller)
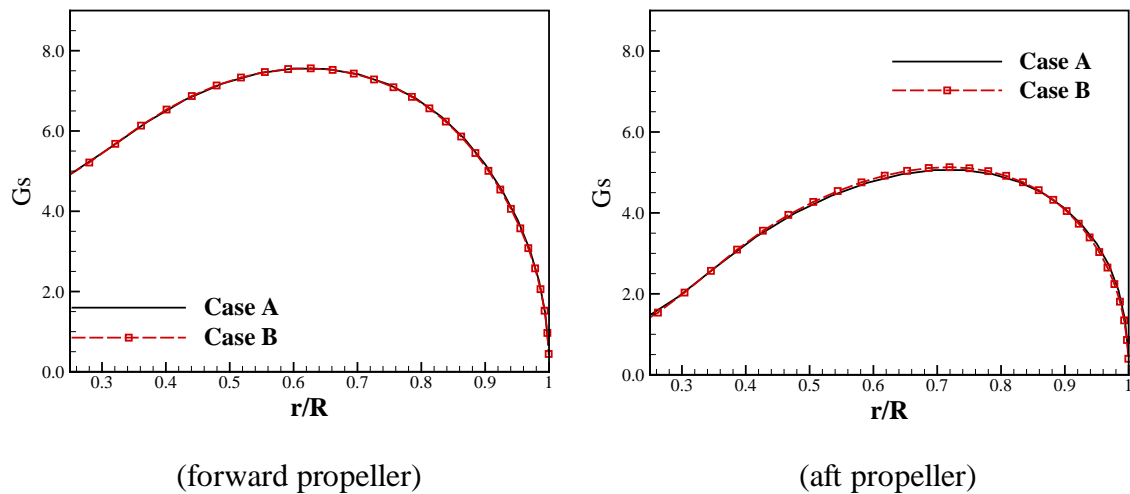
Figure 5.6: Comparison of the circulation distribution from case A and case B.

5.1.4 Results of the straight inflow case

If we only care about the CRP's mean performance, the non-axisymmetric component of the flow can be neglected and the axisymmetric version of the BEM/RANS scheme can be used. However, it is very important to know how much numerical error is introduced in neglecting the non-axisymmetric flow component.

Before making further statements, it is helpful to think about what assumptions are made in reducing the non-axisymmetric problem to the axisymmetric problem. First, the non-axisymmetric bodies, meaning the strut and the free surface in this case, are neglected. Then, the three-dimensional RANS equations are integrated along the circumferential direction. If we assume the total flow does not change much in the circumferential direction, the crossing terms, which are created in the integration of the convective terms, can be neglected. Then, the 3D RANS equation can be written into its axisymmetric form (Su and Kinnas 2017a, Su and Kinnas 2017b).

In Figure 5.7, the single-blade thrust coefficient and torque coefficient are shown as a function of the blade position angle. The 0-degree corresponds to the blade location when it passes the strut. In the non-axisymmetric case, at around the 0-blade-angle, where the blades are closest to the strut, both thrust and torque from the forward blade increase while both thrust and torque from the aft blade decrease. In the axisymmetric case, thrust and torque do not change with the blade position angle. More importantly, both thrust and torque in the axisymmetric case are very close to the thrust and torque in the non-axisymmetric case except when they are close to the 0-blade-angle. Therefore, it is fair to say that the difference between the axisymmetric BEM/RANS and the non-axisymmetric version mainly comes from the non-axisymmetric bodies. Neglection of the crossing terms does not make much difference and can be seen as a reasonable assumption.

104

(forward propeller)   (aft propeller)
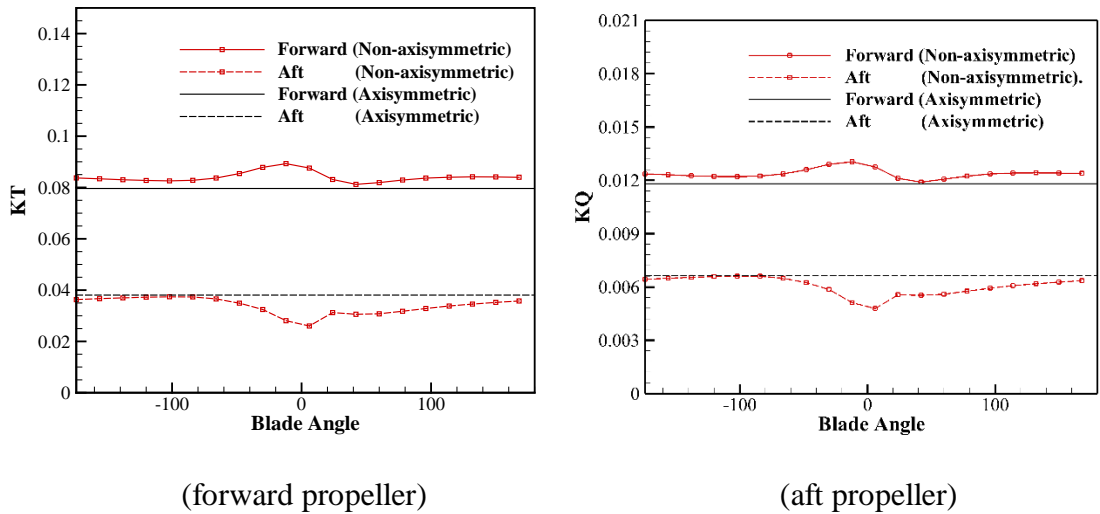
Figure 5.7: Unsteady thrust coefficients (single blade) and torque coefficients (single blade) predicted by the axisymmetric BEM/RANS scheme and by the non-axisymmetric BEM/RANS scheme.
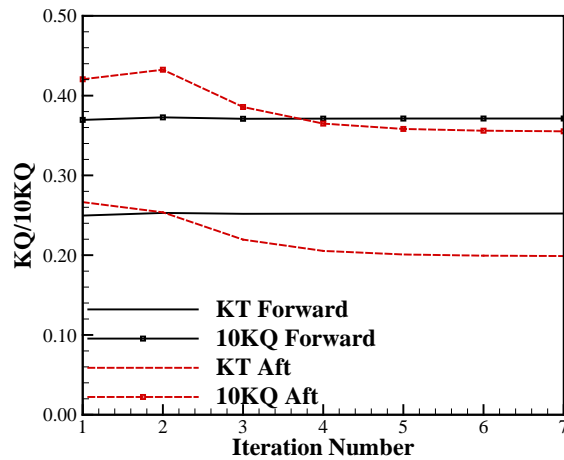
Figure 5.8: Convergence history of the propeller forces on both the forward propeller and the aft propeller.

Figure 5.8 shows the convergence history of the thrust the torque on both the forward propeller and the aft propeller. According to the figure, the forces on the forward propeller does not change much with the iterations because the influence from downstream bodies to upstream bodies is not significant. The forces on the aft propeller, however,

decreases significantly with the iteration and finally converged at around the 5th iteration. This significant change is caused by the wake flow of the forward propeller and the wake flow of the strut.

(forward propeller)   (aft propeller)

(total = forward + aft + strut + pod)
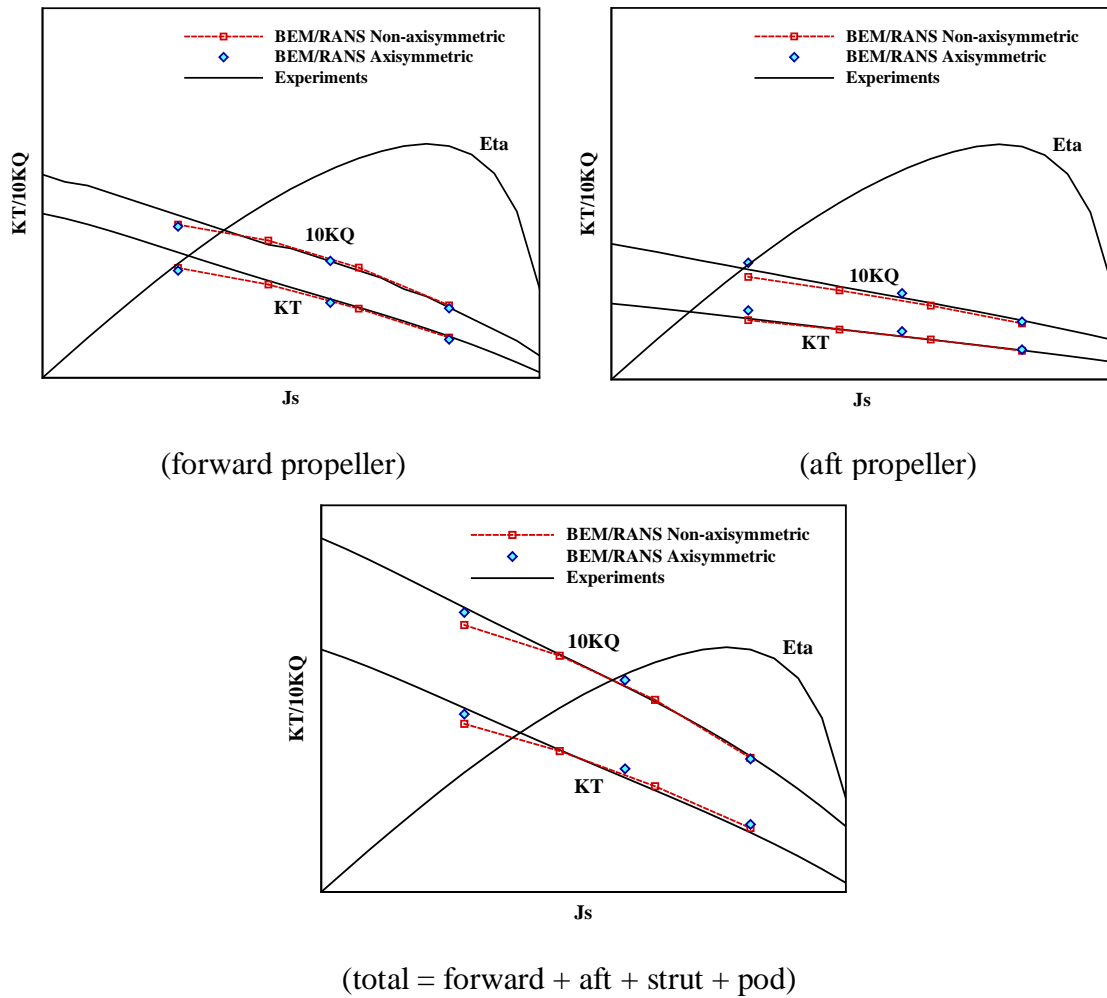
Figure 5.9: Comparison of the predicted thrust coefficients and torque coefficients with experimental data (all figures are plotted with the same scale). The total force includes the force of the forward propeller, the aft propeller, the strut, and the pod.

106

In Figure 5.9, the thrust coefficients and torque coefficients are compared with experimental data at different advance ratios. These coefficients are given by individual propeller values as well as the total CRP values. The total thrust includes not only thrust on both propellers but also the drag forces on the pod and on the strut. As the figure shows, results from both the axisymmetric scheme and the non-axisymmetric scheme have a good agreement with the experimental data. Similar to what has been discovered before, neglecting the strut and the free surface leads to a lower forward propeller loading and a higher aft propeller loading. It is worth noting that the experimental error is unavoidable and should also be accounted for in the comparison between the predicted value and the experiment value.

At lower advance ratios, the error becomes noticeable. A possible explanation can be made by looking at the assumptions of the BEM/RANS interactive scheme. If we start from the more general unsteady RANS equation and integrate them with respect to time over a blade-passing period, the steady RANS equation can be obtained with several additional crossing terms originated from the convective term. If a small amplitude assumption is made on the unsteady component of the total flow, the crossing term can be neglected. It is important to mention that the propeller perturbation flow field, which rotates with the propeller, is the major source of the unsteady flow component. At normal advance ratios, the small amplitude assumption is reasonable.

However, as the advance ratio becomes very low and the propeller loading gets enough high, the stronger propeller perturbation flow leads to a more significant unsteady component. In this case, the small amplitude assumption may no longer be valid and, therefore, the error may increase.
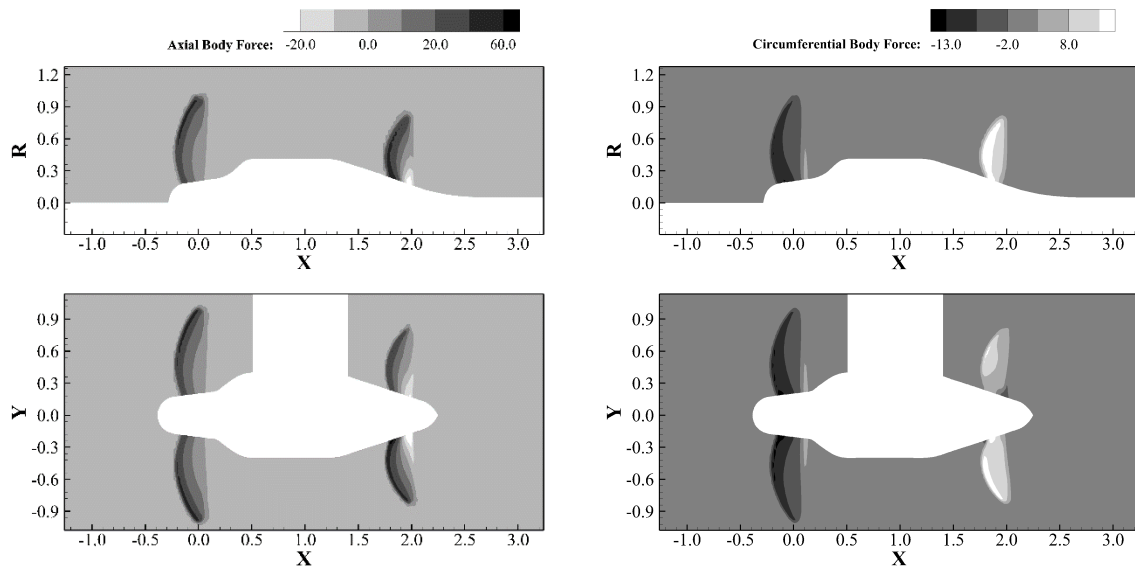
(axial component of body force field)   (circumferential component of body force field)
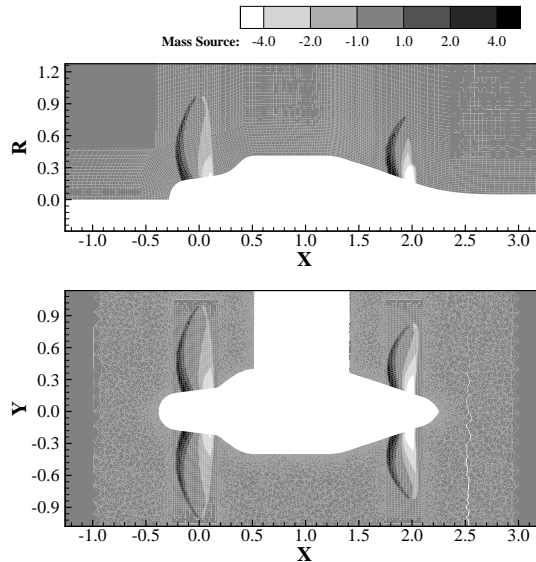
(mass source field)

Figure 5.10: Body force distribution and mass source distribution from axisymmetric BEM/RANS approach (plotted at θ=0 slice, upper figure of every pair) and from non-axisymmetric BEM/RANS approach (plotted at z = 0, lower figure of every pair). The body force field is nondimensionalized by $\left(2\rho V_S^2/D_F\right)$ and the mass source is nondimensionalized by $\left(2\rho V_S/D_F\right)$.

For the total forces in low advance ratios, the axisymmetric scheme has a relatively smaller error compared to the non-axisymmetric scheme. This cannot be interpreted as axisymmetric behaves better because the lower error comes from the cancellation between an underpredicted forward propeller force and an overpredicted aft propeller force. The overpredicted aft propeller loading, as we discussed before, is due to the lack of the strut effect.

Figure 5.10 shows the axial body force field, the circumferential body force field, and the mass source field. Results from the axisymmetric BEM/RANS are the top figures and are plotted at the $\theta = 0$ slice. Results from the non-axisymmetric BEM/RANS are the lower figures and are plotted at the z = 0 slice. Both results show great similarities although a non-axisymmetric pattern can be observed in the aft propeller circumferential body force field.

As shown in Figure 5.10, the forward propeller and the aft propeller both generate a positive axial body force while the circumferential body forces they induced are in opposite directions. The mass source reflects the gradient of the blade thickness distribution in the flow direction. Therefore, it should be positive near the leading edge and negative near the trailing edge.

(axial velocity)   (swirl velocity)

Figure 5.11: The total flow field q_e/V_S from the axisymmetric BEM/RANS approach
(plotted at the $\theta = 0$ slice; upper figures) and from non-axisymmetric
BEM/RANS approach (plotted at the z = 0 slice, lower figures).

In Figure 5.11, the axial and swirl components of the total flow are plotted at the
ship center plane (z = 0 slice). The velocity fields are nondimensionalized by the ship
speed. As shown from the figure, the swirl component is induced by the forward propeller
and reduced by the aft propeller. A small leakage happens near the hub.

With a 2.7 GHz E5-2680 processor, the axisymmetric BEM/RANS scheme takes 1
hour to finish while the non-axisymmetric BEM/RANS scheme takes 5 hours to finish.

5.1.5 Results of the steering case

In a podded CRP application, it is useful to predict the CRP performance when at
a steering condition. To simplify this unsteady steering problem, an inclined-shaft case is
solved instead as a preliminary study.

Figure 5.12: Definitions of the angle of inclination and four different force components.

The definition of the angle of inclination and four different for components are shown in Figure 5.12. The predicted forces generated by the CRP at different inclination angles are shown in Figure 5.13. These forces are non-dimensionalized by the same way thrust coefficient is calculated. Force K_{HX} and K_{HS} are forces in the longitudinal direction and the horizontal direction of the ship hull coordinate system. Force K_{PX} and K_{PS} are forces in the axial direction and the horizontal direction of the propeller shaft coordinate system. Both horizontal forces define the positive direction as pointing from the port side to the starboard side.

As shown in Figure 5.13, when the inclination angle increases, force K_{HX} remains nearly unchanged while force K_{HS} grows linearly with the angle of inclination. In the propeller shaft coordinate system, the horizontal force K_{PS} is linear to the angle of inclination while the axial force K_{PX} remains nearly constant.
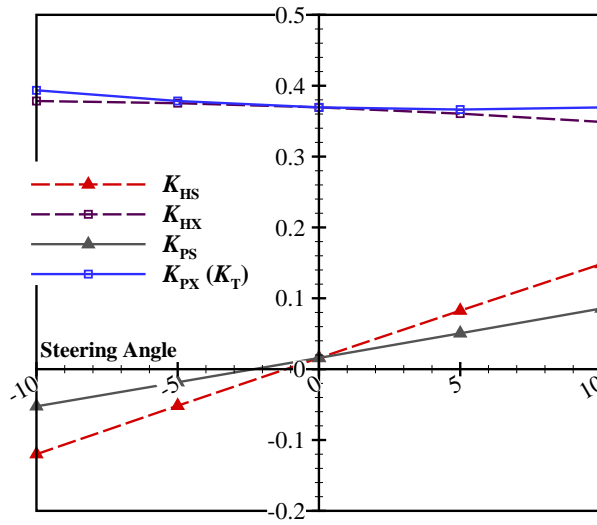
Figure 5.13: Propeller forces at different angles of inclination.

In Figure 5.14, the effective wake of the aft propeller is plotted on the mid-chord slice. The axial velocity fields are represented by the grayscale contours while the other effective wake velocity components are shown by arrows. As shown in the figures, the effective wake fields for the aft propeller has a strong axial component and a strong swirl component because of the forward propeller's wake flow. At ± 10 angle of inclination, part of the aft propeller falls outside of the forward propeller's trailing wake region. At those outside regions, both the axial component and the swirl component of the effective wake become weaker.
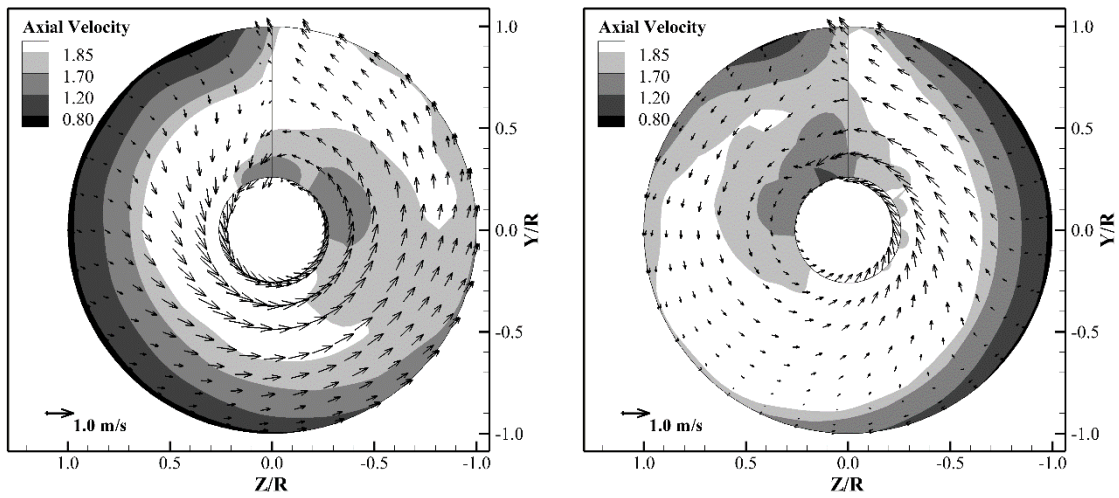
(-10 degrees angle of inclination)   (+10 degrees angle of inclination)
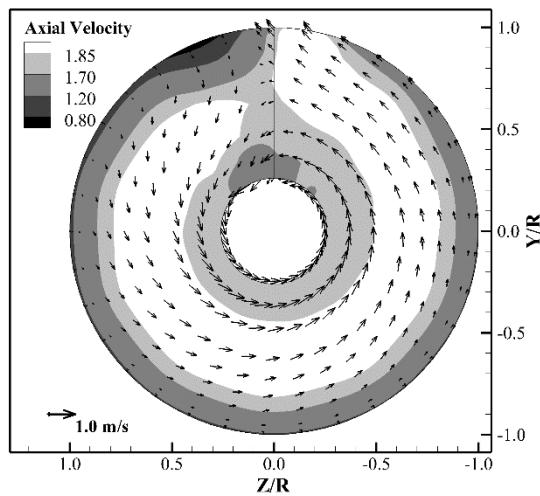
(+0 degrees angle of inclination)

Figure 5.14: Effective wake field at the mid-chord slice of the aft propeller at different angles of inclination. The velocity is nondimensionalized by the ship speed.

Based on the above results, the non-axisymmetric BEM/RANS scheme is capable of handling a CRP propeller working at an small inclination angle. Correlations with experiments are needed in the future when experimental data becomes available.

5.2 HULL-PROPELLER-RUDDER INTERACTION SOLVED BY NON-AXISYMMETRIC BEM/RANS

5.2.1 Description of the problem

In this application, the hull-propeller-rudder interaction problem is attempted via the non-axisymmetric BEM/RANS scheme.

The geometry of the hull and the rudder comes from the M/T Olympus tanker, as shown in Figure 5.15. The propeller used in this study is the P2772 propeller at P/D = 0.87, as shown in Figure 5.16. The thickness distribution the propeller blade is modified in order to convert the round trailing propeller to a sharp trailing edge propeller. More details can be found in Chapter 4.4.1.
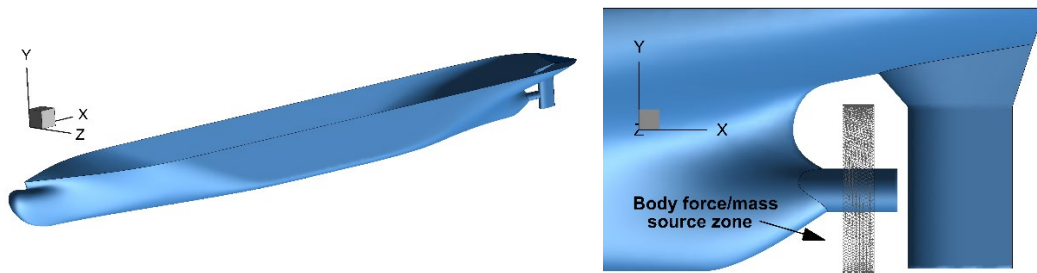
Figure 5.15: Ship hull and rudder geometry of the M/T Olympus tanker. An overview of this ship hull is given in the left figure. The ship stern geometry and rudder geometry are shown in the right figure.

114
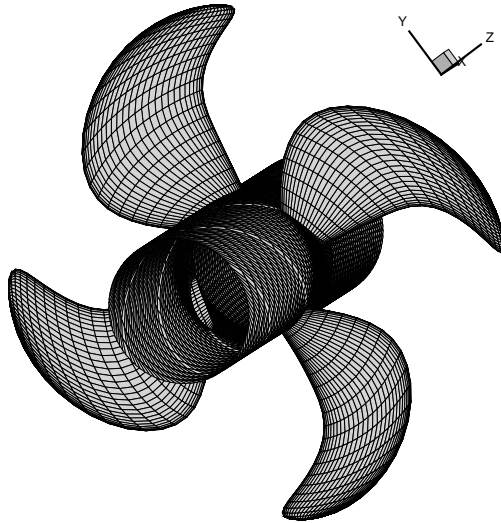
Figure 5.16: BEM model of the P2772 propeller geometry in the hull-propeller-rudder interaction case.

In this study, the ship speed remains constant and follows the ship hull longitudinal direction. The advance ratio ranges from 0.6 to 1.0.
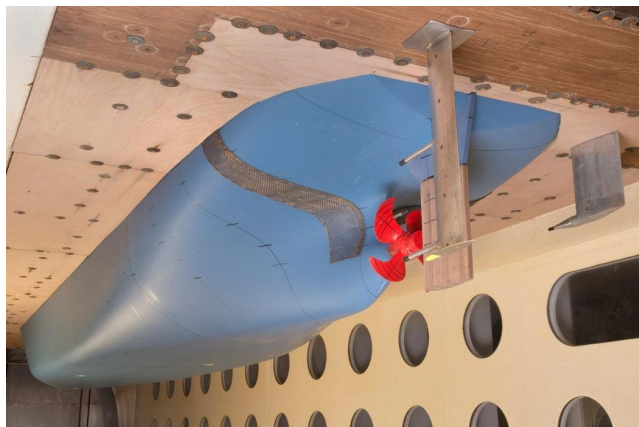
Figure 5.17: Photo of the model test facilities and configurations.

The numerical results are compared with the measurements from an experiment inside a closed rectangular water tunnel (Hallander et al. 2013, Tani et al. 2016). In this experiment, the hull model (including the rudder) was mounted at its design draft on the

top inside a cavitation tunnel as shown in Figure 5.17. The propeller was installed onto the model and powered by a motor to rotate at a given speed. The atmospheric pressure was used inside the tunnel so that the cavitation did not happen. The propeller thrust and torque were measured at different advance ratios. It is worth noting that the experiment used a left-handed propeller, which has been converted to its right-handed counterpart in the BEM model.

5.2.2 Description of the numerical model

Due to the non-axisymmetric shape of the ship hull and the rudder, this problem should be solved with the non-axisymmetric BEM/RANS approach.

In the BEM model, as shown in Figure 5.16, 80×20 panels are placed on the key blade surface while 70×20 panels are used for the hub surface between two blades. A PSF-2 type wake alignment scheme is used.

Since our goal is to establish a good correlation between the results from the BEM/RANS scheme and the experimental value, the computational domain of RANS is set to have the same cross-section dimensions as the water tunnel, as shown in Figure 5.18.
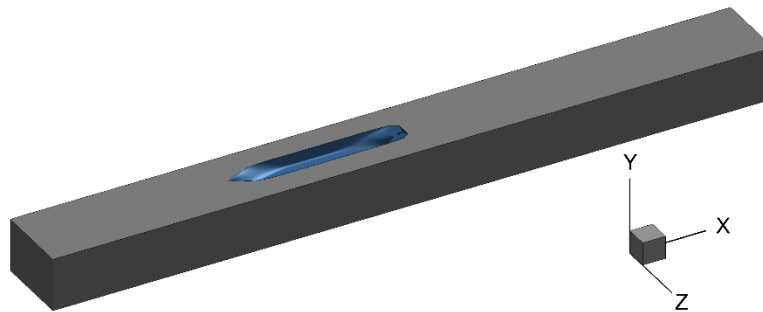
Figure 5.18: Computational domain of the RANS model in the hull-propeller-rudder interaction case (non-axisymmetric problem).

Four million cells are used in the RANS model. A non-slip boundary is applied to the ship hull surface and the rudder surface, while a slip-wall condition is used on the propeller shaft. The slip boundary condition helps to improve the numerical stability of the coupling scheme.

It takes 5 to 7 iterations for the scheme to converge and the typical time cost is around 2 hours with four Xeon E5-2680 processors.

5.2.3 Result and comparison
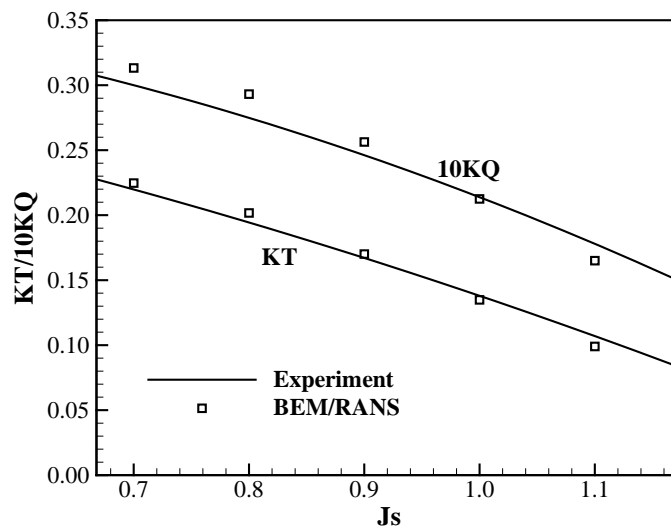
Figure 5.19: Propeller forces predicted by the non-axisymmetric BEM/RANS and those from the experimental measurements.

Five cases with different advance ratios, ranging from 0.7 to 1.1, are solved. Figure 5.19 shows the comparison of propeller thrust coefficient and torque coefficients predicted by the non-axisymmetric BEM/RANS scheme with those measured in the experiment. Figure 5.20 shows the time-averaged circulation distribution at different iteration steps for $Js = 0.9$ case. At the same advance ratio, the axial component of the total flow is plotted on

117

the ship centerline plane, as shown in Figure 5.21. The total forces on the key blade are shown in Figure 5.23 as a function of the blade angle. The first figure in Figure 5.22 shows the nominal wake field, which is obtained by solving RANS without including the body force term and the mass source term. Then, the effective wake fields on the mid-chord plane at different advance ratios are plotted.
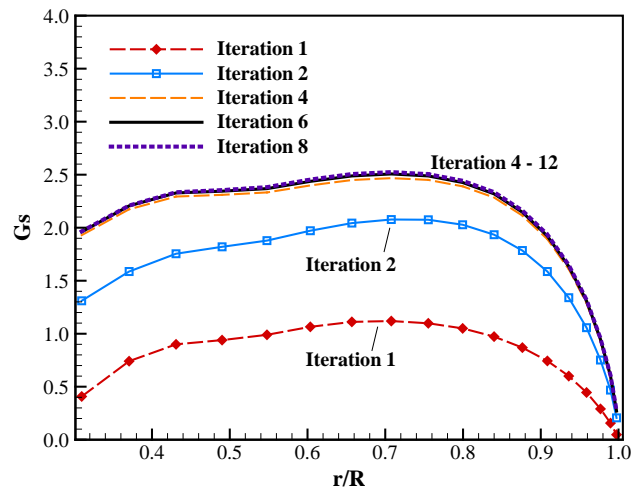
Figure 5.20: Circulation distribution (time-averaged, Js = 0.9) at different iteration steps of the non-axisymmetric BEM/RANS scheme. The 1st iteration corresponds to a uniform inflow case.
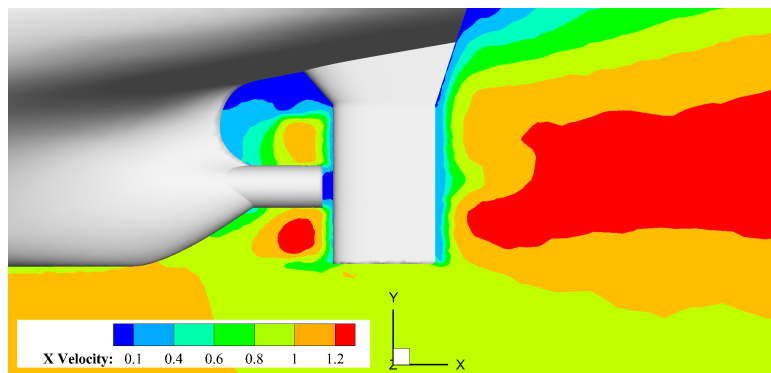
Figure 5.21: Axial component of the total flow field q_t/V_S plotted on the ship centerline plane (z = 0 slice).

118

(nominal wake field)

(effective wake field at $J_S = 0.6$)

(effective wake field at $J_S = 0.8$)

(effective wake field at $J_S = 1.0$)
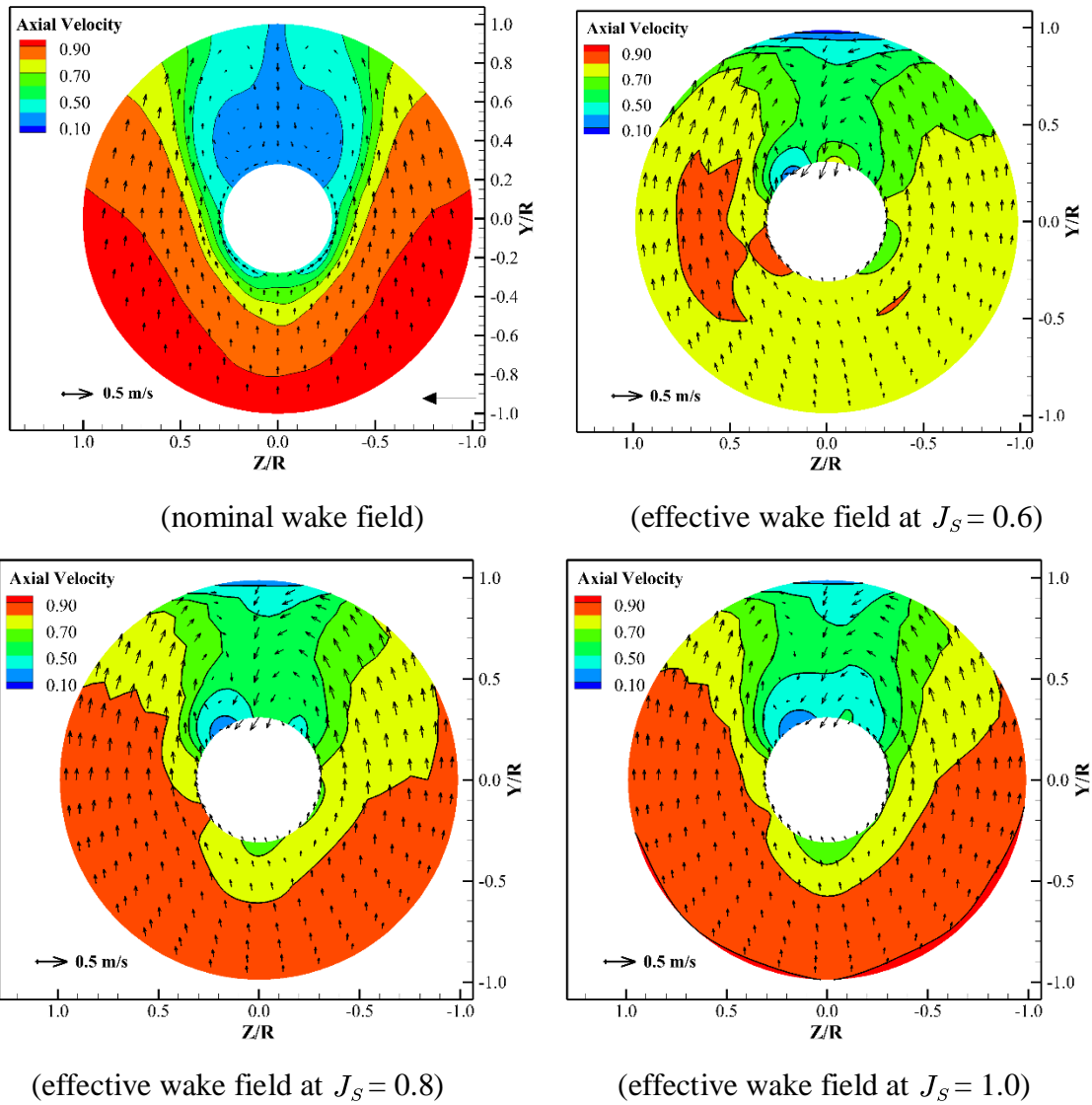
Figure 5.22: The nominal wake field and effective wake field plotted on the mid-chord slice of the body force zone. Axial velocity component is represented by the contour while the in-plane velocity components are represented by arrows.

119
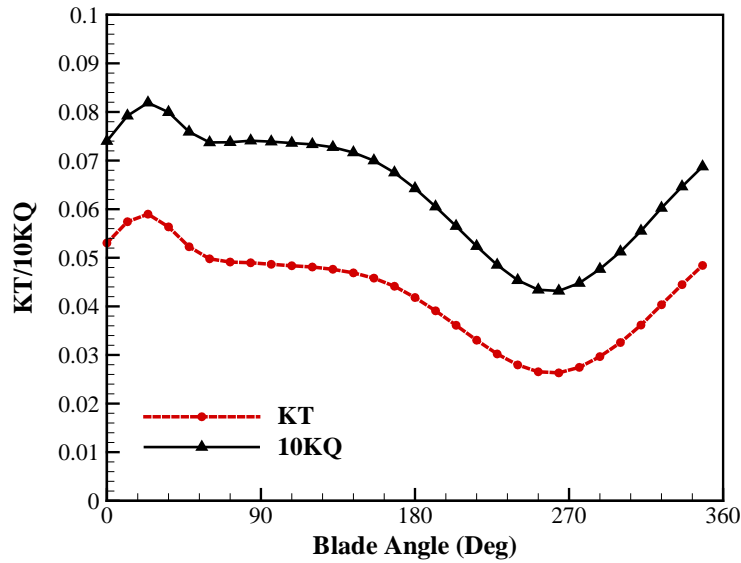
Figure 5.23: Thrust coefficient (single blade) and torque coefficient (single blade) on the key blade as a function of the blade angle.

5.3 HULL-PROPELLER-RUDDER INTERACTION SOLVED BY UNSTEADY BEM/RANS

5.3.1 Description of the problem

In the previous application, the ship hull moves at a constant speed and the time-averaged non-axisymmetric BEM/RANS approach is used. The scheme solves for the periodical propeller performance as a function of the blade angle.

If the velocity around the ship hull changes over time, the propeller performance will no longer be a periodical function. Therefore, for those hull-propeller-rudder interaction problems that involve non-zero ship hull accelerations, the unsteady BEM/RANS scheme needs to be used.

The ship hull geometry, rudder geometry, and propeller geometry in this application are the same as those described in Chapter 5.2 and Chapter 4.4. However, the velocity of the ship is no longer a constant. Two different types of ship motions are tested:

120

- **Straight acceleration case**

    In this application, the ship initially moves at 1.0 m/s towards the forward direction. After the flow around the ship hull is stabilized, a constant axial acceleration is applied to the ship hull which increases the ship speed to 1.2 m/s linearly with respect to time. The acceleration last three propeller revolution periods. After the acceleration, the ship speed remains at 1.2 m/s for the rest of the simulation. The propeller's angular velocity does not change during the iteration. The initial advance ratio (before acceleration) used in this application includes 0.6, 0.8, and 1.0.

- **Turning (maneuvering) case**

    In this application, the ship speed remains at 1.0 m/s while the advance ratio is set to a constant (0.6 or 0.8) throughout the simulation. However, after the flow around the ship hull is stabilized, the ship hull begins to turn to its starboard side. It takes two propeller revolution periods for the ship to linearly accelerate to the maximum turning rate (yaw rate). After the two revolution periods, the ship remains at the maximum turning rate. The center of the turn is located on the ship centerline plane and at 57% of the ship waterline length from the ship stem. Multiple turning rates are used in this application, ranging from 0.417 degrees/second to 1.251 degrees/second. It is worth noting that the rudder is fixed during the maneuvering process. This reduces the complexity of the RANS model and is for testing purpose only. In a real simulation, the rudder's motion should be included.

5.3.2 Description of the numerical model

For both the straight acceleration application and the turning application, the hull-propeller-rudder interaction problem is solved by the unsteady BEM/RANS scheme. The unsteady BEM solver is coupled with the unsteady RANS solver.

In the BEM model, 60×25 panels are placed on the blade surface while 66×10 panels are used for the hub surface between two blades, as shown in Figure 5.24. A PSF-2 type wake alignment is used. The boundary layer correction is not included in this case due to convergence issues.

The RANS model divides the computational domain into an inner zone and an outer zone. The outer zone contains 3.2 million polyhedron cells and ranges from -50D to +50D in the longitudinal direction, from -43D to +43D in the transverse direction, from -32D up to the free surface in the vertical direction, as shown in Figure 5.25. A non-slip boundary is applied to the ship hull surface and the rudder surface, while a slip-wall condition is used on the propeller shaft. A symmetry condition is used to represent the free surface. A zero-gradient condition is used for all the flow variables at the downstream boundary. At all other far field boundaries, the absolute velocity is set to zero.
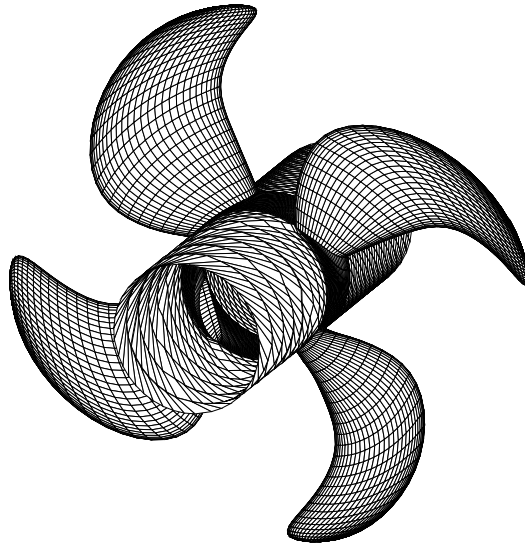
Figure 5.24: BEM model of the P2772 propeller geometry in the unsteady BEM/RANS application
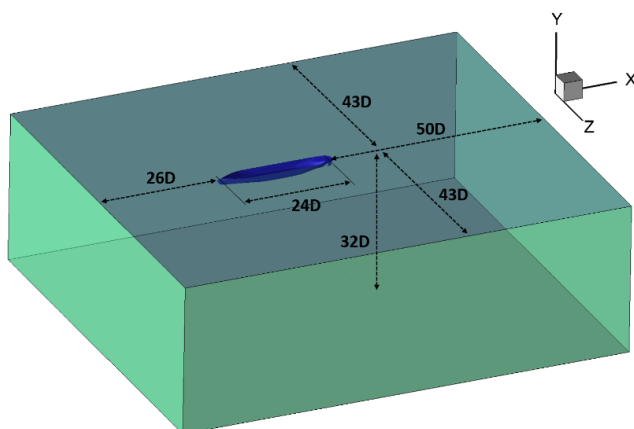
Figure 5.25: BEM model of the P2772 propeller geometry in the unsteady BEM/RANS application

The inner zone is where the body force term and the mass source term are applied. It contains 32×44×120 hexahedron cells and is connected to the outer zone via sliding interfaces. The cells in the inner zone follow that shape of the mean camber surface. More details about the inner zone can be found in Appendix B. The inner zone rotates with the propeller and is connected to the outer zone via sliding interfaces. Other settings for the RANS model are listed in Appendix C.

Unsteady RANS solves for the flow relative to the ship hull, a non-inertial frame of reference. The motion of the ship hull is considered by inertial force terms in the momentum equation. In the straight acceleration case, an acceleration term is added in the direction of the acceleration. In the turning case, a Coriolis term and a centrifugal term are added.

To validate the unsteady BEM/RANS, unsteady full-blown RANS simulations are also performed. In the full-blown RANS model, the outer zone remains the same. The inner zone is a full cylindrical zone that contains 1.35 million polyhedral cells and non-slip boundaries to represent the propeller blades. More details about the inner zone can be found in Chapter 4.4.2.

	Phase 1	**Phase 2**	**Phase 3**	**Phase 4**
Condition	Flow around ship hull stabilizes		Acceleration	Constant speed
Number of revolutions	60	8	3	6
Cumulative blade angle (degrees)	0-21600	21600-24480	24480-25560	25560-27720
Ship velocity (m/s)	1.0	1.0	1.0 → 1.2	1.2
Time step size in BEM/RANS	10 degrees	3 degrees	3 degrees	3 degrees
Time step size in full-blown RANS	10 degrees	1 degree	1 degree	1 degree

Table 5.2: BEM/RANS time step size and full-blown RANS time step size during four different simulation phases (straight acceleration case).

	Phase 1	**Phase 2**	**Phase 3**	**Phase 4**
Condition	Flow around ship hull stabilizes		Increasing yaw-rate	Constant yaw-rate
Number of revolutions	60	8	2	22
Cumulative blade angle	0-21600	21600-24480	24480-25200	25200-33120
Yaw rate (degrees/second)	0.0	0.0	0.0 → Max	Max
Time step size in BEM/RANS	10 degrees	3 degrees	3 degrees	3 degrees
Time step size in full-blown RANS	10 degrees	1 degree	1 degree	1 degree

Table 5.3: BEM/RANS time step size and full-blown RANS time step size during four different simulation phases (turning case).

To reduce the computational cost and ensure the consistency between the unsteady BEM/RANS model and the unsteady full-blown RANS model, the simulation is divided into several phases. Each phase uses a different time step size, as shown in Table 5.2 and Table 5.3. Here, the equivalent time step size is defined as the propeller rotation angle during a time step. Finally, the computational cost for both cases is shown in Table 5.4. The unsteady BEM/RANS scheme also reduces the mesh preparation cost by roughly a half because the inner zone mesh can be generated automatically. This is especially useful when the propeller geometry needs to be changed multiple times during propeller design.

	Number of Revolutions	Computational Cost[4]	
		unsteady BEM/RANS	full-blown RANS
Straight Acceleration	77	9 hours	55 hours
Turning Case	92	13 hours	76 hours

Table 5.4: Comparison of the computational cost of the unsteady BEM/RANS scheme and the unsteady full-blown RANS scheme.

5.3.3 Results of the straight acceleration case

With the straight acceleration application, the effect of the skin friction as body force is first studied. Since the skin friction is currently calculated by an empirical skin friction coefficient, it is important to know how much difference this skin friction can make towards the body force field. Two cases are tested. In the first case and all other unsteady applications in this dissertation, the skin friction is included in calculating the body force

---

[4] The computational cost is based on four computer nodes interconnected by 100Gbps Intel Omni-Path network. Each node contains two Intel Xeon Platinum 8160 CPUs. (4 nodes × 48 cores × 2.1 GHz)

field. In the second case, the skin friction is not included in the body force field. Comparison of the predicted propeller forces from both cases is given in Figure 5.26. As shown in the figure, the difference between the two cases is negligible. Therefore, the empirically determined skin friction coefficient does not play an important role in the body force field.
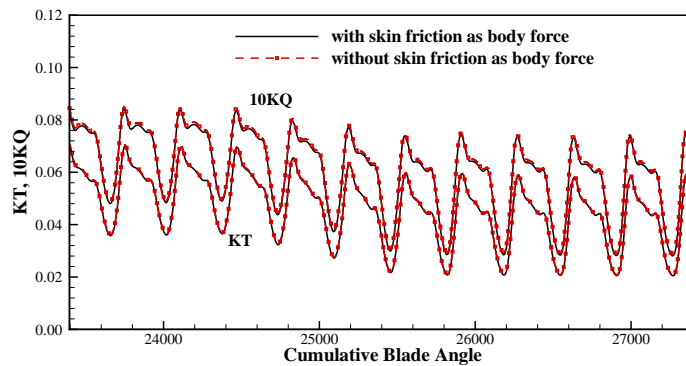
Figure 5.26: Propeller forces predicted by the unsteady BEM/RANS scheme under two conditions: the skin friction included as part of the body force term and the skin friction not included in the body force term.

In Figure 5.27, the effective wake field predicted by the unsteady BEM/RANS is plotted at the mid-chord slice of the inner zone. Since the effective wake can change with time in an unsteady simulation, the wake field from two different time-steps is given. The left figure shows the effective wake field before the acceleration (cumulative blade angle[5] equals to 24480 degrees) while the right figure shows the effective wake field after the acceleration period (cumulative blade angle equals to 25560 degrees). As shown in Figure 5.27, the velocity deficit caused by the ship hull boundary layer can be observed at around zero-blade-angle region in both time steps. There is also a strong vertical (+y) velocity

---

[5] Cumulative blade angle is the angle (in degrees) that the blade has rotated since the start of the simulation.

126

component due to the shape of the ship stern. After the acceleration, the increased axial component of the nominal wake leads to an increase in the axial effective wake velocity as well.

(before the acceleration period)   (after acceleration period)
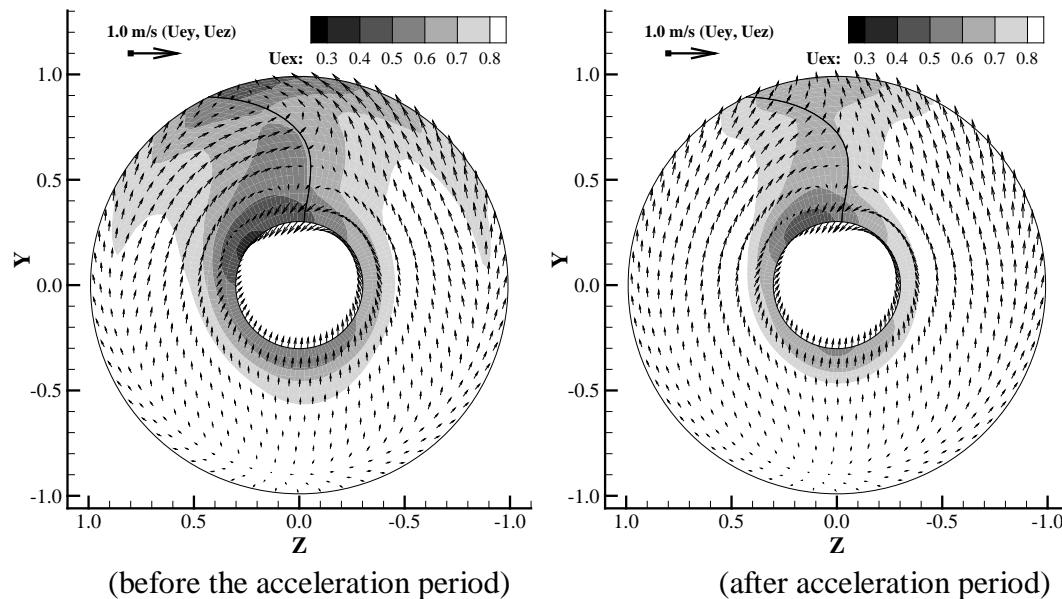
Figure 5.27: The effective wake field (Js = 0.6) plotted on the mid-chord slice in the straight acceleration case. The axial velocity component is shown by the contour while the in-plane velocity components are shown by arrows.

In Figure 5.28, the propeller forces predicted by the unsteady BEM/RANS scheme is compared with those predicted by the full-blown RANS. Three different advance ratios are tested. When the advance ratio is at 0.8 or 1.0, the results from both methods show good agreement. However, at a lower advance ratio (Js = 0.6), the difference becomes more significant, especially at around zero-degree blade angle before the acceleration. According to Figure 5.27, the effective wake reaches its lowest axial velocity value at around zero-degree blade angle. A lower axial effective wake means a higher propeller loading and a higher angle of attack for each section. As a result, the boundary layer at the suction side

of the blade becomes thicker and the boundary layer effect becomes more evident. The lack of boundary layer correction in this study causes the numerical error. This argument also explains why the numerical error becomes smaller after the acceleration period. The higher axial component of the incoming flow leads to a higher axial component of the effective wake. This reduces the angle of attack at zero-degree blade angle and, thus, reduces the effect of the boundary layer.

Figure 5.29 shows the pressure coefficient on the r/R = 0.44 section of the key blade at different blade angles. Results from the last acceleration revolution[6] of the Js = 0.8 case is shown. The pressure coefficient predicted by the unsteady BEM/RANS scheme is also compared with those predicted by unsteady full-blow RANS. In Figure 5.30 and Figure 5.31, similar plots are shown at r/R = 0.57 section and at r/R = 0.79 section. According to these results, a good agreement is found between the blade pressures predicted by the BEM/RANS scheme and predicted by the full-blown RANS scheme at higher radial stations. The error becomes larger at a lower radius, at the suction side of the blade, or close to the blade trailing edge. Possible explanations for these differences include:

- The current scheme assumes the streamline follows a cylindrical surface and the effective wake does not change in time or along the streamline. This leads to an accumulation of numerical error along the streamlines and, therefore, makes the pressure near the trailing edge more problematic.
- Absent of the boundary layer correction causes a numerical error, especially at the suction side near the trailing edge.
- Inaccurate representation of the blade when the thickness is higher. (The blade thickness is higher at lower radius)

---

[6] Cumulative blade angle ranges between 25200 degrees and 25560 degrees.
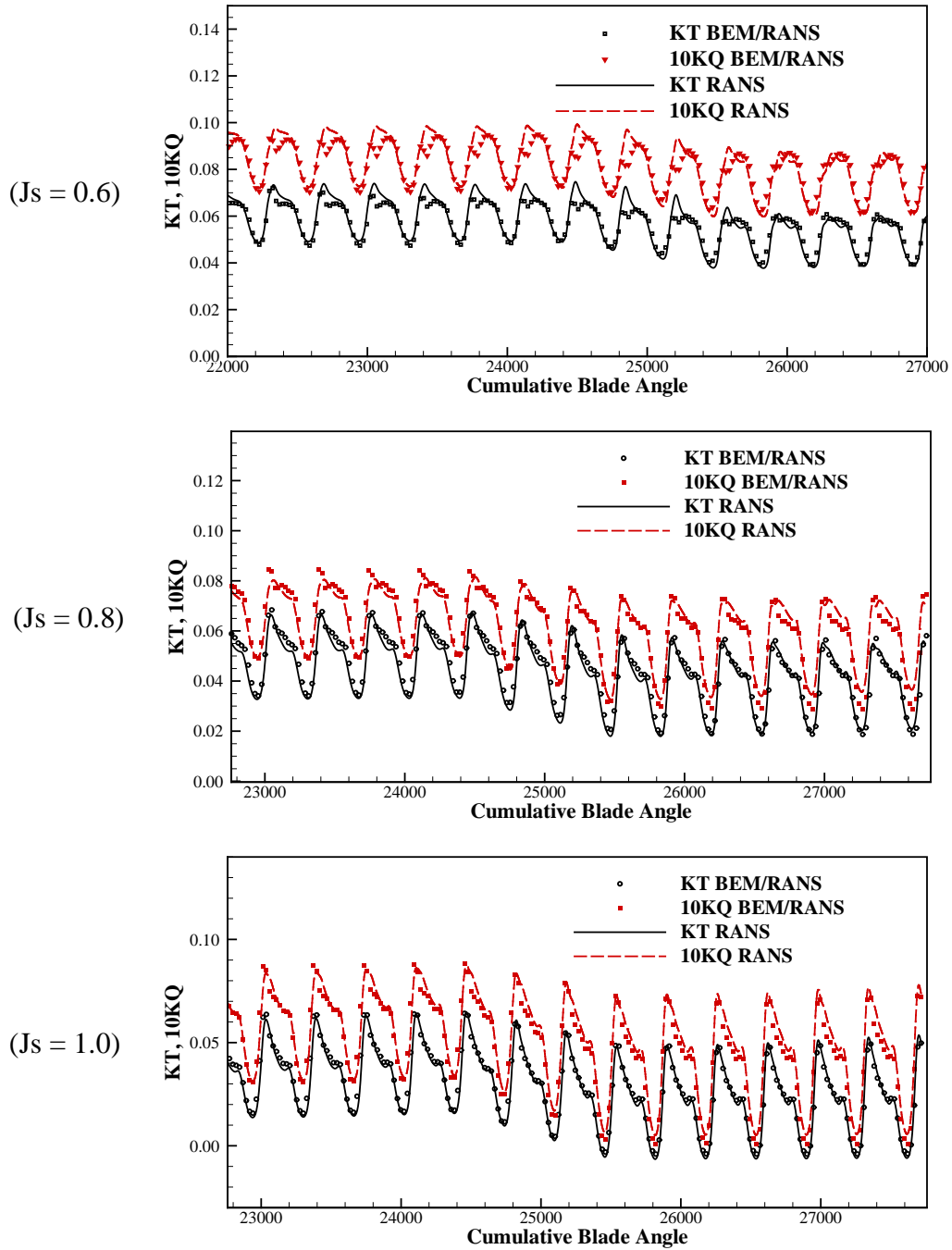
Figure 5.28: Propeller forces predicted by the unsteady BEM/RANS and by the unsteady full-blown RANS. The acceleration starts when the cumulative blade angle reaches 24480 degrees and finishes when the cumulative blade angle reaches 25560 degrees.

(0-degree blade angle)　　　　(90-degree blade angle)

(180-degree blade angle)　　　　(270-degree blade angle)
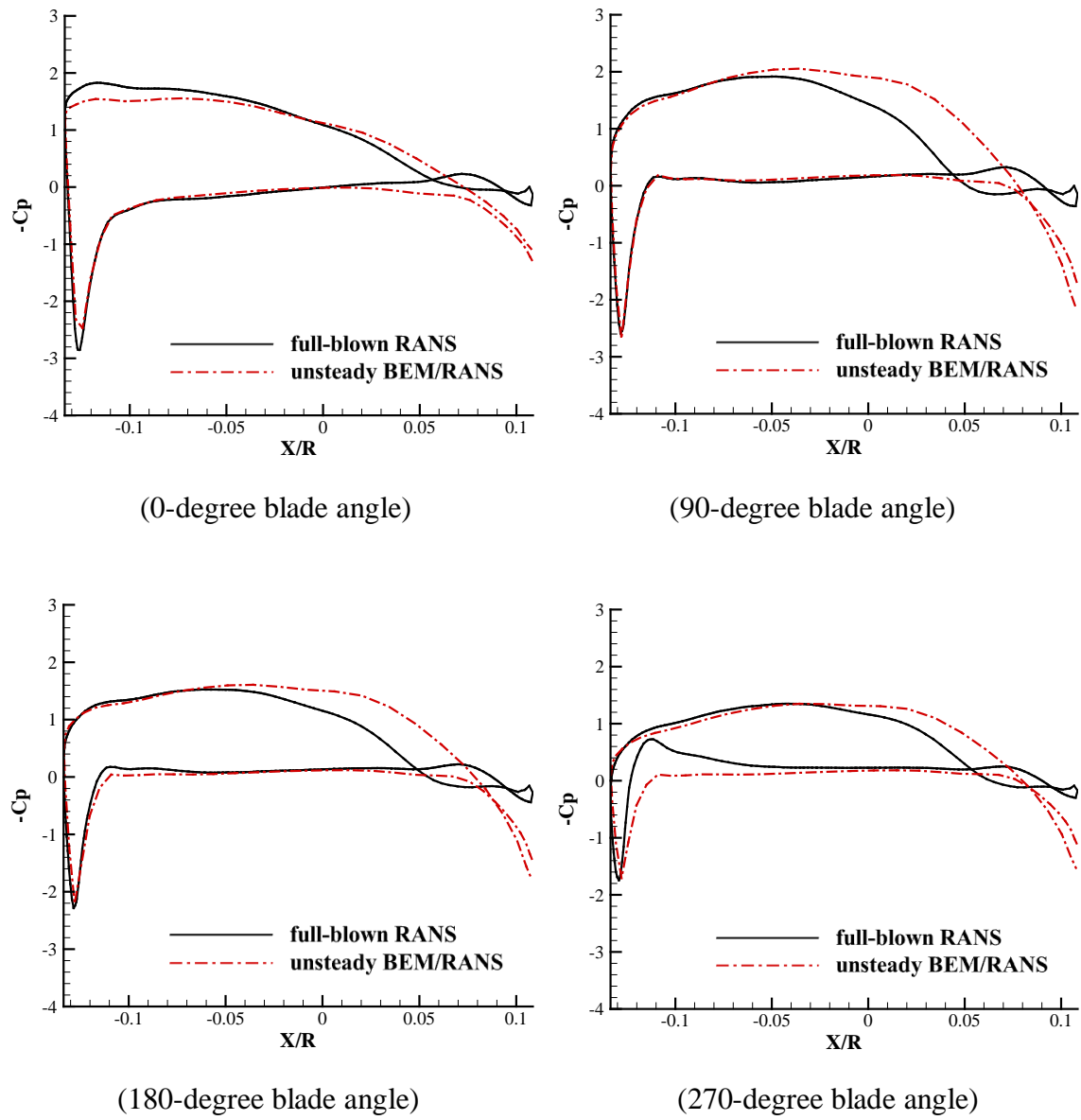
Figure 5.29: Pressure coefficient (Js = 0.8) at the r/R = 0.44 section of the blade surface. The pressure data is obtained on the key blade at four different blade angles of the last acceleration revolution (cumulative blade angle between 25200 degrees and 25560 degrees).

(0-degree blade angle)

(90-degree blade angle)

(180-degree blade angle)

(270-degree blade angle)
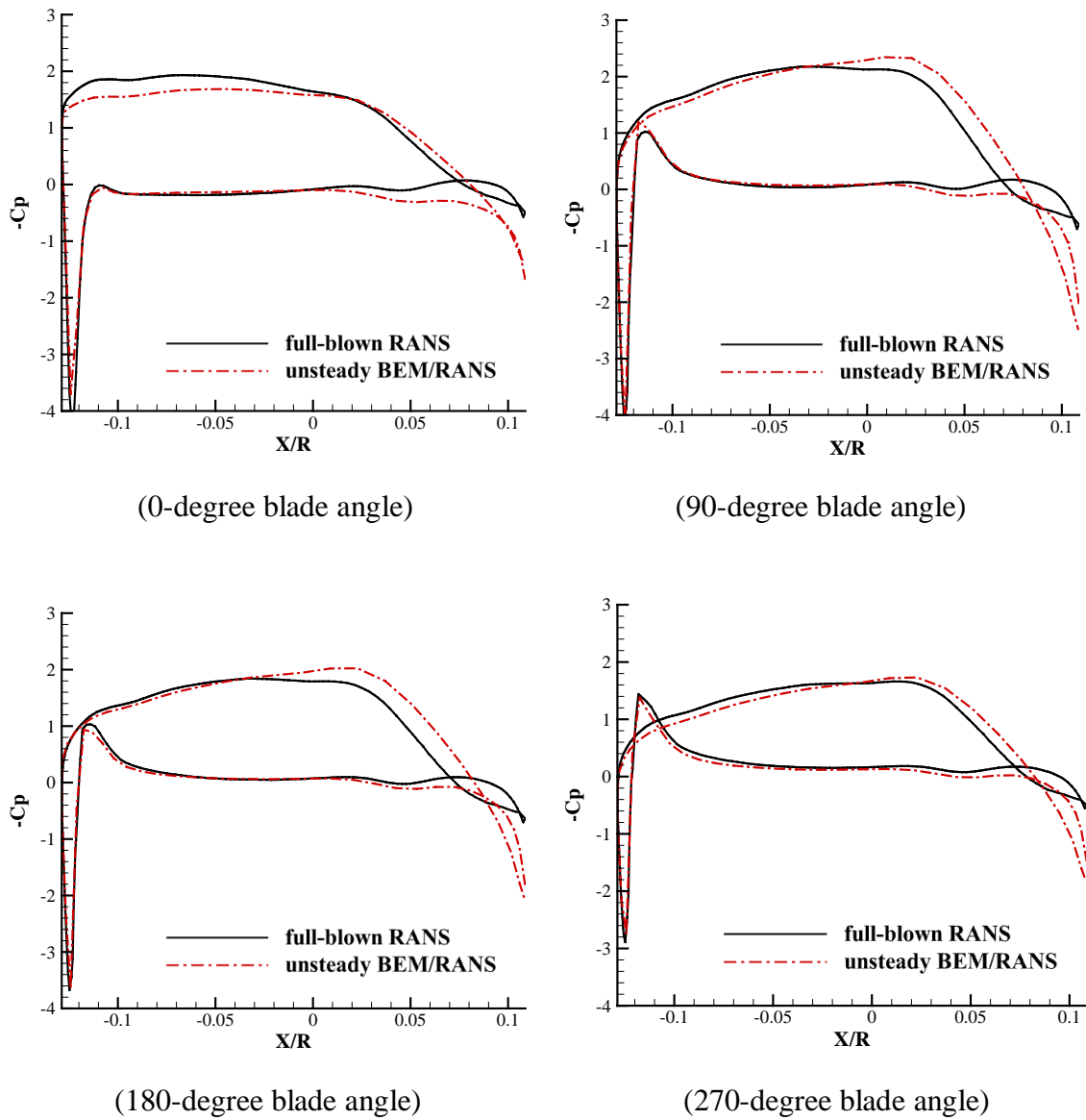
Figure 5.30: Pressure coefficient (Js = 0.8) at the r/R = 0.57 section of the blade surface. The pressure data is obtained on the key blade at four different blade angles of the last acceleration revolution (cumulative blade angle between 25200 degrees and 25560 degrees).

(0-degree blade angle)

(90-degree blade angle)

(180-degree blade angle)

(270-degree blade angle)
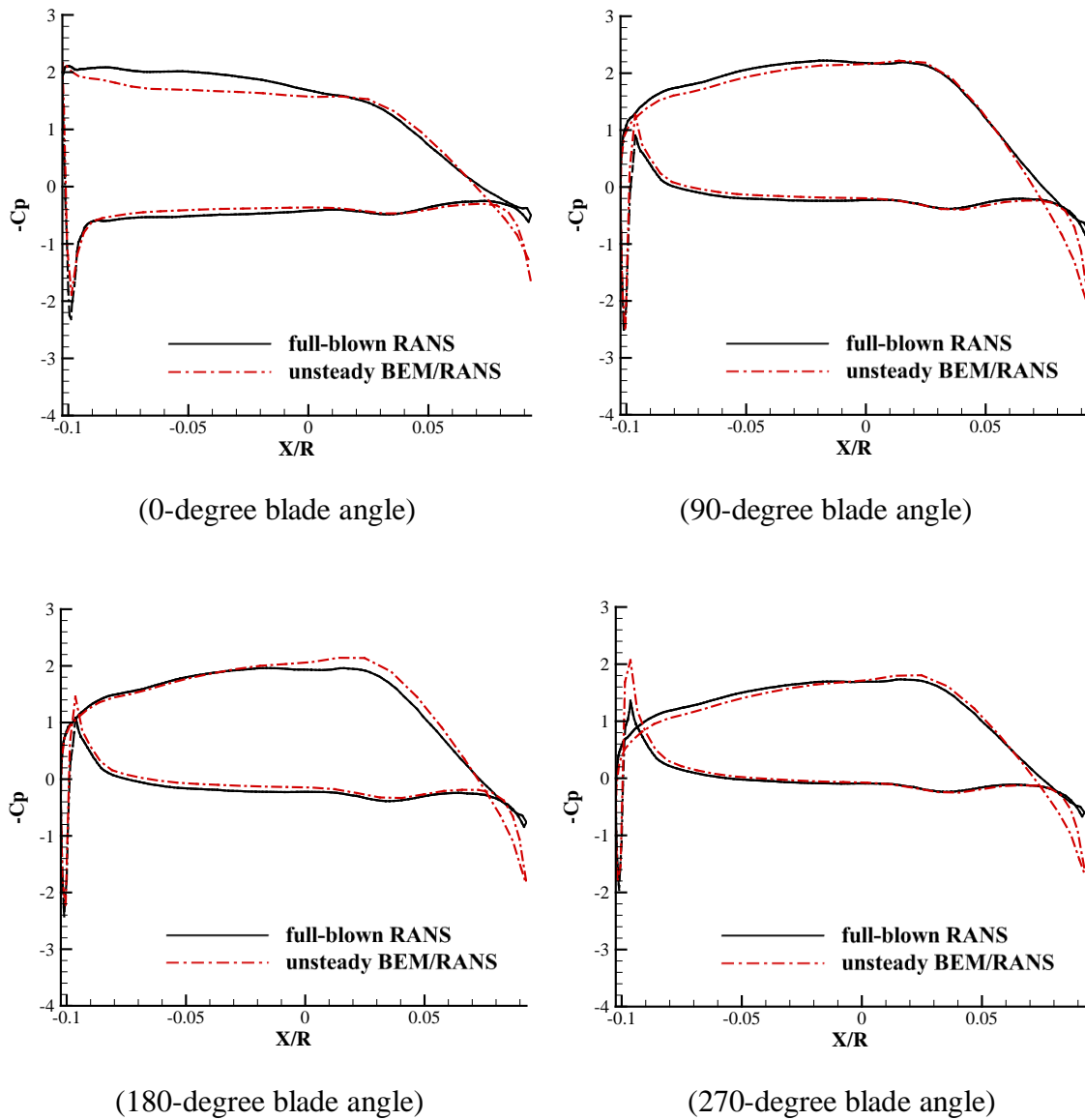
Figure 5.31: Pressure coefficient (Js = 0.8) at the r/R = 0.79 section of the blade surface. The pressure data is obtained on the key blade at four different blade angles of the last acceleration revolution (cumulative blade angle between 25200 degrees and 25560 degrees).

5.3.4 Results of the turning case

Four cases are tested in this application. First, the maximum turning rate is set at 0.417 degrees/second while different advance ratios are tried, including Js = 0.6 and Js = 0.8. Then, the advance ratio is set to 0.8 while different maximum turning rates are tested, including 0.417 degrees/second, 0.834 degrees/second, and 1.251 degrees/second.

The ship hull movement is plotted at different cumulative blade angles, as shown in Figure 5.32. The maximum turning rate used in this figure is 1.251 degrees/second.
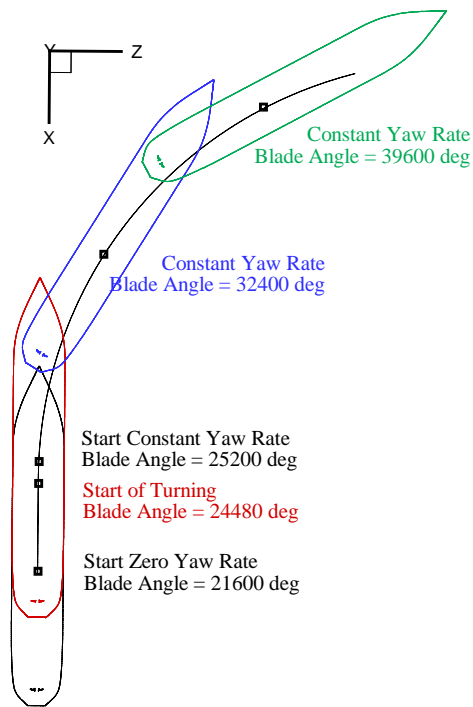
Figure 5.32: Locations of the ship hull at different cumulative blade angles.

In Figure 5.33, the effective wake field predicted by the unsteady BEM/RANS is plotted at the mid-chord slice of the inner zone. The wake field is obtained both before the turning (left figure) and during the constant-yaw-rate period (right figure). As shown in Figure 5.33, the axial component of the effective wake field at the constant turning period

is similar to the axial effective wake field before the turning starts. The velocity deficit region is pushed to the starboard side during the turning. A strong transverse flow component (+Z direction) can also be observed. These are due to the strong cross flow caused turning motion of the ship. The long distance from the propeller to the center of the turning leads to a large cross-flow component even if the yaw-rate is small.

(before the turning period)   (constant-yaw-rate turning period)
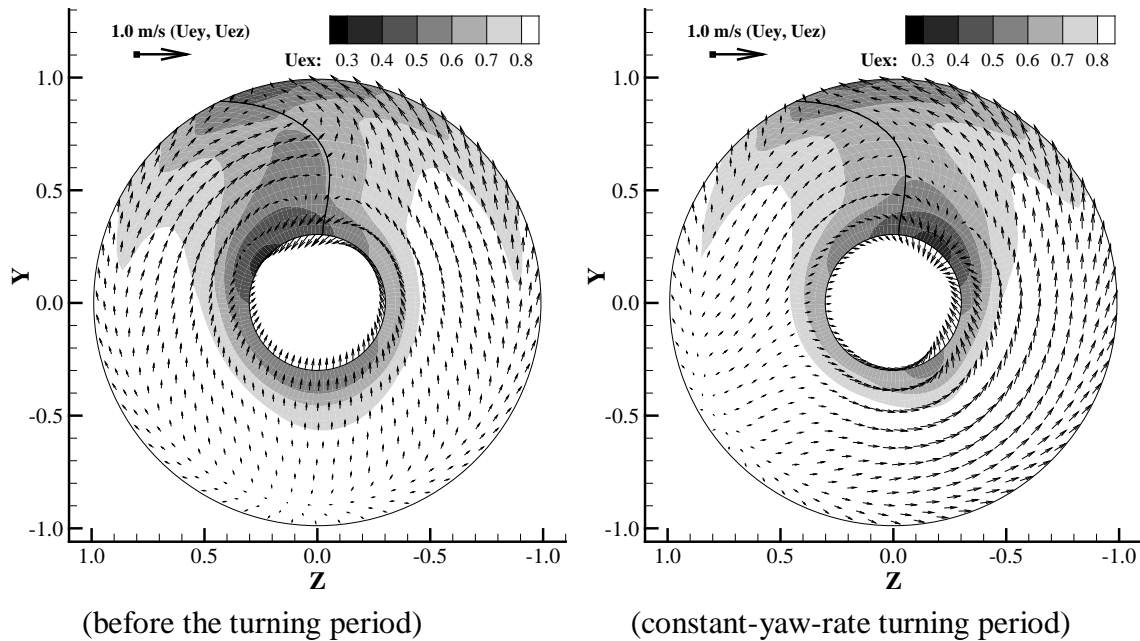
Figure 5.33: The effective wake field (Js = 0.6) plotted on the mid-chord slice in the turning case. The axial velocity component is shown by the contour while the in-plane velocity components are shown by arrows.

In Figure 5.34, the propeller forces predicted by the unsteady BEM/RANS scheme is compared with those predicted by the full-blown RANS. Two different advance ratios are tested. Similar to the previous observation, the results from both methods show good agreement at higher advance ratios (Js = 0.8). The difference becomes more significant when the advance ratio decreases to 0.6.

134
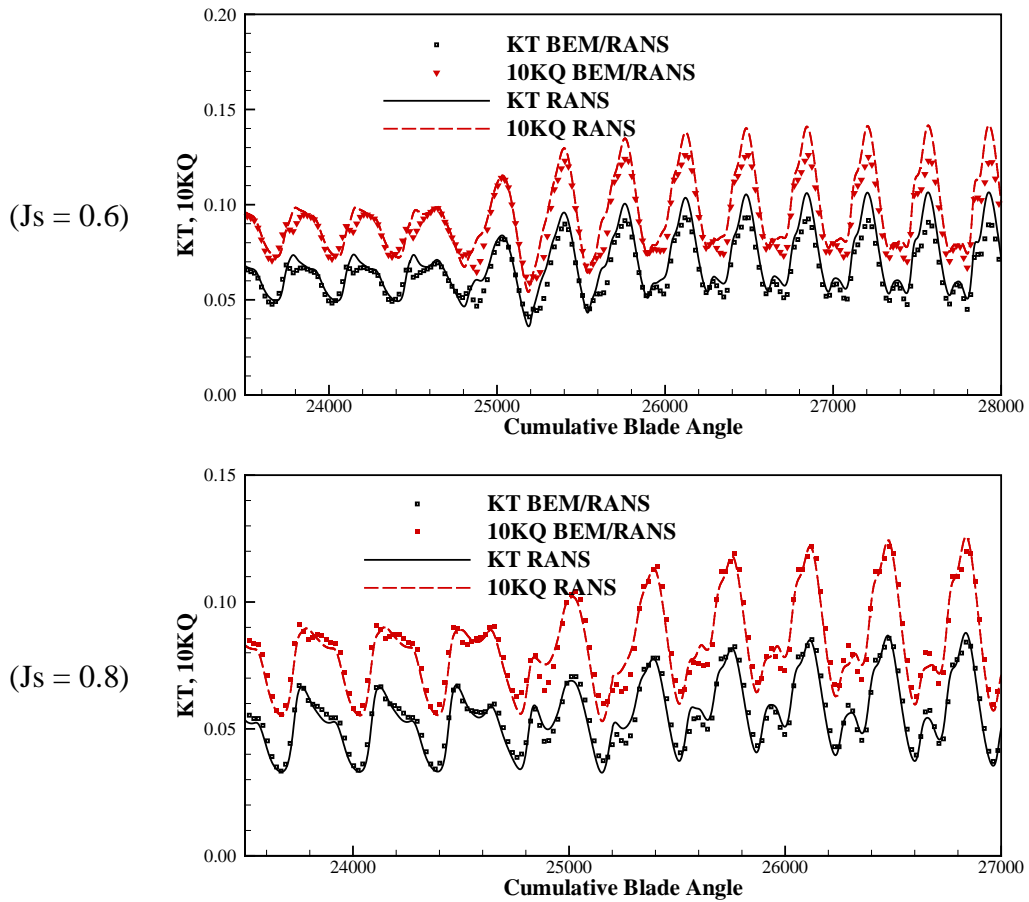
Figure 5.34: Propeller forces predicted by the unsteady BEM/RANS and by the unsteady full-blown RANS. The ship starts to turn when the cumulative blade angle reaches 24480 degrees and begins the constant-yaw-rate turning when the cumulative blade angle reaches 25200 degrees.

Figure 5.35 shows the vorticity fields at the y = 0 slice from both the unsteady BEM/RANS simulation and the unsteady full-blown RANS simulation. Due to the use of the unstructured mesh in this application, the artificial diffusion at the downstream is much stronger than the case with structured mesh (refer to Chapter 4.4 and Chapter 4.5).
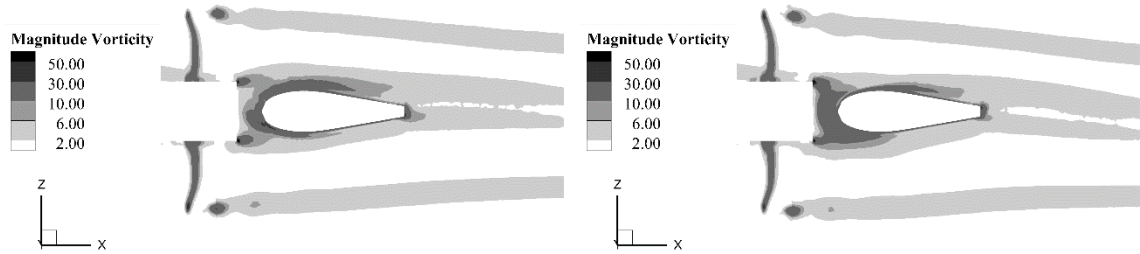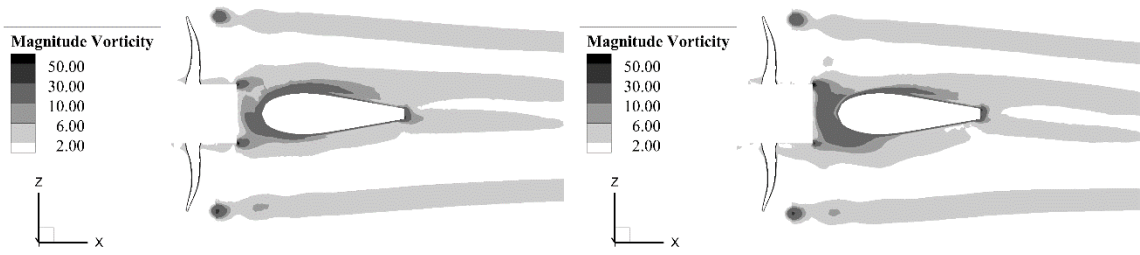
(before the turning period)

(cumulative blade angle: 24480 degrees)

(1 revolution into the turning period)

(cumulative blade angle: 24840 degrees)
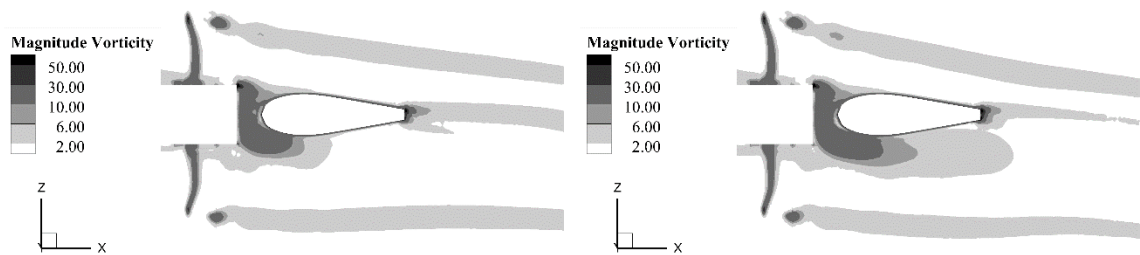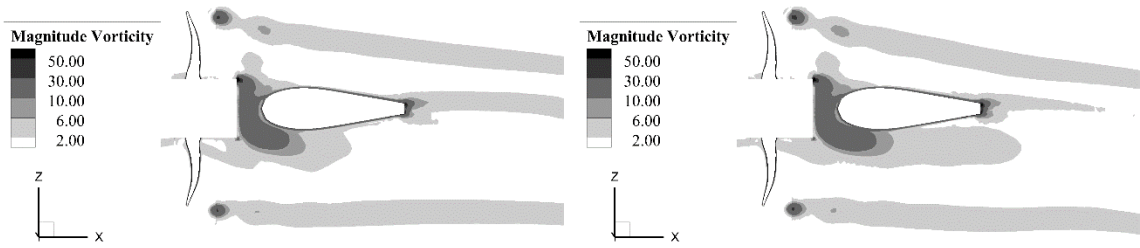
(start of the constant-yaw-rate turning)

(cumulative blade angle: 25200 degrees)

(3 revolutions into the turning period)

(cumulative blade angle: 25560 degrees)

136
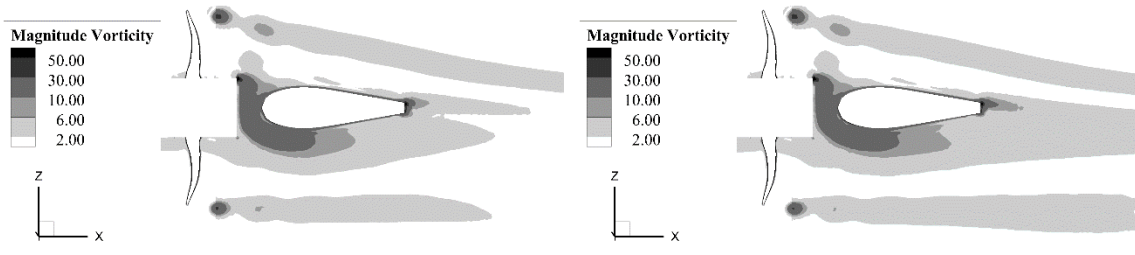
(4 revolutions into the turning period)   (5 revolutions into the turning period)

(cumulative blade angle: 25920 degrees)   (cumulative blade angle: 26280 degrees)
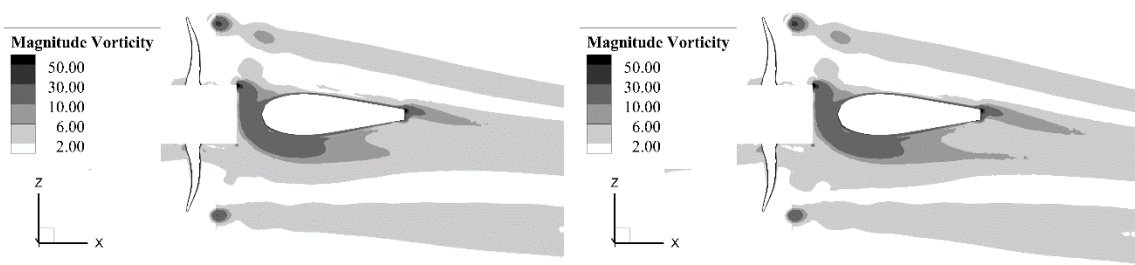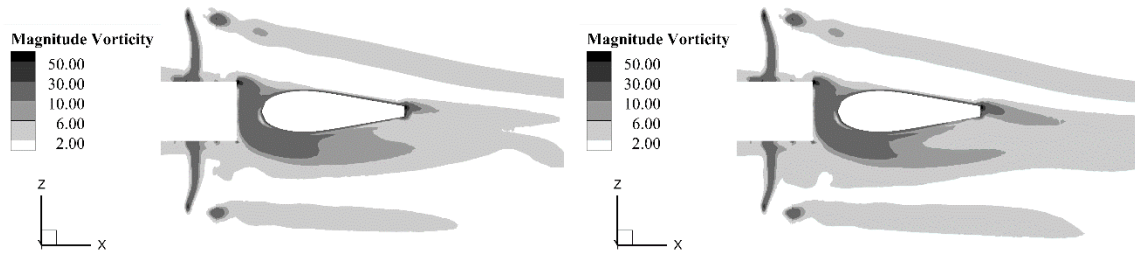
(6 revolutions into the turning period)   (7 revolutions into the turning period)

(cumulative blade angle: 26640 degrees)   (cumulative blade angle: 27000 degrees)

137

(8 revolutions into the turning period)   (9 revolutions into the turning period)

(cumulative blade angle: 27360 degrees)   (cumulative blade angle: 27720 degrees)
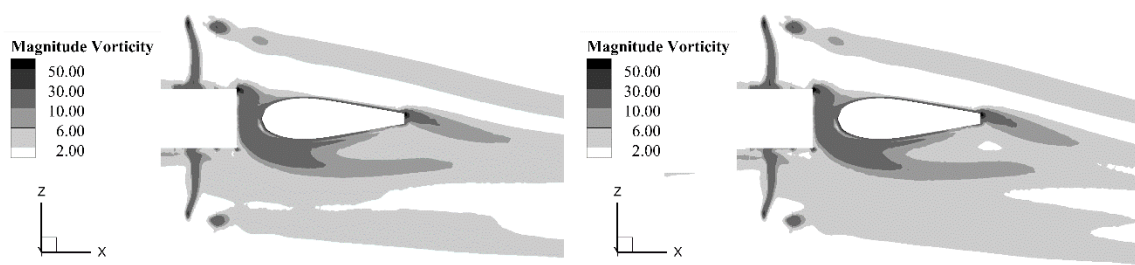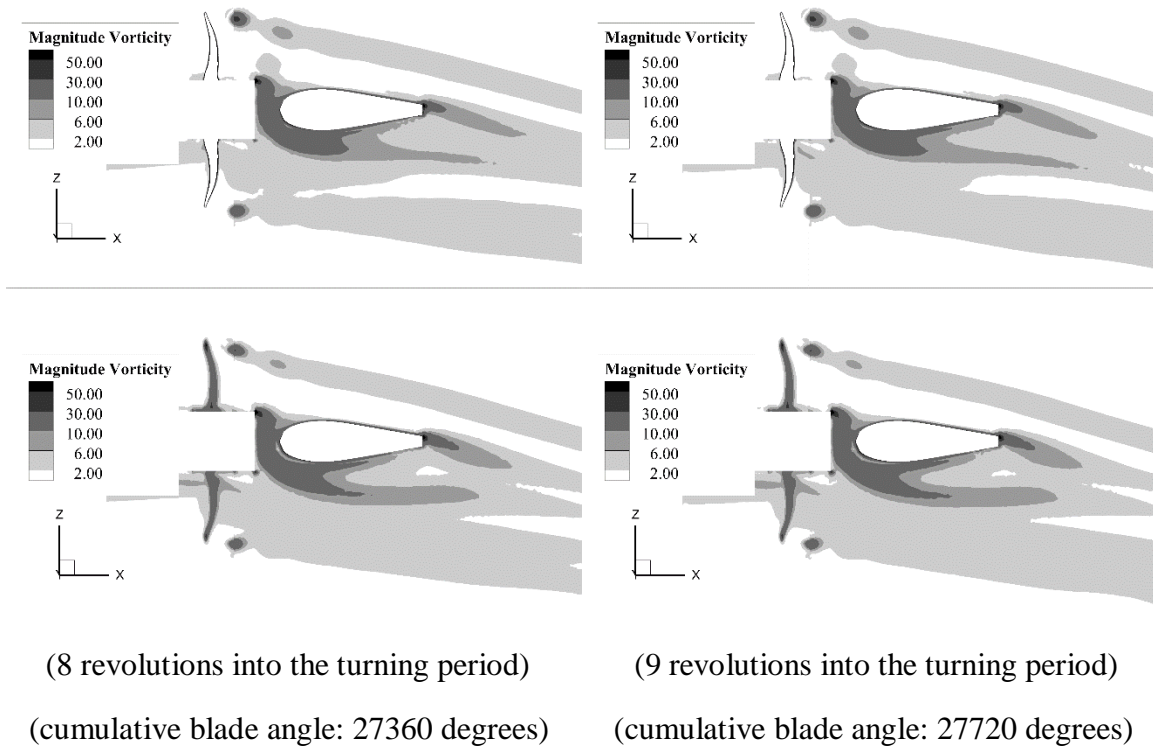
Figure 5.35: Comparisons of vorticity fields (at the $y = 0$ slice) from unsteady
BEM/RANS scheme (upper figures) and from unsteady full-blown RANS
(lower figures).

Turning Rate	0.417 degrees/sec		0.834 degrees/sec		1.251 degrees/sec	
	KT	10KQ	KT	10KQ	KT	10KQ
Full-blown RANS	0.223	0.333	0.229	0.345	0.234	0.351
Unsteady BEM/RANS	0.224	0.324	0.224	0.324	0.224	0.324
Error	0.4%	-2.7%	-2.1%	-6.2%	-4.2%	-7.8%

Table 5.5: Mean propeller forces during a constant-yaw-rate turning. The numerical error
of the unsteady BEM/RANS scheme is given at different turning speed. The
unsteady full-blown RANS result is set as the reference value.

138

Finally, the advance ratio is set to 0.8 while three different maximum turning rates are tested. Full-blown RANS simulations are also performed and used as the reference. The numerical error of the propeller forces predicted by the BEM/RANS scheme is shown in Table 5.5. As the turning rate increases, the numerical error of both the thrust coefficient and the torque coefficient become larger. This is due to the strong cross flow (in the +Z direction) caused by the ship hull yaw motion. Current BEM scheme uses a rigid wake alignment scheme (PSF-2 type). In other words, the trailing wake surface is determined at the beginning of the simulation and does not change with the inflow conditions. A stronger cross-flow component means a larger difference between the rigid wake geometry and the real wake geometry. Therefore, a larger numerical error is expected.

It is worth noting that the rudder is fixed during the maneuvering process. This reduces the complexity of the RANS model and is for testing purpose only. In a real simulation, the rudder's motion should be included.

Chapter 6.   Conclusions and Recommendations

6.1 CONCLUSIONS

In this dissertation, the boundary element method (BEM) is coupled with the Reynolds Averaged Navier-Stokes method (RANS) to solve the multibody interaction problems in the ship propulsion system. Take the hull-propeller-rudder interaction problem as an example. First, the propeller-induced flow is decoupled from the total flow based on the fact that the propeller is smaller in dimensions and faster in its movement compared to the ship hull. While RANS can be used to calculate the "slow-changing" (or steady) total flow around the ship hull, BEM is applied to the "rapid-changing" propeller-induced flow. In the RANS model, instead of using non-slip wall boundaries with a body-conforming mesh, the propeller blades are represented by a body force field and a mass source field. Both terms are calculated by the potential solver. On the other hand, the total flow from RANS is used by BEM to calculate the unsteady effective wake field.

Due to the use of the body force field and the mass source field to represent the propeller blades in RANS, the influence from the propeller blades can be time-averaged in a larger time-step. In other words, it is possible for RANS to use a larger time step size than BEM. If the ship moves at a constant speed and direction, even a steady RANS solver can be used. Furthermore, if the upstream body is axisymmetric, the steady 3-dimensional solver can be reduced to a 2-dimensional axisymmetric one. All of these significantly reduce the number of iterations required by a RANS and the matrix dimensions in RANS. Both lead to a gain in the numerical efficiency.

The BEM/RANS scheme can be implemented with an unsteady approach, a steady non-axisymmetric approach, and a steady axisymmetric approach. The dissertation starts

by introducing the theories and implementations of the steady and unsteady (periodical and non-periodical) boundary element methods. Then, all three BEM/RANS approaches are described together with multiple ways to calculate the body force field, the mass source field, and the effective wake field.

In the unsteady BEM/RANS scheme, a special inner zone mesh arrangement is used so that the body force field and mass source field are confined to one layer of cells per blade. This further reduces the number of cells in RANS and increases the time-step size. The highly confined body force distribution also enables the calculation of the effective wake field closer to the blade. To be compatible with this inner zone mesh arrangement, a camber-distribution model is used to calculate the body force field and mass source field from the propeller surface pressure and the propeller surface source distribution. Numerical study based on an open propeller and a uniform inflow also shows that, in order to get an accurate prediction of the unsteady effective wake, it is important to calculate the blade-induced velocity from an integration over the mean camber, instead of the blade surface.

Similar numerical studies are also performed with the axisymmetric version of the BEM/RANS scheme. Results show that the use of both mass source term and compensating force term is essential to reduce the numerical error on the predicted effective wake field.

Finally, unsteady BEM/RANS scheme is applied to the hull-propeller-rudder interaction problem at ship acceleration or ship turning. The non-axisymmetric BEM/RANS scheme is used to solve a contra-rotating propeller and a hull-propeller-rudder interaction at a constant ship motion. Results show that by considering the interactions between the propeller and it vortical incoming flow, the numerical error of the thrust predicted by the non-axisymmetric BEM/RANS scheme reduces from 13% to 1%. The unsteady BEM/RANS scheme is also shown to behave well except for some extreme cases,

including low advance ratios, high turning rates, etc. Computational cost analysis shows the unsteady BEM/RANS scheme is around 6 times faster than a fully RANS simulation. The unsteady BEM/RANS scheme also reduces the mesh preparation cost by roughly a half. This is more useful when the propeller design needs to be changed multiple times during the design.

6.2 MAJOR CONTRIBUTIONS

The main contributions of the present work are:

1. The time-averaged BEM/RANS approach is developed based on several existing studies from other researchers (Choi 2001, Tian et al. 2014), an unsteady periodical BEM solver (PROPCAV), and a commercial CFD solver (Fluent). Based on this time-averaged implementation, numerical studies are made on whether to include and how to include the mass source term and the compensating force term.

2. The unsteady periodical BEM solver is improved to handle the non-periodical problems. Based on this non-periodical BEM, the unsteady BEM/RANS approach is developed. Unlike other existing unsteady BEM/RANS implementations which rely on a highly refined RANS mesh in the body force zone, this scheme uses a special mesh arrangement and confines the body force field and the mass source field into only one layer of cells (per blade). As a result, this method does not rely on a highly-refined mesh in the body force region and, therefore, reduces the number of cells as well as the number of required iterations. Also, this scheme evaluates the effective wake at a small constant offset from the mean camber control points, unlike other existing unsteady BEM/RANS schemes in which the

effective wake is usually evaluated at an upstream disk. This reduces the numerical error of the effective wake field and can be especially useful in representing the influence of the rudder to the blade.

3. Different ways of calculating the mass source field, body force field, and effective wake field are studied. In order to get an accurate prediction of the effective wake, a necessary condition is provided in choosing the body force (mass source) distribution model and the effective wake calculation model.

6.3 RECOMMENDATIONS

In order to reduce the numerical error and further improve the computational efficiency, the following improvements can be made to the current scheme.

6.3.1 Larger time step size in RANS

In the current scheme, the RANS solver and the BEM solver share the same time step size. This restriction can be removed so that the RANS solver can have a larger time step size compared to BEM. This is reasonable because RANS is used to solve the slow-changing total flow. The rapid-changing propeller-induced flow is handled by the BEM solver which requires a smaller time step size.

To achieve this, the time-stepping scheme should be modified. Numerical studies have shown that the unsteady BEM/RANS scheme requires an implicit scheme to update the effective wake field, body force field, and mass source field. More specifically, if a RANS time step covers multiple BEM steps, the implicit scheme requires the BEM solver to go back a certain number of time steps and re-evaluate the BEM solutions within the RANS time step, as shown in Figure 6.1.

143
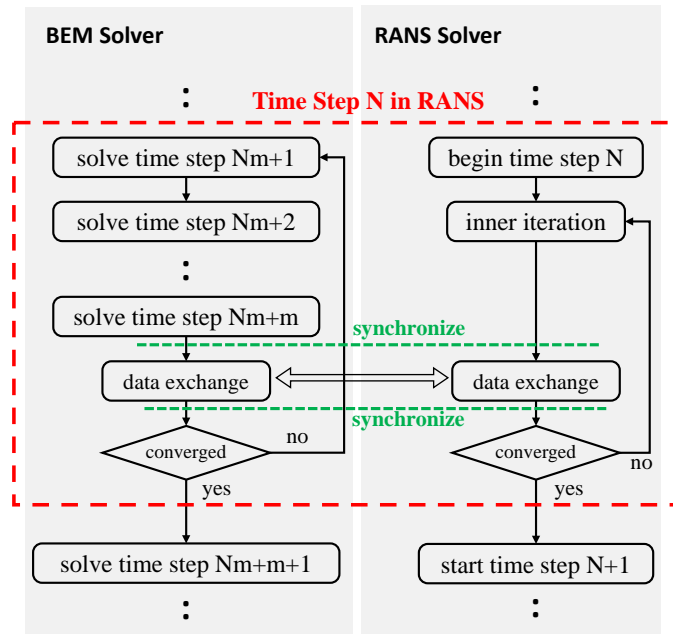
Figure 6.1: Flow chart of the unsteady BEM/RANS scheme with different time step sizes in RANS and in BEM.

6.3.2 More accurate calculation of blade surface pressure in BEM

In calculating the blade surface pressure, the current scheme assumes that the streamlines follow the cylindrical surface and also assumes that the time-derivative and streamwise-derivative of the effective wake equal to zero. With the unsteady non-uniform effective wake field, the validity of these assumptions needs to be studied.

To improve the current scheme, the non-uniform upstream total head should be calculated first. Then, the Bernoulli equation should be applied along streamlines on the propeller blade surface in order to calculate the pressure.

6.3.3 Improvement of numerical convergence

The current unsteady BEM/RANS scheme does not converge when the iterative pressure Kutta condition is used. Although its effects on the overall propeller forces are not significant, having the trailing edge pressures right is essential for super-cavity predictions and boundary layer corrections.

The efficiency and convergence of the boundary layer correction model should be improved so that the boundary layer correction can be added to the BEM/RANS scheme.

6.3.4 Adding other models to BEM

First, the unsteady wake alignment model can be added to the BEM solver of the unsteady BEM/RANS scheme. The current BEM/RANS approach uses a rigid wake surface which does not change in its shape when the inflow velocity is changed. This can cause a numerical error when the velocity of ship deviates from its initial value.

The cavitation model can also be added to the BEM/RANS scheme. The cavity is predicted by the BEM solver and then represented by a mass source field and a compensating force field inside RANS.

Appendix A.   Synchronization and Communication between PROPCAV and ANSYS Fluent

In the unsteady BEM/RANS scheme, the BEM solver and the unsteady RANS solver run simultaneously and exchange data multiple times during the process. The body force field, the mass source field, and the total flow field need to be transferred from one solver to the other. In order to establish communication between solvers, several techniques can be used:

- Shared memory is usually provided by operating systems as a basic library function. These kinds of functions provide communication channels between two processes that are running on the same computer. A shared memory region is allocated and then mapped to certain virtual address locations of both processes. This scheme is fast but does not prevent race conditions on the shared memory.

- The socket is a networking abstraction that exchanges data between servers and clients. The server and client do not have to be on different network addresses.

- Message passing interface also provides a high-level abstraction for sending and receiving messages. It is widely used for the high-performance-computing community.

- Files can also be used to exchange information between processes. Similar to the shared memory technique, the race condition should be avoided via external synchronization techniques.

In order to reduce the time cost of data exchange, the System V shared memory libraries is used for inter-process communication (IPC). The body force field, mass source

filed, and the total flow field is stored at different locations of the shared memory region. Therefore, only two types of race conditions can happen:

- The sender overwrites the data before the receiver finishes reading it;
- The receiver begins reading the data before the sender finishes writing it.

To avoid these race conditions, a synchronization step is applied both before and after the data exchange step. The System V semaphores are used for the multi-process synchronization.

Figure A.1 shows the location of each process in a multi-node parallel computing implementation. First, PROPCAV is paralleled via the OpenMP library and is located in node #1. ANSYS Fluent uses a distributed memory parallelization. The host process is located in node #1 and communicates with the PROPCAV solver. The body force/mass source data in the host process is sent to process #0 first and then broadcasted to all the other processes. The flow information in the propeller zone is collected by process #0 first and then send to the host process.
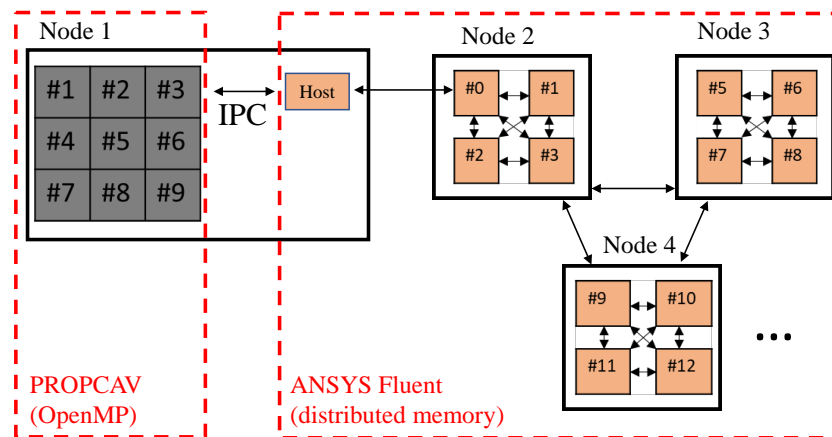
Figure A.1: Multi-node parallel computing structure of unsteady BEM/RANS scheme.

Appendix B. Meshing Strategy for the Body Force Zone in Unsteady BEM/RANS scheme

The mesh zone that contains the body force/mass source field in the unsteady BEM/RANS scheme is designed in a special way, as shown in Figure B.1 and Figure B.2. As shown in Figure B.2, the mean camber surface of the blade is aligned with the diagonal direction of the cells, so that the body force field and mass source field is contained in only one layer of cells (per blade). This greatly reduces the interpolation error and ensures the conservation of mass sources and conservation of propeller forces between the BEM solver and the RANS solver. It also reduces the thickness of the body force distribution which leads to a more accurate prediction of the effective wake field.
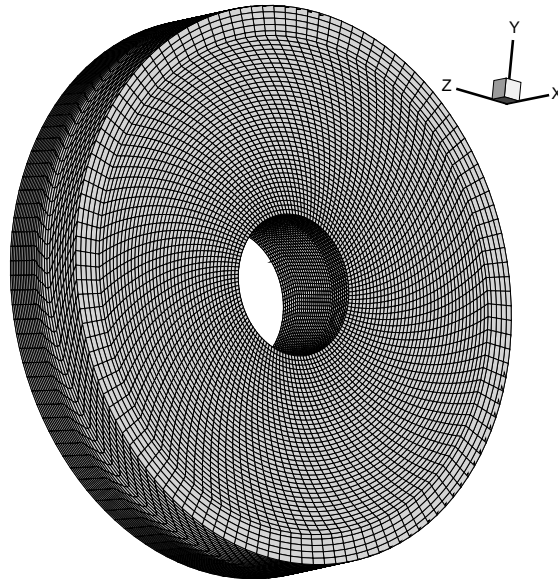
Figure B.1: Overview of body force mesh zone in the unsteady BEM/RANS approach.
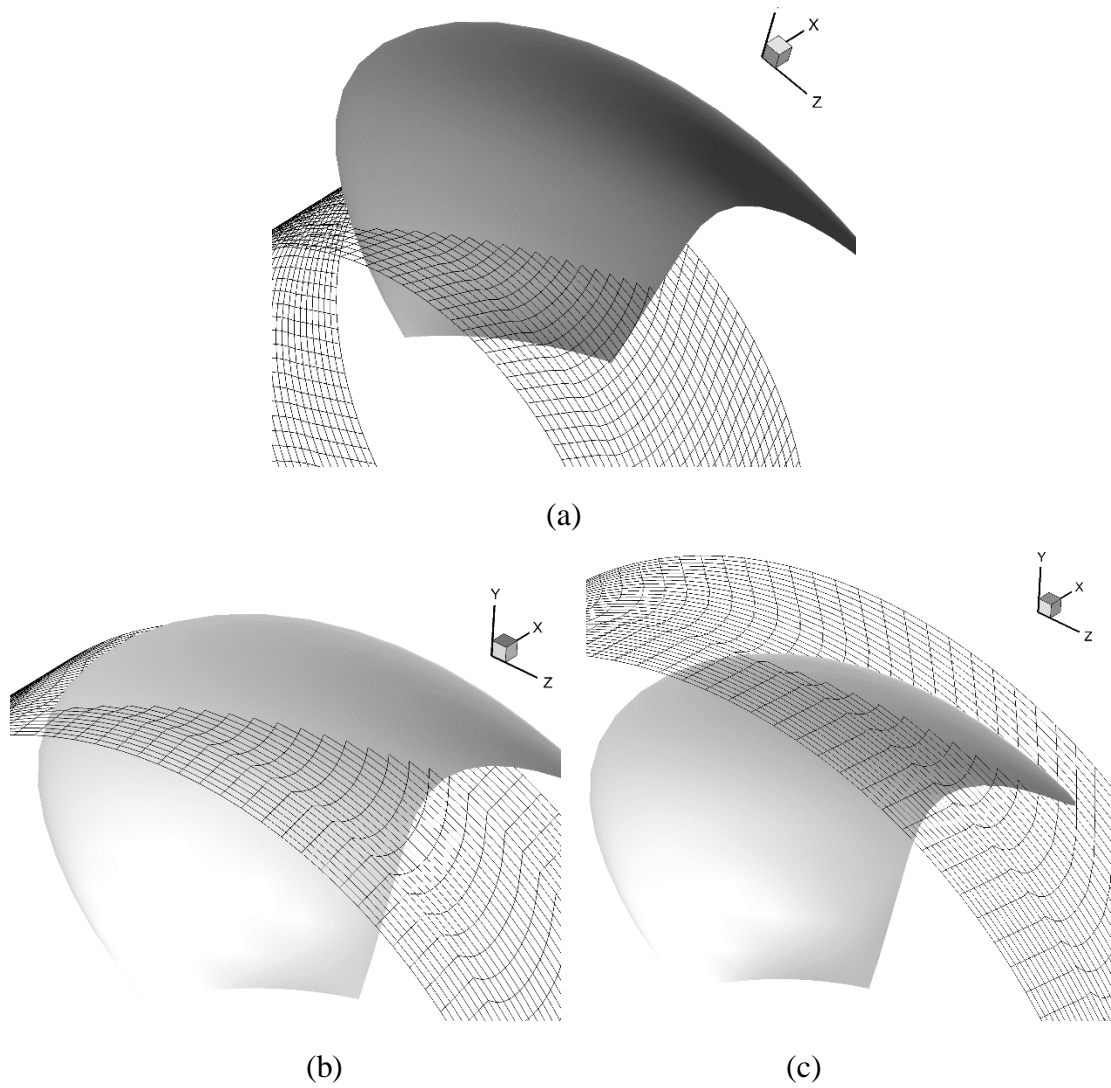
Figure B.2: Body force zone mesh slices at difference radius. The camber of the blade aligns with the diagonal direction of the cells.

Appendix C.   Basic Schemes and Models Used in the RANS Solver

The RANS solver used in this dissertation is ANSYS Fluent v18.2[7]. Multiple simulations are used in this dissertation. Although the physical problems and geometries they are dealing with may be different, these RANS solvers share lots of similarities in terms of interpolation schemes, discretization schemes, time-stepping schemes, etc. To reduce the complexity of describing all the RANS solver configurations for each simulation, these configurations are described in this part and used as the default settings unless otherwise described.

- Solver: incompressible segregated solver
- Velocity-pressure scheme: pressure-implicit with splitting of operators (Issa 1986)
- Turbulence model: k-ω SST with the following constant values

σ_{k1}	$\sigma_{\omega1}$	σ_{k2}	$\sigma_{\omega2}$	α_1	β_1	β_2
1.176	2.0	1.0	1.168	0.31	0.075	0.0828
α_∞^*	α_∞	α_0	β_∞^*	R_β	R_k	R_ω
1	0.52	1/9	0.09	8	6	2.95
ζ^*	M_{t0}					
1.5	0.25					

- Discretization and interpolation:
    - Flow variables are defined at cell centroid

---

[7] ANSYS Fluent: https://www.ansys.com/products/fluids/ansys-fluent

- Convection term: interpolation of velocity on cell faces is handled by second-order upwind
- Diffusion term: cell centroid velocity gradient is calculated by the least square method. Then, central difference scheme with deferred correction is used to calculate the face gradient.

- Time stepping scheme (in unsteady simulations): Second-order implicit
- Boundary conditions: non-slip boundary on the ship hull and the propeller blades; slip boundary on the hub; flow velocity is set at the upstream boundaries; the static pressure is given at downstream boundaries
- Relative motion: In the hull-propeller-rudder interaction case, the flow is solved in a reference frame fixed to the ship hull while the propeller rotation is handled by moving mesh. In the hull is not included, the flow is solved in a reference frame fixed to the propeller shaft.

References

Balaras, E. (2004). Modeling complex boundaries using an external force field on fixed Cartesian grids in large-eddy simulations. Computers & Fluids, 33(3), 375-404.

Balaras, E., Schroeder, S., and Posa, A. (2015). Large-eddy simulations of submarine propellers. Journal of Ship Research, 59(4), 227-237.

Baltazar, J., Rijpkema, D., and Falcao de Campos, J.A.C. (2017) On the Use of the ?- Re? Transition Model for the Prediction of the Propeller Performance at Model-Scale. In proceedings international symposiums on marine propulsors, Finland.

Bensow, R. E. and Bark, G. (2010). Implicit LES predictions of the cavitating flow on a propeller. Journal of fluids engineering, 132(4), 041302.

Black, S. D. (1997). Integrated lifting-surface/Navier-Stokes design and analysis methods for marine propulsors. Doctoral dissertation, Massachusetts Institute of Technology.

Berger, S., Bauer, M., Druckenbrod, M., and Abdel-Maksoud, M. (2013). Investigation of scale effects on propeller-induced pressure fluctuations by a viscous/inviscid coupling approach. In Proc. Third International Symposium on Marine Propulsors (pp. 209-217).

Brizzolara, S., Villa, D., and Gaggero, S. (2008). A systematic comparison between RANS and Panel Methods for Propeller Analysis. In Proc. Of 8th International Conference on Hydrodynamics, Nantes, France.

Calcagni, D., Salvatore, F., Dubbioso, G., and Muscari, R. (2017). A generalized unsteady hybrid DES/BEM methodology applied to propeller-rudder flow simulation. In Proceedings of the VII International Conference on Computational Methods in Marine Engineering (pp. 15-17).

Carlton, J. (2012). Marine propellers and propulsion. Butterworth-Heinemann. 71-73. (pdf page 94)

Carrica, P. M., Castro, A. M., and Stern, F. (2010). Self-propulsion computations using a speed controller and a discretized propeller with dynamic overset grids. Journal of marine science and technology, 15(4), 316-330.

Chang, S. H. (2012). Numerical simulation of steady and unsteady cavitating flows inside water-jets. Doctoral dissertation, The University of Texas at Austin.

Chase, N., Michael, T., and Carrica, P. M. (2013). Overset simulation of a submarine and propeller in towed, self-propelled and maneuvering conditions. International Shipbuilding Progress, 60(1-4), 171-205.

152

Choi, J. K. (2001). Vortical inflow-propeller interaction using an unsteady three-dimensional Euler solver. Doctoral dissertation, The University of Texas at Austin.

Choi, J. K. and Kinnas, S. A. (2001). Prediction of non-axisymmetric effective wake by a three-dimensional Euler solver. Journal of Ship Research, 45(1), 13-33.

Drela, M. (1989). XFOIL: An analysis and design system for low Reynolds number airfoils. In Low Reynolds number aerodynamics (pp. 1-12). Springer, Berlin, Heidelberg.

Fine, N. E. (1992). Nonlinear analysis of cavitating propellers in nonuniform flow. Doctoral dissertation, Massachusetts Institute of Technology.

Gaggero, S. and Brizzolara, S. (2008) A Potential Panel Method for the Prediction of Mid-chord Face and Back Cavitation. 6 th International Conference on High Performance Marine Vehicles, 1, 33-46.

Gaggero, S., Villa, D., and Viviani, M. (2017). An extensive analysis of numerical ship self-propulsion prediction via a coupled BEM/RANS approach. Applied Ocean Research, 66, 55-78.

Ghassemi, H. and Taherinasab, M. (2013). Numerical calculations of the hydrodynamic performance of the contra-rotating propeller (CRP) for high-speed vehicle. Polish Maritime Res., 20(2), 13-20.

Gibson, I. S. and Lewis, R. I. (1973). Ducted propeller analysis by surface vorticity and actuator disk theory. In Proceedings of the Symposium on Ducted Propeller. Royal Institute of Naval Architects.

Greeley, D. S. and Kerwin, J. E. (1982) Numerical methods for propeller design and analysis in steady flow. Transactions of Society of Naval Architects & Marine Engineers, vol. 90, pp. 415 – 453.

Greve, M., Wöckner-Kluwe, K., Abdel-Maksoud, M., and Rung, T. (2012). Viscous-inviscid coupling methods for advanced marine propeller applications. International Journal of Rotating Machinery, 2012.

Hallander, Jan, Lindell, Per. "Model tests for M/T Olympus." SSPA Report No.: RE40116086-01-00-A, 2013.

Hally, David. (2015). Propeller analysis using RANS/BEM coupling accounting for blade blockage. Proceedings of the 4th International Symposium on Marine Propulsors, Austin, United States.

Hally, David. (2017). A RANS-BEM coupling procedure for calculating the effective wakes of ships and submarines. Proceedings of the 5th International Symposium on Marine Propulsors, Espoo, Finland.

He, L. (2010). Numerical simulation of unsteady rotor/stator interaction and application to propeller/rudder combination. Doctoral dissertation, The University of Texas at Austin.

Hess, J. L. and Smith, A. O. (1967). Calculation of potential flow about arbitrary bodies. Progress in Aerospace Sciences, 8, 1-138.

Hess, J. L. and Valarezo, W. O. (1985). Calculation of steady flow about propellers by means of a surface panel method. AIAA, No. 85.

Hoshino, T. (1989). Hydrodynamic analysis of propellers in steady flow usinga surface panel method. Journal of the Society of Naval Architects of Japan, 1989(165), 55-70.

Hsin, C. Y. (1990). Development and analysis of panel methods for propellers in unsteady flow. Doctoral dissertation, Massachusetts Institute of Technology.

Hufford, G. S. (1992). Viscous flow around marine propellers using boundary layer strip theory (Doctoral dissertation, Massachusetts Institute of Technology).

Issa, R. I. (1986). Solution of the implicitly discretised fluid flow equations by operator-splitting. Journal of computational physics, 62(1), 40-65.

Kerwin, J. E. and Lee, C. S. (1978). Prediction of steady and unsteady marine propeller performance by numerical lifting surface theory. Transactions SNAME, vol 86.

Kerwin, J. E., Keenan, D. P., Black, S. D., Diggs, J. G., SCHOTT, C. G., KNIGHT, C. J., NGUYEN, P. N., GREELEY, D.S., MAJUMDAR, P., and MORGAN, W. B. (1994). A coupled viscous/potential flow design method for wake-adapted, multi-stage, ducted propulsors using generalized geometry. Transactions-Society of Naval Architects and Marine Engineers 102: 23-56.

Kim, S., Du, W., and Kinnas, S. A. (2017). Panel Method for Ducted Propellers with Sharp and Round Trailing Edge Duct with Fully Aligned Wake on Blade and Duct. In 5th Symposium on Marine Propulsors, SMP (Vol. 17, pp. 12-15).

Kinnas, S. A. (1992). A general theory for the coupling between thickness and loading for wings and propellers. Journal of Ship Research, 36(1):59

Kinnas, S. A. (2006). A note on the Bernoulli equation for propeller flows: The effective pressure. Journal of ship research, 50(4), 355-359.

Kinnas, S. A. and Fine, N. E. (1989). Theoretical prediction of midchord and face unsteady propeller sheet cavitation. In International Conference on Numerical Ship Hydrodynamics, 5th.

Kinnas, S. A. and Hsin, C. Y. (1992). Boundary element method for the analysis of the unsteady flow around extreme propeller geometries. AIAA journal, 30(3), 688-696.

Kinnas, S. A. and Hsin, C. Y. (1994). The local error of a low-order boundary element method at the trailing edge of a hydrofoil and its effect on the global solution. Computers & fluids, 23(1), 63-75.

Kinnas, S. A. and Pyo, S. (1999). Cavitating propeller analysis including the effects of wake alignment. Journal of Ship Research, 43(1):38–47.

Kinnas, S. A., Choi, J. K., Lee, H., Young, Y. L., Gu, H., Kakar, K., and Natarajan, S. (2002). Prediction of cavitation performance of single or multi-component propulsors and their interaction with the hull. Soc. Nav. Archit. Mar. Eng., Trans, 110, 215-244.

Kinnas, S. A., Lee, H. S., Michael, T. J., and Sun, H. (2007a). Prediction of Cavitating Water-jet Propulsor Performance Using a Boundary Element Method. Proc. 9th Int. Conf. on Numerical Ship Hydrodynamics, Ann Arbor, Michigan.

Kinnas, S. A., Lee, H. S., Sun, H. and He, L. (2007b). Performance prediction of single or multi-component propulsors using coupled viscous/inviscid methods. In Proc. 10th Int. Symposium on the Practical Design of Ships and other Floating Structures, PRADS.

Kinnas, S. A., Yu, X., and Tian, Y. (2012). Prediction of propeller performance under high loading conditions with viscous/inviscid interaction and a full wake alignment model. In 29th Symposium on naval hydrodynamics, Sweden.

Lai, M. C. and Peskin, C. S. (2000). An immersed boundary method with formal second-order accuracy and reduced numerical viscosity. Journal of computational Physics, 160(2), 705-719.

Lee, C. S. (1979). Predicton of steady and unsteady performance of marine propellers with or without cavitation by numerical lifting-surface theory. Doctoral dissertation, Massachusetts Institute of Technology.

Lee, H. (2002). Modeling of unsteady wake alignment and developed tip vortex cavitation. Doctoral dissertation, The University of Texas at Austin.

Lee, J. (1987). A potential based panel method for the analysis of marine propellers in steady flow. Doctoral dissertation, Massachusetts Institute of Technology.

Li, D-Q (2006). Validation of RANS predictions of open water performance of a highly skewed propeller with experiments. Journal of Hydrodynamics, Ser. B, 18(3), 520-528.

Liu, X.L. (2009). A potential based panel method for prediction of steady and unsteady performances of contra-rotating propellers. Proceedings of the 1st International Symposium on Marine Propulsors, Trondheim, Norway.

Mascio, A., Muscari, R., and Dubbioso, G. (2014). On the wake dynamics of a propeller operating in drift. Journal of Fluid Mechanics, 754, 263-307.

155

Mishra, B. (2005). Prediction of performance of podded propulsors via coupling of a vortex–lattice method with an Euler or a RANS solver. Environmental and Water Resources Engineering. Department of Civil, Architectural and Environmental Engineering. The University of Texas at Austin.

Mittal, R. and Iaccarino, G. (2005). Immersed boundary methods. Annu. Rev. Fluid Mech., 37, 239-261.

Pan, Y. and Kinnas, S. A. (2011). A viscous/inviscid interactive approach for the prediction of performance of hydrofoils and propellers with nonzero trailing edge thickness. Journal of Ship Research, 55(1), 45-63.

Rijpkema, D., Starke, B., and Bosschers, J. (2013). Numerical simulation of propeller-hull interaction and determination of the effective wake field using a hybrid RANS-BEM approach. In Third International Symposium on Marin Propulsors, SMP2013.

Salvatore, F., Calcagni, D., Muscari, R., and Broglia, R. (2015). A generalised fully unsteady hybrid RANS/BEM model for marine propeller flow simulations, VI th Int. Conference on Computational Methods in Marine Engineering, MARINE 2015, Rome, Italy, pp. 613-626.

Sanchez-Caja, A., Rautaheimo, P., and Siikonen, T. (2000). Simulation of incompressible viscous flow around a ducted propeller using a RANS equation solver. In Proceedings of the Twenty-Third Symposium on Naval Hydrodynamics.

Sanchez-Caja, A., Sipila, Tuomas P., and Pylkkanen, J.V. (2009) Simulation of viscous flow around a ducted propeller with rudder using different RANS-based approaches. First International Symposium on Marine Propulsors, Trondheim, Norway.

Sánchez-Caja, A., Martio, J., Saisto, I., and Siikonen, T. (2015). On the enhancement of coupling potential flow models to RANS solvers for the prediction of propeller effective wakes. Journal of Marine Science and Technology, 20(1), 104-117.

Schetz, J. A. and Favin, S. (1979). Numerical solution of a body-propeller combination flow including swirl and comparisons with data. Journal of Hydronautics, 13(2), 46-51.

Starke, B. and Bosschers, J. (2012, August). Analysis of scale effects in ship powering performance using a hybrid RANS-BEM approach. In 29th Symposium on Naval Hydrodynamics (pp. 26-31).

Stern, F., Kim, H. T., Patel, V. C., and Chen, H. C. (1986). Computation of viscous flow around propeller-shaft configurations (No. IIHR-305). IOWA INST OF HYDRAULIC RESEARCH IOWA CITY.

Su, Y. and Kinnas, S. A. (2017a). A Generalized Potential/RANS Interactive Method for the Prediction of Propulsor Performance. Journal of Ship Research, 61(4), 214-229.

Su, Y., Kinnas, S. A., and Jukola, H. (2017b). Application of a BEM/RANS Interactive Method to Contra-Rotating Propellers. In Proceedings of the Fifth International Symposium on Marine Propulsors, Espoo, Finland.

Su, Y. and Kinnas, S. A. (2017c). A BEM/RANS interactive method for predicting contra-rotating propeller performance. Ocean Systems Engineering, 7(4), 329-344.

Su, Y. and Kinnas, S. A. (2018). A Time-Accurate BEM/RANS Interactive Method for Predicting Propeller Performance Considering Unsteady Hull/Propeller/Rudder Interaction, In Proceedings of 32nd Symposium on Naval Hydrodynamics, Hamburg, Germany.

Su, Y., Kim, S., Du, W., Kinnas, S. A. (2016) PROPCAV (Version 3.3) user manual and documentation. Department of Civil, Architectural and Environmental Engineering, The University of Texas at Austin.

Sun, H. (2008). Performance prediction of cavitating propulsors using a viscous/inviscid interaction method. Doctoral dissertation, The University of Texas at Austin.

Tani, G., Viviani, M., Hallander, J., Johansson, T., and Rizzuto, E. (2016). Propeller underwater radiated noise: A comparison between model scale measurements in two different facilities and full-scale measurements. Applied Ocean Research 56: 48-66.

Tian, Y., Jeon, C.H., and Kinnas, S.A. (2014). Effective wake calculation/application to ducted propellers. Journal of Ship Research, 58(2), 1-13.

Vaz, G. (2005). Modelling of sheet cavitation on hydrofoils and marine propellers using boundary element methods. Technical University of Lisbon.

Warren, C. L. (1999). Prediction of propulsor-induced maneuvering forces using a coupled viscous/potential-flow method for integrated propulsors. MASSACHUSETTS INST OF TECH CAMBRIDGE DEPT OF OCEAN ENGINEERING.

Young, Y. L. (2002). Numerical modeling of supercavitating and surface-piercing propellers. Doctoral dissertation, The University of Texas at Austin.

Zhuang, Z. Li, B. Zhao, F. (2004). Integral calculation of viscous flow around ship hull with propeller. Journal of Ship Mechanics. 2004